NASA Technical Memorandum 100991

A High Fidelity Real-Time Simulation of a Small Turboshaft Engine

Mark G. Ballin

(NASA-TM-100991) A HIGH FIDELITY REAL-TIME SIMULATION OF A SMALL TURBOSHAFT ENGINE (NASA) 95 p CSCL 21E

N88-26378

Unclas
G3/08 0156166

July 1988

National Aeronautics and
Space Administration

NASA Technical Memorandum 100991

A High Fidelity Real-Time Simulation of a Small Turboshaft Engine

Mark G. Ballin, Ames Research Center, Moffett Field, California

July 1988

National Aeronautics and
Space Administration

Ames Research Center
Moffett Field, California 94035

National Aeronautics and
Space Administration

Ames Research Center
Moffett Field, California 94035

NASA

Reply to Attn of:

Shelley J. Scarich
M/S 241-13

ERRATA

RE: NASA TM 100991

A High-Fidelity Real-Time Simulation of a Small Turboshaft Engine

Mark G. Ballin

July 1988

On p. 2, figure 1, a correction should be noted.
In the upper middle portion of the figure, GAS INDUCED FLAP REGRESSIVE should be CONTROL-SYSTEM-INDUCED FLAP REGRESSIVE.

Yours,

Shelley Scarich
Publications

A HIGH FIDELITY REAL-TIME SIMULATION OF A SMALL TURBOSHAFT ENGINE

Mark G. Ballin

Ames Research Center

SUMMARY

A high-fidelity component-type model and real-time digital simulation of the General Electric T700-GE-700 turboshaft engine were developed for use with current generation real-time blade-element rotor helicopter simulations. A control system model based on the specification fuel control system used in the UH-60A Black Hawk helicopter is also presented. The modeling assumptions and real-time digital implementation methods particular to the simulation of small turboshaft engines are described. The validity of the simulation is demonstrated by comparison with analysis-oriented simulations developed by the manufacturer, available test data, and flight test time histories.

NOMENCLATURE

A_m	area of exposed metal; used in heat-sink representation
B_1	seal-pressurization bleed fraction
B_2	power-turbine-balance bleed fraction
B_3	compressor-diffuser bleed fraction
c_{pg}	specific heat of gas; used in heat-sink representation
c_{pm}	specific heat of metal; used in heat-sink representation
FAR	ratio of fuel to atmospheric gas in combustor
h	convective heat transfer coefficient; used in heat-sink representation
$H2$	station 2 enthalpy, Btu/lb_m
$H3$	station 3 enthalpy, Btu/lb_m
$H41$	station 4.1 enthalpy, Btu/lb_m
$H41_{ns}$	station 4.1 enthalpy not including heat-sink effects, Btu/lb_m
$H44$	station 4.4 enthalpy, Btu/lb_m
$H45$	station 4.5 enthalpy, Btu/lb_m
$H49$	station 4.9 enthalpy, Btu/lb_m
HVF	heating value of fuel, Btu/lb_m
J	moment of inertia of all mass rigidly attached to the engine output shaft, $ft \cdot lb_f \cdot sec^2$
J_{GT}	moment of inertia of the rigid mass which represents the gas generator, compressor, and the associated shafting, $ft \cdot lb_f \cdot sec^2$
J_{load}	moment of inertia of the load mass, $ft \cdot lb_f \cdot sec^2$
J_{PT}	moment of inertia of the power turbine and output shaft, $ft \cdot lb_f \cdot sec^2$
K_{b3}	station 3 bleed-flow coefficient

PRECEDING PAGE BLANK NOT FILMED

K_{bl}	fraction of diffuser bleed gas which is used to cool the gas generator turbine blades
K_{damp}	power turbine speed damping coefficient, $ft \cdot lb_f \cdot sec/rad$
K_{dpb}	combustor pressure drop coefficient, $lb_f^2 \cdot sec^2/lb_m^2 \cdot in^4 \cdot deg\ R$
K_{H2}	station 2 enthalpy coefficient, $Btu/lb_m \cdot deg\ R$
K_{H3_1}	station 3 enthalpy coefficient, $Btu/lb_m \cdot deg\ R$
K_{H3_2}	station 3 enthalpy coefficient, Btu/lb_m
K_{H41_1}	station 4.1 enthalpy coefficient, $Btu/lb_m \cdot deg\ R$
K_{H41_2}	station 4.1 enthalpy coefficient, Btu/lb_m
K_{H45}	fraction of station 4.4 enthalpy used to represent station 4.5 enthalpy
K_{Ps3}	fraction of total pressure at station 3 used to represent static pressure at station 3
K_{QC_1}	empirically-determined compressor torque coefficient
K_{QC_2}	empirically-determined compressor torque coefficient
K_{T41_1}	station 4.1 temperature coefficient, $lb_m \cdot deg\ R/Btu$
K_{T41_2}	station 4.1 temperature coefficient, $deg\ R$
K_{T45_1}	station 4.5 temperature coefficient, $lb_m \cdot deg\ R/Btu$
K_{T45_2}	station 4.5 temperature coefficient, $deg\ R$
K_{T49_1}	station 4.9 temperature coefficient, $lb_m \cdot deg\ R/Btu$
K_{T49_2}	station 4.9 temperature coefficient, $deg\ R$
K_{TH41_1}	station 4.1 velocity ratio coefficient, $1/deg\ R$
K_{TH41_2}	station 4.1 velocity ratio coefficient
K_{TH45_1}	station 4.5 velocity ratio coefficient, $1/deg\ R$

K_{TH45_2}	station 4.5 velocity ratio coefficient
K_{V3}	station 3 volume coefficient, $lb_f/in^2 \cdot lb_m \cdot deg\ R$
K_{V41}	station 4.1 volume coefficient, $lb_f/in^2 \cdot lb_m \cdot deg\ R$
K_{V45}	station 4.5 volume coefficient, $lb_f/in^2 \cdot lb_m \cdot deg\ R$
K_{WGT}	station 4.1 flow coefficient, $lb_m \cdot in^2/lb_f \cdot sec$
M	mass of metal that absorbs heat energy from gas; used in heat-sink representation
NG	rotational speed of compressor and gas generator, rpm
NG_c	corrected compressor and gas generator speed; a nonphysical value which is independent of inlet conditions, rpm
NG_{des}	design rotational speed of the gas generator and compressor, rpm
NP	rotational speed of power turbine and output shaft, rpm
NP_{des}	design rotational speed of power turbine and output shaft, rpm
$P1$	station 1 total pressure, lb_f/in^2
$P2$	station 2 total pressure, lb_f/in^2
$P3$	station 3 total pressure, lb_f/in^2
$P41$	station 4.1 total pressure, lb_f/in^2
$P45$	station 4.5 total pressure, lb_f/in^2
$P49$	station 4.9 total pressure, lb_f/in^2
P_{amb}	ambient pressure, lb_f/in^2
P_s3	station 3 static pressure; a fuel-control-system parameter, lb_f/in^2
P_s9	station 9 static pressure, lb_f/in^2
P_{std}	standard-day pressure, lb_f/in^2
Q_{acc}	torque required for helicopter accessory power, $ft \cdot lb_f$

Q_C	torque required by compressor, $ft \cdot lb_f$
Q_{damp}	torque required by helicopter gearbox (gearbox damping), $ft \cdot lb_f$
Q_{eng}	torque transmitted to helicopter gearbox from both engines, $ft \cdot lb_f$
Q_{GT}	torque output of gas generator, $ft \cdot lb_f$
Q_{mr}	torque required by helicopter main rotor, $ft \cdot lb_f$
Q_{PT}	torque output of power turbine, $ft \cdot lb_f$
Q_{req}	torque required by external load with respect to power turbine speed, $ft \cdot lb_f$
Q_{tr}	torque required by helicopter tail rotor, $ft \cdot lb_f$
$T1$	station 1 temperature, $deg\ R$
$T2$	station 2 temperature, $deg\ R$
$T3$	station 3 temperature, $deg\ R$
$T41$	station 4.1 temperature, $deg\ R$
$T41_{ns}$	station 4.1 temperature not including heat-sink effects, $deg\ R$
$T41_{sgn}$	heat-sink function
$T45$	station 4.5 temperature, $deg\ R$
$T49$	station 4.9 temperature, $deg\ R$
T_{amb}	ambient temperature, $deg\ R$
TC_{T41}	empirically determined constant used in station 4.1 heat-sink representation, $lb_m^{\frac{4}{5}} \cdot sec^{\frac{8}{5}}/deg\ R^{\frac{1}{2}}$
T_{g_i}	temperature of gas entering the heat-sink representation control volume
T_{g_o}	temperature of gas leaving the heat-sink representation control volume
T_m	temperature of exposed metal as used in heat-sink representation

T_{std}	standard atmosphere temperature at sea-level, $deg\ R$
$W41$	station 4.1 mass flow rate of combustion gases, lb_m/sec
$W45$	station 4.5 mass flow rate of combustion gases, lb_m/sec
$W45_c$	corrected station 4.5 mass flow rate of combustion gases, lb_m/sec
$WA2$	station 2 mass-flow rate of atmospheric gas, lb_m/sec
$WA24_{bl}$	station 2.4 bleed flow of atmospheric gas, lb_m/sec
$WA2_c$	corrected station 2 mass-flow rate of atmospheric gas, lb_m/sec
$WA3$	station 3 mass flow rate of atmospheric gas, lb_m/sec
$WA31$	station 3.1 mass flow rate of atmospheric gas, lb_m/sec
$WA3_{bl}$	diffuser bleed discharge flow, lb_m/sec
W_f	fuel flow, lb_m/sec
W_g	mass flow rate of gas into heat-sink representation control volume
δ_2	ratio of inlet pressure to sea-level pressure
ΔH_{GT}	gas-generator-turbine enthalpy drop, Btu/lb_m
ΔH_{PT}	power turbine enthalpy drop, Btu/lb_m
η	combustor efficiency
τ_1	heat-sink lead time constant for a trim operating condition; used in small-perturbation representation, sec
τ_2	heat-sink lag time constant for a trim operating condition; used in small-perturbation representation, sec
θ_2	ratio of inlet temperature to standard-day temperature
θ_{41}	station 4.1 squared-critical-velocity ratio
θ_{45}	station 4.5 squared-critical-velocity ratio

A HIGH FIDELITY REAL-TIME SIMULATION OF A SMALL TURBOSHAFT ENGINE

Mark G. Ballin

Ames Research Center

SUMMARY

A high-fidelity component-type model and real-time digital simulation of the General Electric T700-GE-700 turboshaft engine were developed for use with current generation real-time blade-element rotor helicopter simulations. A control system model based on the specification fuel control system used in the UH-60A Black Hawk helicopter is also presented. The modeling assumptions and real-time digital implementation methods particular to the simulation of small turboshaft engines are described. The validity of the simulation is demonstrated by comparison with analysis-oriented simulations developed by the manufacturer, available test data, and flight-test time histories.

INTRODUCTION

The accurate representation of propulsion system performance and dynamic response to changing load conditions is becoming an important component in experimental handling-qualities investigations of rotorcraft. A high level of sophistication in modeling of the powerplant, drive train, and all power requirements of the vehicle is necessary to achieve an accurate representation of vehicle performance and dynamic response, especially for such demanding mission tasks as nap-of-the-earth flight. It is also important for simulations of off-design vehicle configurations and in exploring expanded mission requirements for a particular vehicle. A real-time representation of the propulsion system is required for piloted simulation. Piloted simulation enables efficient determination of requirements made on the propulsion system as well as the response of the pilot to the interaction of the propulsion system with the vehicle.

High-fidelity propulsion system modeling is particularly necessary in the investigation of integrated flight and propulsion controls for rotorcraft. As shown in figure 1, much dynamic interaction between the rotor, drive train, and propulsion system takes place at or below the once-per-revolution frequency of the rotor (ref. 1). The present generation of real-time blade-element rotor helicopter simulations such as Sikorsky Gen Hel (ref. 2) can accurately model individual blade dynamics up to the one-per-revolution frequency. A real-time model which correctly represents propulsion-system dynamic response at a high bandwidth is therefore necessary. In addition, advanced propulsion-control strategies may involve monitoring or estimation of internal engine states, so an accurate internal representation of the engine is required. Because the load demand of rotorcraft propulsion systems typically varies from zero power to full power, the model must be valid over the full power range of the actual engine. It must also be valid over a complete range of ambient operating conditions. Engine parameters of primary importance to real-time handling qualities investigations include the output torque and dynamics of the gas turbines, both of which are necessary for pilot sound cuing as well as for modeling of power output. Also important are parameters used by the fuel

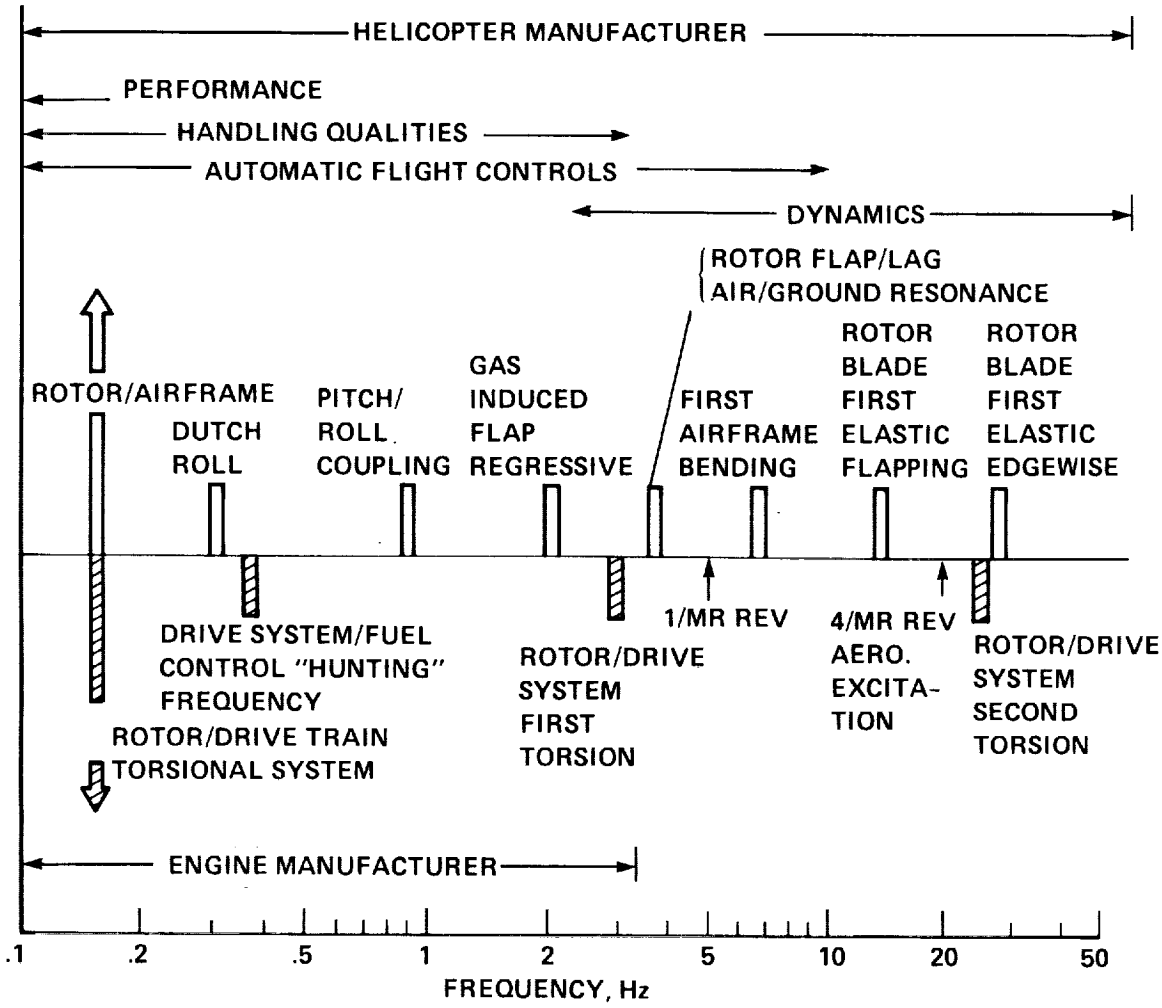

Figure 1: Modal frequencies of interest in engine and fuel-control design and modeling (ref. 3).

control system, such as compressor discharge static pressure and internal engine temperatures. Of somewhat less importance to piloted simulation are the internal mass flows, which may be used to determine proximity to limits such as compressor stall.

In the available real-time models, engine dynamics are represented by experimentally determined partial derivatives of changes of output torque to changes in turbine speeds and fuel flow. Such models are unsatisfactory because needed internal engine states may not be modeled. In addition, dynamic characteristics of the existing models have been shown to be incorrect in comparison with experimental data (ref. 4). Partial-derivative models tend to be valid only for a limited range of operating conditions. Because they are not based on the physical phenomena which they represent, their validity is always in question when used under conditions for which they are not designed.

An acceptable level of fidelity is can be achieved by using an engine model made up of individual engine components, each of which is modeled based on thermodynamic laws governing the engine cycle. Such component-type simulations are used by engine manufacturers to study the steady-state and transient behavior of engines, but they are usually far too complex for use in real-time digital simulation. A component engine model which is simplified for real-time use is the most promising alternative to partial-derivative engine representations.

As part of a real-time simulation study of the effects of propulsion control on helicopter handling qualities, a current-generation turboshaft engine was developed for use with the Sikorsky Gen Hel blade-element simulation. A version of Gen Hel representative of the UH-60A Black Hawk was available at Ames, so its powerplant, the General Electric (GE) T700, was chosen. In addition, accurate physical models of the fuel control system, mechanical actuators and linkages, and the engine sensors were developed to an equivalent level of sophistication. They are necessary for a correct representation of closed-loop propulsion system dynamics, engine protection control, and the effects of control modification. This paper describes the development of a real-time simplified-component representation of the engine. Models of the engine sensors, the fuel control system, and control actuators are also presented, but without extensive discussion. Note that all uses of "rotor" in this paper refer to the helicopter main or tail rotor system, and not to engine turbine rotors.

I would like to express appreciation to Dr. Robert T. N. Chen of the Flight Dynamics and Controls Branch for his aid and advice in the development of linear models used to verify the volume dynamics approximation. Richard McFarland of the Simulation Investigations Branch provided explanations of real-time numerical methods, hardware constraints, and software interfacing that were invaluable in developing an acceptable real-time simulation code. Special thanks are given to Mr. Dan Gilmore of the General Electric Corporation. Mr. Gilmore was of tremendous help in providing the data used in the validation effort, and his suggestions for improvements to and expansion of the engine and fuel control system models were critical to obtaining a valid simulation.

ENGINE AND FUEL CONTROL SYSTEM

The engine modeled is a T700-GE-700 (fig. 2), a small turboshaft engine of the 1600-hp class which powers the UH-60A Black Hawk helicopter. It consists of a five-stage axial and a single-stage centrifugal flow compressor; a low-fuel-pressure, flowthrough annular combustion chamber; a two-stage axial flow gas generator turbine; and a two-stage independent power turbine (ref. 5). The first two stages of the compressor use variable-geometry inlet guide vanes and stator vanes, and air is bled from the compressor exit to cool the gas generator turbine. The power turbine, which is uncooled, has a coaxial driveshaft which extends forward through the front of the engine where it is connected to the output shaft assembly.

ORIGINAL PAGE IS
OF POOR QUALITY

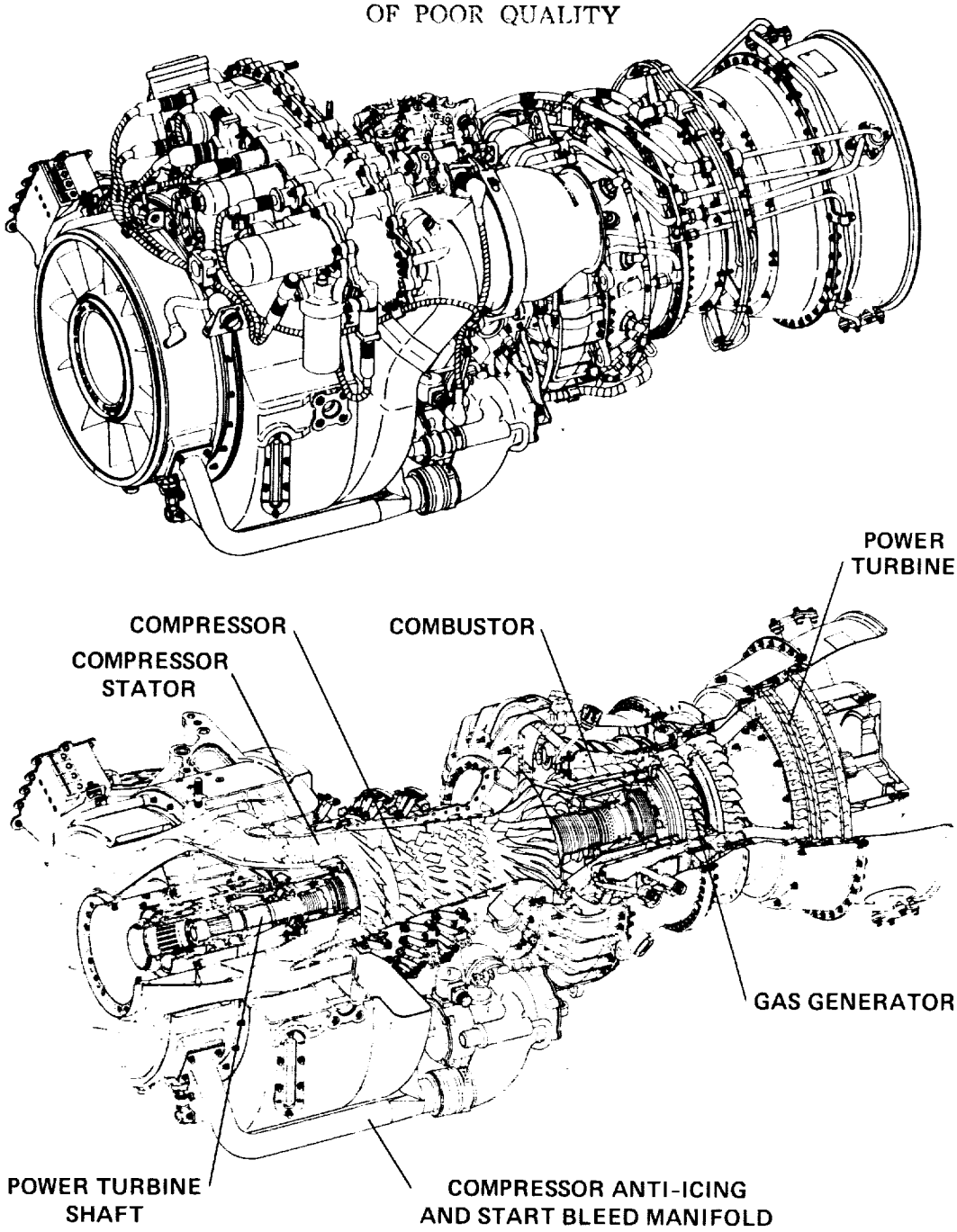

Figure 2: General Electric T700-GE-700 engine. (From ref. 6.)

ORIGINAL PAGE IS
OF POOR QUALITY

The T700 fuel control system provides power modulation for speed control, overtemperature protection, and load sharing between engines for multiple-engine installations. It consists of a hydromechanical control unit (HMU) for fuel metering as a function of schedules of gas generator speed and power demand, and an electrical control unit (ECU) which performs isochronous power-turbine speed governing and overtemperature protection (ref. 6). The HMU consists of a high pressure vane pump and mechanical cams which impose acceleration, deceleration, topping, and idle schedules as functions of inlet temperature and gas generator speed. A feed-forward compensation of load demand is achieved by adjusting the set point as a function of the helicopter collective control position. The compressor variable geometry is also controlled as a function of inlet temperature and gas generator speed. The ECU provides output shaft speed-control by driving a torque motor in the HMU based on a power-turbine-speed error signal. The torque motor adjusts the HMU fuel demand downward, so that an electrical system failure results in maximum power. Power turbine inlet temperature is also monitored; fuel flow is reduced when it exceeds limits. Load sharing is also provided; fuel flow is adjusted if torque is determined to be lower than that of another engine operating in parallel.

The drive train which transmits power to the helicopter requires a high gear-ratio transmission which reduces the engine shaft speed to a level usable by the rotor system. It transfers power to the main rotor, tail rotor, and accessory loads. Because power requirements of a helicopter are zero during certain conditions such as autorotation, power from each engine must also pass through a clutch which disengages the engine from the gearbox if transmission speed exceeds that of the engine shaft.

ENGINE MODEL

Gas turbine engines convert heat energy into useful work by expanding gases and forcing them to rotate turbines. A typical free-turbine turboshaft engine consists of four major components: the compressor, the combustor, the gas generator, and the power turbine. Chemical energy is converted to heat in the combustor. Heat causes the expansion of gas which rotates the gas generator turbine. The gas generator is directly linked to the compressor, which compresses atmospheric gas for use in the combustor. Energy which is not consumed by the gas generator is extracted by the power turbine as the expanding gases pass through it. The power turbine, which is also called the free or independent turbine, is not connected to the other rotating components. Because of this, a turboshaft engine can operate from full to zero power levels while maintaining a specified output shaft speed. Any description of the operating point of a free-turbine turboshaft engine is therefore dependent on the speeds of both the gas generator and the power turbines.

The four major components are separated by fluid mixing volumes, each of which is associated with flow passages within the engine where thermodynamic states are quantifiable. States of the gas in each control volume are expressed in terms of pressure, temperature, and mass flow. They are determined as functions of energy transfer across each component. Equations describe each component in terms of the state of the component, thermodynamic states upstream and downstream of the component, energy applied to or taken from the component, and efficiencies of energy transfer. Conservation of mass is used to determine the values of mass flows into and out of each control volume. Dynamics of the rotating components are modeled by relating changes of angular rotation of a given component to its moment of inertia and the applied torque. A load from an external source is required to determine power turbine (and output shaft) speed. Losses associated with fluid dynamic or mechanical processes are represented by single- or multivariable functions based on previously-derived or empirical data. Inputs consist of ambient temperature and pressure at the inlet, pressure at the exhaust, fuel flow, and load torque.

Figure 3 is a representation of the major engine components and locations, or stations, within the engine where thermodynamic states of the gas must be modeled. The six compressor stages and variable-geometry flow vanes are represented with the compressor component, between stations 2 and 3. Bleed flow which is used for seal pressurization and power turbine balance is extracted from stage 4 of the compressor, which is represented by station 2.4. Station 3 is the compressor diffuser, or outlet. Flow is bled at this point to cool the combustor and gas generator turbine. Station 3.1 is the combustor and station 4.1 is the mixing volume representing the combustor outlet and gas-generator-turbine inlet. The two stages of the gas generator turbine are modeled by the generator turbine component. Station 4.4 represents the thermodynamic state of output gases passing through this turbine, not including the effects of the cooling bleed flow. These effects are added at station 4.5, which represents the power turbine inlet. The two-stage power turbine is represented by the power turbine component. Station 4.9 is the power turbine outlet, and station 9 is the engine exhaust.

Development History

As a part of ongoing research in turboshaft engine technology, a component-type mathematical model was developed by NASA Lewis Research Center for real-time hybrid computer simulation (ref. 7). It is a greatly simplified version of the nonreal-time component-type digital simulation developed by GE. It is capable of representing the operating condition of the major internal engine components as well as the engine thermodynamic cycle. It was chosen to serve as the basis for development of a real-time digital simulation.

Modeling simplifications made in the development of the NASA-Lewis hybrid simulation model were based on a general simulation technique developed at NASA-Lewis (ref. 8) as well as experience with small turboshaft engines. Power turbine efficiency as a function of its speed was neglected because, for the designed use of the model, the power turbine deviates from design speed by only a few percent. No modeling of compressor surge, heat-sink losses, or exhaust pressure losses was attempted. Linear relationships were used to describe secondary effects such as bleed flows. Dynamics of the variable geometry guide vanes also were assumed to be instantaneous. A digital program was developed using CSMP, a high-level system modeling language. It accurately reproduced steady-state operation of an experimental test article operated at Lewis Research Center. A real-time fixed-point version of this program was then written for use in interfacing with control system hardware at Lewis Research Center. Because of the lack of transient data, no validation of engine dynamic characteristics was performed in this phase of the model development (ref. 7).

A real-time digital simulation was developed in FORTRAN at NASA Ames, based on the NASA Lewis hybrid model. During the validation effort for the real-time simulation, some expansion of the model was found to be necessary. A function representing station 4.9 total pressure was added, and a model of the nonadiabatic energy transfer at station 4.1 was required. A power-turbine damping factor was also added to aid in matching transient response at low power levels. In each case, models developed by GE were used.

Model Component Equations

The equations which describe the complete engine mathematical model are given below. As will be described in the Volume Dynamics Approximation section, implementation of the model for real-time

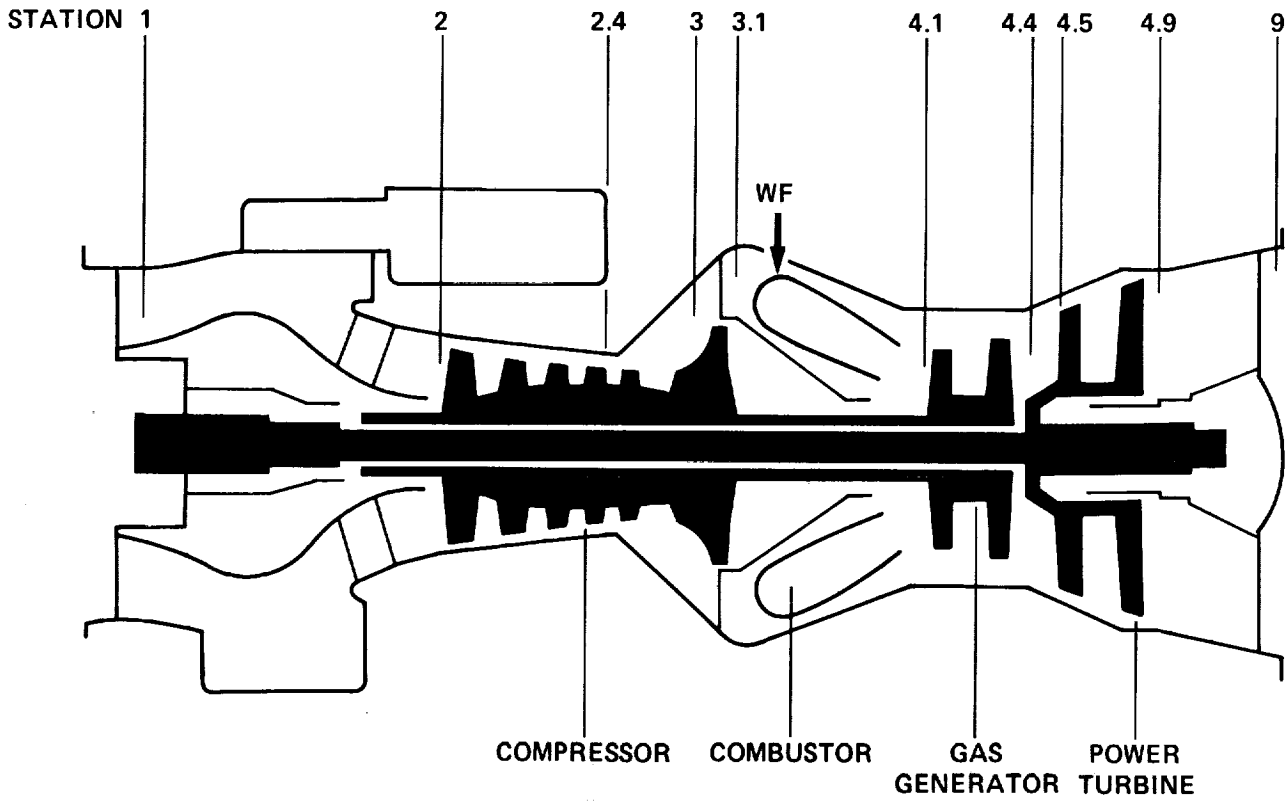

Figure 3: Primary components of a small turboshaft engine.

use required some simplification of the equations. Model constants and plots of mass-flow and energy functions which are specific to the T700-GE-700 engine are presented in Appendix A.

Pressure and temperature stagnation effects have been found to roughly offset the aircraft inlet losses over most of the aircraft flight envelope. Total pressure $P2$ and temperature $T2$ are therefore estimated to be equal to the static ambient conditions.

$$P2 = P1 = P_{amb} \tag{1}$$

$$T2 = T1 = T_{amb} \tag{2}$$

Station 2 enthalpy is calculated from station 2 temperature.

$$H2 = K_{H2} \cdot T2 \tag{3}$$

Static pressure at station 3 is represented as a linear function of the total pressure.

$$P_s3 = K_{Ps3} \cdot P3 \tag{4}$$

The gas-generator turbine speed is corrected by the square root of a nondimensional temperature parameter.

$$\theta_2 = \frac{T2}{T_{std}} \tag{5}$$

$$NG_c = \frac{NG}{\sqrt{\theta_2}} \tag{6}$$

On the actual engine, two stages of the compressor contain variable-angle stator vanes to achieve rapid compressor acceleration without stall and to optimize fuel consumption. Vane position is controlled by the HMU as a function of $T2$ and NG. In order to minimize complexity of the real-time model, corrected compressor airflow is determined from a performance map which is a function of corrected station-3 static pressure and corrected gas generator speed only. This assumes that for any instant in time, the variable-geometry stator vanes are in the nominal design position for a given operating point of the compressor.

$$WA2_c = f_1\left(\frac{P_s3}{P2}, NG_c\right) \tag{7}$$

$$\delta_2 = \frac{P2}{P_{std}} \tag{8}$$

$$WA2 = WA2_c\frac{\delta_2}{\sqrt{\theta_2}} \tag{9}$$

Temperature and enthalpy changes from stations 2 to 3 are determined as a function of the change of pressure across the compressor component.

$$T3 = T2 \cdot f_2\left(\frac{P_s3}{P2}\right) \tag{10}$$

$$H3 = K_{H3_1}T3 + K_{H3_2} \tag{11}$$

The nonlinear fractions of bleed flow are also determined from function maps. Actual bleed flows are then determined from the bleed fractions. Flow extracted at station 2.4 acts to pressurize the seals, preventing oil loss and keeping hot gases, dust, and moisture out of the oil sumps. In addition, the flow is used to pressurize the power-turbine balance piston, which provides a forward force on the power turbine to alleviate some of the thrust load on the turbine bearing. The diffuser discharge air, $WA3_{bl}$, is used to cool the combustion liner and the gas-generator-turbine blades and shrouds. The fraction of the bleed flow used to cool the gas generator is reintroduced to the gas path downstream of the gas generator turbine. The turbine blades are cooled internally and the bleed gas is then released through a shower-head-type series of nozzles.

$$B_1 = f_3(NG_c) \tag{12}$$

$$B_2 = f_4(WA2_c) \tag{13}$$

$$B_3 = f_5(WA2_c) \tag{14}$$

$$WA24_{bl} = WA2(B_1 + B_2) \tag{15}$$

$$WA3_{bl} = WA2(B_3 + K_{b3}) \tag{16}$$

The fraction of mass flow at the diffuser is determined by subtracting the compressor stage-4 bleed flow from flow entering the compressor.

$$WA3 = WA2 - WA24_{bl} \tag{17}$$

The combustor mass flow and efficiency are nonlinear functions of inlet and outlet pressures, inlet temperature, and the fuel-to-air ratio. Change of enthalpy across the combustor is also a function of the heating value of the fuel.

$$WA31 = \sqrt{\frac{P3(P3 - P41)}{K_{dpb} \cdot T3}} \tag{18}$$

$$FAR = \frac{W_f}{WA31} \tag{19}$$

$$\eta = f_6(FAR) \tag{20}$$

$$H41_{ns} = \frac{H3 + \eta \cdot FAR \cdot HVF}{1 + FAR} \tag{21}$$

The value of the temperature at station 4.1 without heat-sink dynamics is a function of enthalpy.

$$T41_{ns} = K_{T41_1} H41_{ns} + K_{T41_2} \tag{22}$$

The temperature at station 4.1 is expressed as a transfer function with slowly varying coefficients. (See the following subsection.) If no heat-sink representation is used, $T41 = T41_{ns}$.

$$T41 = T41_{ns} \cdot f_s(T41, T41_{ns}, W41, NG_c) \tag{23}$$

$$H41 = K_{H41_1} T41 + K_{H41_2} \tag{24}$$

As described in reference 7, a critical velocity parameter is used to calculate an enthalpy change parameter for the gas generator turbine as a function of pressure ratio only. Actual enthalpy drop is calculated by multiplying this parameter by the squared critical velocity ratio. Exit enthalpy is then determined.

$$\theta_{41} = K_{TH41_1} T41 + K_{TH41_2} \tag{25}$$

$$\Delta H_{GT} = \theta_{41} \cdot f_7 \left(\frac{P45}{P41} \right) \tag{26}$$

$$H44 = H41 - \Delta H_{GT} \tag{27}$$

Over the normal operating range of the engine, a choked nozzle equation is adequate to calculate the mass flow.

$$W41 = K_{WGT} \frac{P41}{\sqrt{\theta_{41}}} \tag{28}$$

At station 4.5, gases from the station 4.4 and cooling-bleed flow from the compressor are mixed before passing through the power turbine. The enthalpy of the mixed gases is proportional to enthalpy at station 4.4. Temperature is then determined from enthalpy.

$$H45 = K_{H45} H44 \tag{29}$$

$$T45 = K_{T45_1} H45 + K_{T45_2} \tag{30}$$

A power-turbine enthalpy drop parameter is determined as a function of pressure ratio across the turbine, as described for the gas-generator turbine. In addition, mass flow is determined as a function of pressure ratio only.

$$\theta_{45} = K_{TH45_1} T45 + K_{TH45_2} \tag{31}$$

$$\Delta H_{PT} = \theta_{45} \cdot f_8 \left(\frac{P49}{P45} \right) \tag{32}$$

$$W45_c = f_9 \left(\frac{P_s9}{P45} \right) \tag{33}$$

$$W45 = W45_c \frac{P45}{\sqrt{\theta_{45}}} \tag{34}$$

Station 4.9 enthalpy and temperature are determined from the change in enthalpy across the power turbine.

$$H49 = H45 - \Delta H_{PT} \tag{35}$$

$$T49 = K_{T49_1} H49 + K_{T49_2} \tag{36}$$

Station 4.9 pressure is determined from a nonlinear function map of gas generator speed (provided by GE).

$$P_s9 = P_{amb} \tag{37}$$

$$P49 = P_s9 \cdot f_{10}(NG_c) \tag{38}$$

Values of torque which are output or required by the engine are determined from the changes in energy across the compressor and turbines. Effects of the compressor interstage bleed flows are accounted for with an empirically determined function. A damping factor based on change of power turbine speed is an additional term in the power turbine torque equation.

$$Q_C = 778.12 \cdot \frac{60}{2\pi} \cdot \frac{1}{NG} \{WA2(K_{QC_1} H3 - H2) + WA3 \cdot K_{QC_2} H3\} \tag{39}$$

$$Q_{GT} = 778.12 \cdot \frac{60}{2\pi} \cdot \frac{1}{NG} \cdot W41 \Delta H_{GT} \tag{40}$$

$$Q_{PT} = 778.12 \cdot \frac{60}{2\pi} \cdot \frac{1}{NP} \cdot W45 \Delta H_{PT} - K_{damp} \cdot \frac{2\pi}{60} \cdot (NP - NP_{des}) \tag{41}$$

Conservation of mass is applied to determine intervolume pressure dynamics for stations 3, 4.1, and 4.5.

$$P3 = K_{V3} \int T3(WA3 - WA3_{bl} - WA31)\,dt \tag{42}$$

$$P41 = K_{V41} \int T41(WA31 - W_f - W41)\,dt \tag{43}$$

$$P45 = K_{V45} \int T45(W41 - W45 + B_3 K_{bl} WA2)\,dt \tag{44}$$

Turbine speeds are determined as a function of the externally-applied torques by assuming conservation of angular momentum.

$$NG = \frac{60}{2\pi} \int \frac{Q_{GT} - Q_C}{J_{GT}} dt \tag{45}$$

$$J = J_{PT} + J_{load} \tag{46}$$

$$NP = \frac{60}{2\pi} \int \frac{Q_{PT} - Q_{req}}{J} dt \tag{47}$$

Heat-Sink Model

Early in the validation effort, the modeling of nonadiabatic processes occurring in areas of large temperature gradients was found to be necessary for correct transient response. There is a transient energy transfer which is caused by the metal mass of the turbine absorbing heat from the hot gas. This is especially significant at station 4.1, immediately downstream of the combustor. Known as the heat-sink effect, this phenomenon can be modeled as a lumped parameter system with the heat transfer equations.

$$c_{pm} M \frac{dT_m}{dt} = hA_m(T_{g_i} - T_m) \tag{48}$$

$$c_{pg} W_g(T_{g_i} - T_{g_o}) = c_{pm} M \frac{dT_m}{dt} \tag{49}$$

The first equation relates the change in metal temperature to the difference between metal and gas temperatures, and the second equation represents the effect of this change of metal temperature on the gas.

This model is provided by GE and is identical to the model used in transient analysis simulations. The above equations can be expressed as the transfer function

$$\frac{T_{g_o}}{T_{g_i}} = \frac{T41}{T41_{ns}} = \frac{\left(\frac{Mc_{pm}}{hA_m} - \frac{Mc_{pm}}{W_g c_{pg}}\right)s + 1}{\frac{Mc_{pm}}{hA_m}s + 1}. \tag{50}$$

The time constant $\frac{Mc_{pm}}{hA_m}$ is known to be a function of mass flow and gas temperature.

$$\frac{Mc_{pm}}{hA_m} = TC_{T41} \cdot \frac{\sqrt{T41}}{W41^{\frac{4}{5}}} \tag{51}$$

where TC_{T41} is an empirically determined constant. The value of $\frac{Mc_{pm}}{c_{pg}}$ varies as a function of gas generator speed.

$$T41_{sgn} = f_{hs}(NG_c) \tag{52}$$

$$\frac{Mc_{pm}}{W_g c_{pg}} = \frac{T41_{sgn}}{W41} \tag{53}$$

REAL-TIME IMPLEMENTATION

Because of the high-frequency dynamics contained in the described model, the model must be simplified for use with real-time rotorcraft simulations. The following sections describe the approximations made.

Volume Dynamics Approximation

Each of the control volumes within the engine is associated with a temperature, pressure, and change of mass of the air and fuel mixture. During steady-state operation of the engine, a state of equilibrium exists between the control volumes for each of these parameters. A change in the state of any control volume creates pressure and mass flow changes in the other control volumes until a new equilibrium is achieved. The dynamics associated with this change of equilibrium are very rapid, especially for a small turboshaft engine for which control volumes are small compared to the high mass flows. They are well outside the bandwidth of interest for piloted handling qualities investigations. The discrete modeling of such high-frequency dynamics necessitates stepping forward in time in extremely small increments, resulting in a high computation overhead which is unacceptable for real-time simulation.

Therefore, it must be assumed that pressures and mass flows within the mixing volumes are in equilibrium at all times. Such a quasi-steady approximation is only valid if it can be shown that the eliminated dynamics have a negligible effect on the lower-frequency engine dynamics. Several existing real-time simulations do make this approximation to engine volume dynamics (refs. 9, 10, 11, and 12). However, the characteristicly high bandwidth of blade-element rotor simulations requires a high propulsion-system model bandwidth. The validity of the approximation therefore requires a closer investigation when applied to a small turboshaft engine which is coupled to a high-fidelity helicopter simulation.

The volume dynamics approximation was shown to be valid for small turboshaft engines by comparison of linear representations of two nonlinear digital simulations, one of which modeled component

volumes using the quasi-steady approximation. The other simulation contained full volume dynamics. Because of nonlinear turbine-efficiency and mass-flow relationships, the dynamic response of a turboshaft engine may generally not be described linearly. However, a linear model which is accurate for small perturbations about one operating point is useful in evaluating the open-loop engine response to a fuel-flow input.

The linear perturbation models were extracted from the complete nonlinear digital simulation and a reduced-order nonlinear simulation which contained the volume dynamics approximation. Because the station 4.1 heat-sink approximation was added to both models as a linear lead-lag representation, it was not included in the analysis. The resulting five degrees-of-freedom represented were pressures at stations 3, 4.1, and 4.5 and the two turbine speeds. In state-equation form,

$$\dot{\bar{x}} = A\bar{x} + \bar{b}W_f \tag{54}$$

where

$$\bar{x} = \begin{Bmatrix} NG \\ NP \\ P3 \\ P41 \\ P45 \end{Bmatrix}$$

$$A = \begin{bmatrix} \frac{\partial \dot{NG}}{\partial NG} & \frac{\partial \dot{NG}}{\partial NP} & \frac{\partial \dot{NG}}{\partial P3} & \frac{\partial \dot{NG}}{\partial P41} & \frac{\partial \dot{NG}}{\partial P45} \\ \frac{\partial \dot{NP}}{\partial NG} & \frac{\partial \dot{NP}}{\partial NP} & \frac{\partial \dot{NP}}{\partial P3} & \frac{\partial \dot{NP}}{\partial P41} & \frac{\partial \dot{NP}}{\partial P45} \\ \frac{\partial \dot{P3}}{\partial NG} & \frac{\partial \dot{P3}}{\partial NP} & \frac{\partial \dot{P3}}{\partial P3} & \frac{\partial \dot{P3}}{\partial P41} & \frac{\partial \dot{P3}}{\partial P45} \\ \frac{\partial \dot{P41}}{\partial NG} & \frac{\partial \dot{P41}}{\partial NP} & \frac{\partial \dot{P41}}{\partial P3} & \frac{\partial \dot{P41}}{\partial P41} & \frac{\partial \dot{P41}}{\partial P45} \\ \frac{\partial \dot{P45}}{\partial NG} & \frac{\partial \dot{P45}}{\partial NP} & \frac{\partial \dot{P45}}{\partial P3} & \frac{\partial \dot{P45}}{\partial P41} & \frac{\partial \dot{P45}}{\partial P45} \end{bmatrix}$$

$$\bar{b} = \begin{bmatrix} \frac{\partial \dot{NG}}{\partial W_f} \\ \frac{\partial \dot{NP}}{\partial W_f} \\ \frac{\partial \dot{P3}}{\partial W_f} \\ \frac{\partial \dot{P41}}{\partial W_f} \\ \frac{\partial \dot{P45}}{\partial W_f} \end{bmatrix}$$

The model containing the nonlinear volume dynamics approximation is represented by the two turbine-speed degrees-of-freedom.

For a further comparison, a third linear model was created by eliminating the states corresponding to the volume dynamics in the five-degree-of-freedom model. Order reduction was performed by setting the state derivatives $\dot{P}3$, $\dot{P}41$, and $\dot{P}45$ to zero and solving the equations for the remaining two states.

Stability derivatives were extracted from the nonlinear simulations by suppressing all integrations after trimming the simulation at a desired operating condition. Each state or control was then individually perturbed and the effects of its change were determined in the state derivatives at the input of each integrator. The central-difference extraction method that was used perturbs each state or control variable in both positive and negative directions. A perturbation step-size of plus or minus two percent of equilibruim conditions was considered to be adequate based on the rotor speed deviations experienced by current-generation helicopters. During the derivative extraction process, the rotor was allowed to reach a new equilibrium after each perturbation to eliminate dynamics of the rotor blade lag degree-of-freedom. The rotor was allowed to rotate an exact-integer number of revolutions between extractions, resulting in rotor blade azimuths which were unchanging for each extraction. In this way, first harmonic changes of required torque which occur in blade-element rotor simulations were eliminated from the linear model.

For a linear representation of the dynamics of the applied load, the small-perturbation extraction method was applied to the Gen Hel UH-60A blade-element helicopter simulation. A model consisting of two linear elements was used. A derivative representing the change of load torque with respect to power turbine speed was used to model steady-state change of torque with a change of rotor speed. The change of load torque with respect to power turbine acceleration was also needed to model the rotor inertia which manifests itself as a shear force transient at the rotor hub lag-hinge.

$$\Delta Q_{req} = \frac{\partial Q_{req}}{\partial NP}\Delta NP + \frac{\partial Q_{req}}{\partial \dot{NP}}\Delta \dot{NP} \tag{55}$$

The term Q_{req} is defined as load or "required" torque with respect to power turbine speed. All vehicle simulation load contributions are included in the required torque term.

$$Q_{req} = Q_{mr} + Q_{tr} + Q_{acc} + Q_{damp} \tag{56}$$

Engine output torque is assumed to be a linear function of NP, the other states, and the fuel flow, W_f.

$$\Delta Q_{eng} = \sum \frac{\partial Q_{eng}}{\partial x_j}\Delta x_j + \frac{\partial Q_{eng}}{\partial NP}\Delta NP + \frac{\partial Q_{eng}}{\partial W_f}\Delta W_f \tag{57}$$

where x_j represents the remaining four states. For the two-degree-of-freedom model extraction, x_j represents the gas-generator-turbine speed state.

Coefficients of the NP equation were determined by relating the change in angular speed to the net torque.

$$\Delta \dot{NP} = (\Delta Q_{eng} - \Delta Q_{req})/J \tag{58}$$

The moment of inertia, J, is the sum of inertias of the power turbine, drive train, and rotor hub. Rotor blade inertias are not included in J; effects of these inertias are reflected in the $\frac{\partial Q_{req}}{\partial NP}$ term. A linear equation may be written for $\Delta \dot{NP}$ in terms of the extracted derivatives and the state perturbations.

$$\Delta \dot{NP} = \frac{1}{1 + \frac{1}{J}\frac{\partial Q_{req}}{\partial NP}} \left\{ \frac{1}{J} \sum \frac{\partial Q_{eng}}{\partial x_j}\Delta x_j + \frac{1}{J}\left(\frac{\partial Q_{eng}}{\partial NP} - \frac{\partial Q_{req}}{\partial NP}\right)\Delta NP + \frac{1}{J}\frac{\partial Q_{eng}}{\partial W_f}\Delta W_f \right\} \tag{59}$$

The resulting elements of the state and control matrices for the power-turbine speed state are

$$A_{2,j} = \frac{\frac{\partial Q_{eng}}{\partial x_j}}{J + \frac{\partial Q_{req}}{\partial NP}}, j = 1, 3 - 5 \tag{60}$$

$$A_{2,2} = \frac{\frac{\partial Q_{eng}}{\partial NP} - \frac{\partial Q_{req}}{\partial NP}}{J + \frac{\partial Q_{req}}{\partial NP}} \tag{61}$$

$$b_2 = \frac{\frac{\partial Q_{eng}}{\partial W_f}}{J + \frac{\partial Q_{req}}{\partial NP}} \tag{62}$$

Although it is not a complete model of the dynamics of the rotor and drive train, this linear load representation is adequate to model the large-scale changes of required power about a trim flight condition. Because the rotor system and drive train are modeled with a single degree of freedom, the effects of blade lagging and first harmonic variations in required torque are not represented. It is usable over the full range of the helicopter simulation, and is therefore useful in illustrating the changes of engine dynamics over the operating envelope of the aircraft.

A comparison of the simulation and the linear models for a high-power flight condition is shown in figure 4. Both the complete five-degree-of-freedom and the two-degree-of-freedom perturbation models are good represention of engine response. Errors associated with changes in trim are small, and transient responses of internal engine states are reproduced well. The reduced-order linear model response is nearly identical to that of the extracted linear models. Note that higher-order dynamics can be seen in the simulation power turbine response. This is a result of neglecting rotor-blade lag dynamics and the effects of rotor azimuthal variation in the linear rotor-load representation.

Appendix B gives the extracted small-perturbation models for three typical flight conditions. Reference 1 suggests that high-power conditions correspond to a more linear engine response, resulting in a more accurate linear model. For the T700 implementation, low power response was found to be quite linear, at least to power levels corresponding to the UH-60A bucket speed (trim condition 2 of Appendix B). At lower power levels which occur in a near-autorotative descent flight condition (trim condition 3), engine response is slightly less linear.

Eigenvalues of the linear models for three trim conditions are shown in table 1. The five-degree-of-freedom extracted model consists of five stable, nonoscillatory modes. The power turbine state is completely decoupled from the other states. The neglected dynamics of the simplified load representation therefore have no effect on the gas-generator turbine or volume dynamics. Three modes, corresponding to the pressure states, are outside the bandwidth of interest for the modeling of rotor and propulsion system dynamics. These modes are well above the second drive-train torsional mode and the rotor blade first in-plane elastic mode of a typical helicopter. Also, the reduced-order two-state model eigenvalues are seen to be in good agreement with those of the extracted two-state model. The volume dynamics approximation is therefore considered to be valid for real-time and nonreal-time engine dynamic modeling.

Effects of Heat-Sink Dynamics

Inclusion of station 4.1 heat-sink effects in the small perturbation model requires the addition of an extra state. This state, gas temperature at station 4.1, is related to temperature without heat-sink dynamics by

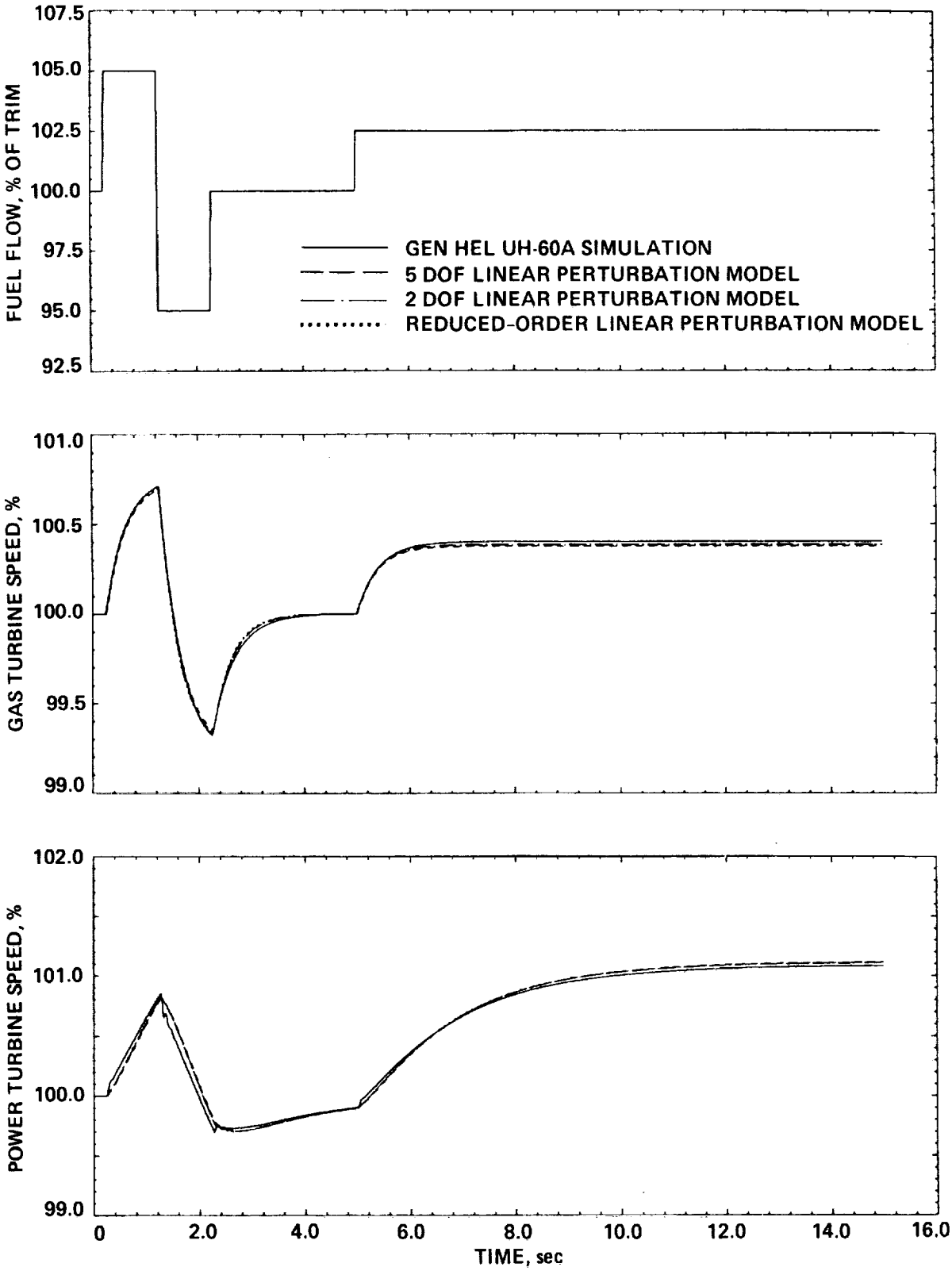

Figure 4: Comparison of the linear perturbation models with the nonlinear simulation for a high-power flight condition.

Trim Condition	Mode	5-DOF Model	2-DOF Model	Reduced-Order 5-DOF Model
1	NG	-2.66	-2.69	-2.81
	NP	-0.565	-0.565	-0.565
	$P3$	-51.6		
	$P41$	-4900.		
	$P45$	-3060.		
2	NG	-2.08	-2.23	-2.16
	NP	-0.446	-0.446	-0.446
	$P3$	-52.2		
	$P41$	-4640.		
	$P45$	-4040.		
3	NG	-1.75	-1.82	-1.83
	NP	-0.357	-0.357	-0.357
	$P3$	-52.6		
	$P41$	-4430.		
	$P45$	-4530.		

Table 1: Eigenvalues of two extracted perturbation models and the reduced-order model.

$$\frac{T41}{T41_{ns}} = \frac{\tau_1 s + 1}{\tau_2 s + 1} \tag{63}$$

for small perturbations about trim. The temperature with no dynamics, $T41_{ns}$, is a function of the other five states. For extraction from the nonlinear simulation, $T41$ dynamics may be expressed in the form

$$\Delta\dot{T41} = -\frac{1}{\tau_2}\Delta T41 + \frac{\tau_1}{\tau_2}\Delta\dot{T41}_{ns} + \frac{1}{\tau_2}\Delta T41_{ns} \tag{64}$$

where

$$\Delta T41_{ns} = \sum \frac{\partial T41_{ns}}{\partial x_i}\Delta x_i + \frac{\partial T41_{ns}}{\partial W_f}\Delta W_f$$

$$\Delta\dot{T41}_{ns} = \sum \frac{\partial T41_{ns}}{\partial x_i}\Delta \dot{x}_i + \frac{\partial T41_{ns}}{\partial W_f}\Delta \dot{W}_f$$

During derivative extraction, $T41$ was held fixed at the trim value and the change in $T41$ was determined for each state perturbation. The time constants τ_1 and τ_2 are those values corresponding to the trim operating condition. The six-degree-of-freedom linear representation is equal to

$$F_1\dot{\bar{x}} = F_2\bar{x} + G_1 W_f + G_2\dot{W}_f \tag{65}$$

where

$$\overline{x} = \begin{Bmatrix} NG \\ NP \\ P3 \\ P41 \\ P45 \\ T41 \end{Bmatrix}$$

$$F_1 = \begin{bmatrix} 1 & 0 & 0 & 0 & 0 & 0 \\ 0 & 1 & 0 & 0 & 0 & 0 \\ 0 & 0 & 1 & 0 & 0 & 0 \\ 0 & 0 & 0 & 1 & 0 & 0 \\ 0 & 0 & 0 & 0 & 1 & 0 \\ -\frac{\eta}{\tau_2}\frac{\partial T41_{ns}}{\partial NG} & -\frac{\eta}{\tau_2}\frac{\partial T41_{ns}}{\partial NP} & -\frac{\eta}{\tau_2}\frac{\partial T41_{ns}}{\partial P3} & -\frac{\eta}{\tau_2}\frac{\partial T41_{ns}}{\partial P41} & -\frac{\eta}{\tau_2}\frac{\partial T41_{ns}}{\partial P45} & 1 \end{bmatrix}$$

$$F_2 = \begin{bmatrix} \frac{\partial \dot{NG}}{\partial NG} & \frac{\partial \dot{NG}}{\partial NP} & \frac{\partial \dot{NG}}{\partial P3} & \frac{\partial \dot{NG}}{\partial P41} & \frac{\partial \dot{NG}}{\partial P45} & \frac{\partial \dot{NG}}{\partial T41_{ns}} \\ \frac{\partial \dot{NP}}{\partial NG} & \frac{\partial \dot{NP}}{\partial NP} & \frac{\partial \dot{NP}}{\partial P3} & \frac{\partial \dot{NP}}{\partial P41} & \frac{\partial \dot{NP}}{\partial P45} & \frac{\partial \dot{NP}}{\partial T41_{ns}} \\ \frac{\partial \dot{P3}}{\partial NG} & \frac{\partial \dot{P3}}{\partial NP} & \frac{\partial \dot{P3}}{\partial P3} & \frac{\partial \dot{P3}}{\partial P41} & \frac{\partial \dot{P3}}{\partial P45} & \frac{\partial \dot{P3}}{\partial T41_{ns}} \\ \frac{\partial \dot{P41}}{\partial NG} & \frac{\partial \dot{P41}}{\partial NP} & \frac{\partial \dot{P41}}{\partial P3} & \frac{\partial \dot{P41}}{\partial P41} & \frac{\partial \dot{P41}}{\partial P45} & \frac{\partial \dot{P41}}{\partial T41_{ns}} \\ \frac{\partial \dot{P45}}{\partial NG} & \frac{\partial \dot{P45}}{\partial NP} & \frac{\partial \dot{P45}}{\partial P3} & \frac{\partial \dot{P45}}{\partial P41} & \frac{\partial \dot{P45}}{\partial P45} & \frac{\partial \dot{P45}}{\partial T41_{ns}} \\ \frac{1}{\tau_2}\frac{\partial T41_{ns}}{\partial NG} & \frac{1}{\tau_2}\frac{\partial T41_{ns}}{\partial NP} & \frac{1}{\tau_2}\frac{\partial T41_{ns}}{\partial P3} & \frac{1}{\tau_2}\frac{\partial T41_{ns}}{\partial P41} & \frac{1}{\tau_2}\frac{\partial T41_{ns}}{\partial P45} & -\frac{1}{\tau_2} \end{bmatrix}$$

$$G_1 = \begin{bmatrix} \frac{\partial \dot{NG}}{\partial W_f} \\ \frac{\partial \dot{NP}}{\partial W_f} \\ \frac{\partial \dot{P3}}{\partial W_f} \\ \frac{\partial \dot{P41}}{\partial W_f} \\ \frac{\partial \dot{P45}}{\partial W_f} \\ \frac{1}{\tau_2}\frac{\partial T41_{ns}}{\partial W_f} \end{bmatrix}$$

$$G_2 = \begin{bmatrix} 0 \\ 0 \\ 0 \\ 0 \\ 0 \\ \frac{n}{n_2}\frac{\partial T41_{ss}}{\partial W_f} \end{bmatrix}$$

The model may be expressed in standard state-equation form with the following transformation (as derived by Chen).

$$\dot{\bar{z}} = A\bar{z} + \bar{b}W_f \tag{66}$$

$$\bar{x} = C\bar{z} + \bar{d}W_f \tag{67}$$

where

$$A = F_1^{-1}F_2$$

$$\bar{b} = F_1^{-1}G_1 + FF_1^{-1}G_2$$

$$C = I$$

$$\bar{d} = F_1^{-1}G_2$$

Figure 5 illustrates the importance of the use of a station 4.1 heat-sink model. Response is significantly slowed compared to the five-degree-of-freedom model. The overall effect of the heat-sink representation is a larger variation of rotor shaft speed and decreased closed-loop system stability. Analysis-oriented simulations such as the performance standard component-model program developed by the engine manufacturer also model a heat sink effect at station 4.5. Because its influence was found to be small, the station 4.5 heat-sink effect is not represented in the real-time model. Figures B7 through B12 present the six-degree-of-freedom extracted linear models and three-state extracted models which contain the volume dynamics approximation for the three flight conditions.

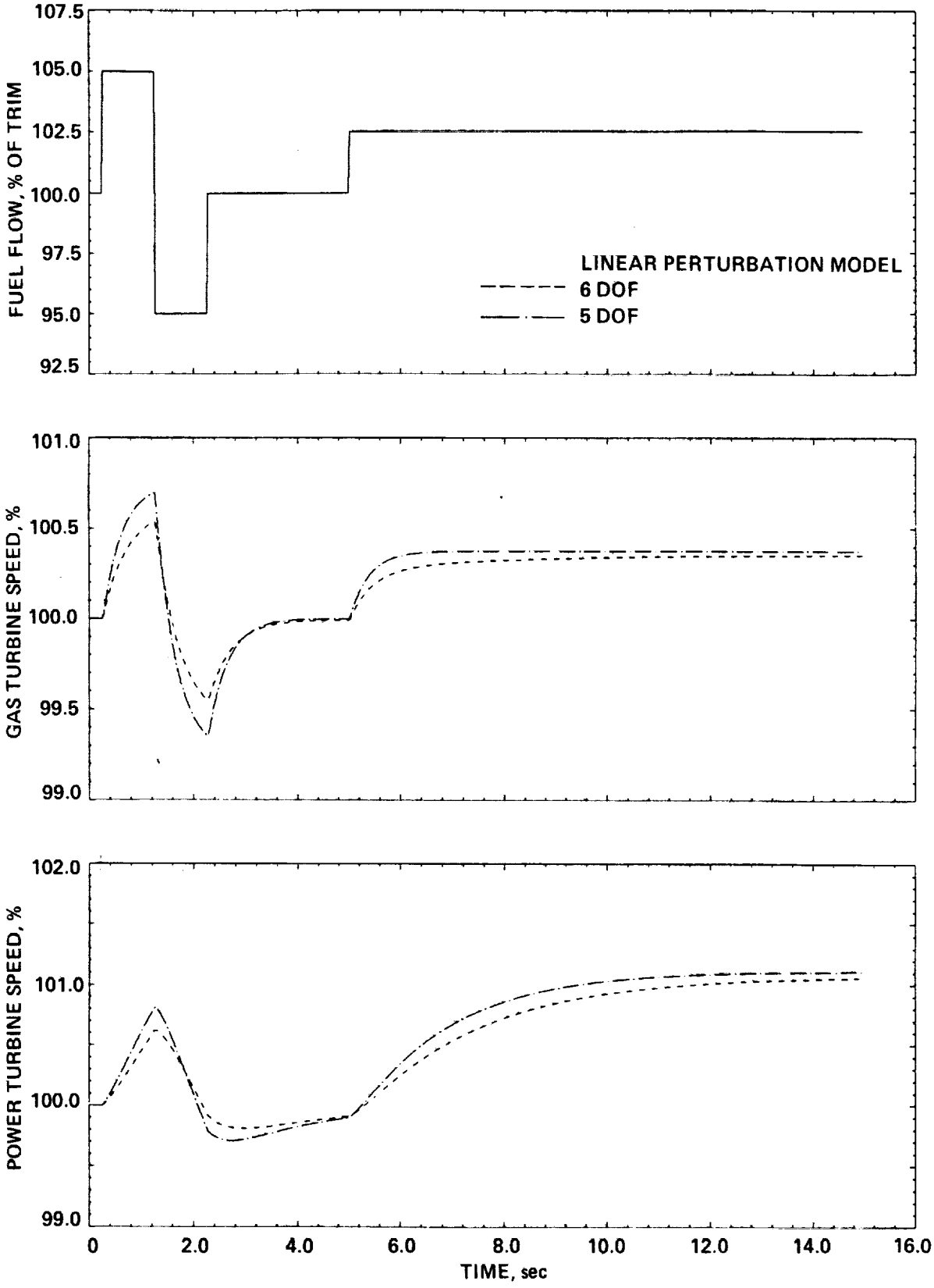

Figure 5: Linear model responses at a high-power flight condition with and without station 4.1 heat-sink model.

Real-Time Modeling Considerations

The requirement for real-time operation imposes severe requirements on a component model and its program structure. Real-time component models are by necessity simplified from more sophisticated component simulations which are used for design or analysis purposes. Although the simplified component model is based on the physics of each process within the engine cycle, any detail which is found to have no significant effect on operation or response must be removed in order to minimize computing time. The digital implementation of a real-time model is constrained by the intended use of the model and the capabilities of the processor used. Typical restrictions that have been used in previous real-time models are the use of third-order polynomial curve fits for nonlinear functions, the use of integer exponents and square roots only, and allowing no iteration between time steps (ref. 12). Furthermore, because complete rotorcraft simulations involve considerable computational demands, only a small percentage of the available computation time can be devoted to the propulsion system. On the positive side, the increasingly higher computational capabilities of state-of-the-art hardware allows some of the more severe restrictions to be relaxed. Present implementation restrictions at Ames require a minimum amount of multiple-pass coding or iteration and the use of the Ames simulation-standard function table processor routines as much as possible. Also, Ames host computers are operated asynchronous to peripheral hardware such as the image-generation computers. The time-step size is determined for a given simulation depending on computer speed and the amount of peripheral computer system loading. Simulations must therefore be designed to be independent of time step size, the only specifiable restrictions being maximum or minimum allowed values.

The omission of dynamic states results in sets of coupled algebraic equations which describe the pressures at each station in terms of pressures at the other stations. Because the equations are not linear, they may not be solved analytically. A real-time simulation must therefore solve the equations using iteration methods unless a form of preprocessing is used. However, excessive amounts of iteration must be avoided to limit computational demands. Iteration also results in poor computational efficiency because the time-step size must be chosen based on the number of iterations needed for the most extreme transient conditions.

Two previously used methods rely on a one-pass iteration scheme to achieve the necessary computational efficiency. They employ fixed-point iteration with a form of convergence technique. Once the convergence has been verified as adequate, the iteration loop is eliminated and the updated values are used in the following time interval. A method used at NASA Lewis was developed from hybrid computer applications (refs. 9 and 10). Convergence of the iteration is forced by inserting a first-order lag with a small time constant between previously calculated values and values to be used in the next time interval. The lag may be expressed in the z-domain as

$$\frac{x_{n+1}}{x_n} = \frac{Kz}{z - e^{-K\Delta t}} \tag{68}$$

where the convergence gain, K, is variable, with higher values resulting in faster convergence but with lower margins of stability. While having the advantages of simplicity and efficiency, the method was found to give poor results under large power-transient operation as experienced by small turboshaft engines. Stability is also lowered under low-power conditions.

The second method (refs. 11 and 12) refines the one-step iteration procedure by using a redundant continuity equation to obtain a mass-flow error term. This term is then multiplied by a coefficient derived from a set of predetermined partial derivatives. The resulting value is used in the next time interval as an acceptable estimate of mass flow. The method has the advantages of speed of calculation and stability over

a wide range of operation. When applied to a large turbofan engine, the difference from a full iteration method was less than one percent for severe ramp inputs (ref. 11). However, the user has no control over the amount of error which is produced. Also, a change of time step will directly affect the magnitude of the error. An alternative approach which allows the user to specify the level of acceptable error was therefore employed.

Real-Time Iteration Solution

The real time iteration solution presented here was found to produce acceptable transient response while executing in real time on a high-speed computer. It has been executed successfully in conjunction with the Gen Hel UH-60A simulation using a CDC 7600 computer and an Ames-developed real-time operating system.

A fixed-point iteration was used to solve the nonlinear algebraic equations. Because multiple passes are required to determine elements of the Jacobian for quadratic convergence methods, they were found to involve more computation than linearly convergent methods. The equations were expressed recursively in the form

$$x_{(n)} = f(x_{(n-1)}) \tag{69}$$

The iteration solution is unique and convergent provided that the Lipschitz condition

$$|f(x_{(n-1)}) - f(x_{(n)})| \leq L|x_{(n-1)} - x_{(n)}| \tag{70}$$

is satisfied with a value of the Lipschitz constant, L, less than 1. Convergence of the iteration was controlled with the use of the successive overrelaxation method. For each iteration, the value of pressure state x was modified by its previous value.

$$x_{(n)} = x_{(n-1)} + R \cdot [f(x_{(n)}) - x_{(n-1)}] \tag{71}$$

Values of the relaxation parameter, R, less than 1 cause slower convergence, resulting in greater stability. A value of R was chosen to allow monotonic convergence over the operating range of the engine.

Two nested algebraic loops are present in the representation of pressures $P3$ and $P41$. The outer loop arises from the calculation of compressor mass flow which is indirectly a function of pressure $P3$. The inner loop is a result of the interdependence of pressures across the combustor. The coupled equations are given by

$$\dot{P3} = 0 = K_{V3} \cdot T3 \cdot (WA3 - WA3_{bl} - WA31) \tag{72}$$

$$\dot{P41} = 0 = K_{V41} \cdot T41 \cdot (WA31 + W_f - W41) \tag{73}$$

Because the calculation of compressor flows involves a significant amount of computation, the outer loop was separated from the inner loop by assuming that the mass flow entering the combustor for a given interval is approximately equal to the mass flow leaving the compressor in the previous interval.

$$WA31_{(n)} \approx WA3_{(n)} - WA3_{bl(n-1)} \tag{74}$$

This outer loop proved to be strongly convergent. This was verified by examining the value of the Lipschitz constant for extreme transient operating cases. With a sufficiently small time step, one iteration of the outer loop produces near-equilibrium results. However, the approximation results in a value of iteration error which is a function of the time step. The time step must therefore be kept as small as possible to achieve minimum error and acceptable transient response.

The inner loop was then solved iteratively with algebraic equations modified for efficient computation. An expression for $P3$ is obtained from the combustor equation.

$$P3^2 - P3 \cdot P41 - K_{dpb} \cdot T3 \cdot WA31^2 = 0 \tag{75}$$

Solving for $P3$, the physically realizable, positive real root corresponds to

$$P3 = \frac{1}{2}\left(P41 + \sqrt{P41^2 + 4 \cdot K_{dpb} \cdot T3 \cdot WA31^2}\right) \tag{76}$$

From the coupled $\dot{P}41$ equation another expression for WA31 is obtained.

$$WA31 = W41 - W_f \tag{77}$$

The combustor equation is then solved for $P41$. Substituting the above expression for $WA31$, solving the choked nozzle equation for $W41$, and substituting results in the following expression for $P41$.

$$P41 = P3 - \frac{T3 \cdot K_{dpb} \cdot \left(\frac{K_{WCT} \cdot P41}{\sqrt{\theta_{41}}} - W_f\right)^2}{P3} \tag{78}$$

A fixed-point iteration was then used to solve the two equations for $P3$ and $P41$. The iteration converges linearly, with a total of eleven arithmetic operations required for each pass. No relaxation algorithm is required for convergence. Under the most extreme conditions, up to ten iterations may be required for convergence with less than 0.1 percent error, resulting in a total of 110 arithmetic operations.

Pressure upstream of the power turbine, $P45$, may be solved independently of the other pressures, but because it is a nonlinear function of its own value, iterative techniques must be used. The quasi-static approximation is made by setting the derivative of $P45$ to zero. The continuity equation relates mass flows at station 4.5.

$$\dot{P45} = 0 = K_{V45} \cdot T45 \cdot (W41 - W45 + B_3 B_4 WA2) \tag{79}$$

Substituting the expressions for mass flow at station 4.5, the iteration function is given by

$$P45 = \frac{(W41 + B_3 B_4 WA2)\sqrt{\theta_{45}}}{f_9\left(\frac{P_a 9}{P45}\right)} \tag{80}$$

The numerator is a constant over the iteration. A total of four arithmetic operations and one function-table look-up is used for each iteration. Stability and speed of execution were tested under extreme conditions of an instantaneous step in fuel flow from flight idle to full power. Eight iterations resulted in an error equal to less than 0.1 percent of the steady-state value.

The iteration method presented offers some advantages over other methods which may involve preprocessing or altering of volume dynamics. All functional relationships describe physical processes between thermodynamic or mechanical states of the components. Hence, engine performance can be altered by adjustment of these functions. No preprocessing programs are required. An equilibrium solution

may be obtained within a specified error tolerance. Because of the opened compressor mass-flow iteration, however, response is dependent on time step. For the T700 implementation, a restriction on time step to a maximum value of 10 msec was established based on a maximum allowable error of 0.1 percent between time steps.

Pressure Function Table Solution

A further method is being investigated which has the advantage of removing all real-time iteration, thereby relaxing the severe time-step size requirements associated with the iteration solution. A preprocessing program is used to tabulate steady-state values of pressure at station 4.1 as a function of fuel flow, the inlet conditions, temperature at station 4.1, and gas generator speed. Because of the use of the heat-sink model, station 4.1 temperature must be an independent input to the function table. A table look-up method is then used in real-time execution. Pressures at stations 3 and 4.5 are determined as functions of fuel flow and pressure at station 4.1. The method involves no loss of generality. It has been found to be valid for large time steps, thereby alleviating computer speed requirements and allowing multiple-engine installations for real-time execution. The major disadvantage is the requirement for storage of the station 4.1 pressure table, which involves thousands of data points. The method also requires the use of a preprocessing program, thus preventing on-line modification to the compressor mass-flow and turbine-energy functions.

FUEL CONTROL SYSTEM MODEL

The real-time digital implementation of the fuel control system consists of simplified versions of the ECU and the HMU and models of pressure, temperature, torque, and speed sensors. Collective pitch rigging to the load demand spindle for the UH-60A implementation is also provided. Each of these is modeled as an explicit entity such that all interfaces between components represent interfaces in the actual control system. Simplifications were made by eliminating models and control logic which are beyond the scope of real-time simulation requirements or are not needed because of simplifications to the engine model. Eliminated model features include automatic engine start-up capability, fuel control below flight-idle power, position control of the variable-geometry inlet-guide-vanes, redundancy models, and redundancy model logic. The complete fuel control system model is presented in Appendix C.

VALIDATION

The model was validated by comparison of static trim performance and dynamic response with available information, which was provided by GF and NASA Lewis.

Static Trim

Steady-state simulation performance was verified to be within normal limits of operation by comparison with data supplied from two computer simulations developed by the engine manufacturer. The GE status-81 model is a comprehensive analysis-oriented model which is used for detailed representation of the engine thermodynamic cycle. The GE unbalanced torque model is a simplified model which is optimized

to reproduce engine dynamics for control system design purposes. Maps of trim characteristics of the three models are provided in figures 6 through 8. In all cases, the real-time model displays an acceptable steady-state performance. Figure 6 is a plot of gas generator speed as a function of fuel flow. The steady-state operation of the real-time model is bounded by the two analysis models over the range of operation except between 81 and 86 percent of gas generator speed. In this area, the real-time model tends to overestimate fuel consumption by as much as five percent. At higher gas generator speeds, the real-time model displays the characteristic of the GE unbalanced torque model, requiring less fuel for a given fuel flow than the GE status-81 model. Because of the limits of the data supplied in the real-time model functional relations, the maximum gas generator speed for which the model is valid is 100 percent. This is adequate for the intended use of the model because the fuel control system prevents steady-state operation outside of this range. Figure 7 is a plot of horsepower as a function of fuel flow. The real-time model displays agreement with the status-81 model over the entire operating range of the engine. The unbalanced torque model shows less available horsepower for a given fuel flow at high power levels. Static pressure at station 3, an input to the control system, is shown as a function of gas generator speed in figure 8. The same trends shown in figure 6 are seen, with the real-time model showing closer agreement with the unbalanced torque model over most of the range of operation.

A comparison with available data from the experimental engine operated by NASA Lewis is shown in tables 2 and 3. Table 2 gives the ambient conditions and loading for each test condition, and table 3 gives the resulting trim operating conditions for the engine and the real-time model. The experimental engine is a prototype model which does not reproduce specification engine performance. Because of this, compressor-mass-flow and turbine-energy functions derived from this test engine were used in place of the standard functions which represent specification performance. These functions were supplied by NASA Lewis. For the six cases, the inlet and exhaust conditions, fuel flow, and load conditions were specified so that internal states could be compared. During the tests, the dynamometer load torque was adjusted to obtain a specified power turbine speed. The model power turbine speed was allowed to vary in order to achieve trim with the test load torque. Fair agreement is seen in the medium- and high-power test cases (cases 3 through 6). The real-time model tends to overestimate power output by a small percentage in all cases. Internal temperatures and pressures agree very well. At lower power settings, agreement is poorer. The model overestimates gas generator speed by 4 percent in case 1. Although the model is not valid for such low power turbine speeds, the major difference seen in these speeds is caused by the difference in gas generator speeds and not in the power turbine model.

Dynamic Response

Open loop response was validated by comparison with the GE performance-standard status-81 simulation. Time history simulation data were provided by GE for large-step fuel flow inputs. The simulated load was a simple model representing the dynamometer used for testing of the NASA-Lewis experimental engine. The load is variable, based on a simulated collective-pitch control input which was used to trim the power turbine at the design speed for a specified fuel flow. Because of differences in sophistication of the two simulations in modeling of off-design power turbine speeds, the power turbine speeds were held constant by suppressing the NP integration. Output torque was therefore used as a measure of engine power. Some results are presented in figures 9 and 10.

As shown in figure 9, the two simulations are in close agreement for a step increase from midpower to high power. Gas generator speed is overestimated by 1 to 2 percent; this is reflected in the trim differences between the real-time model and the status-81 model in figure 6. Trim values of station 4.1 and 4.5

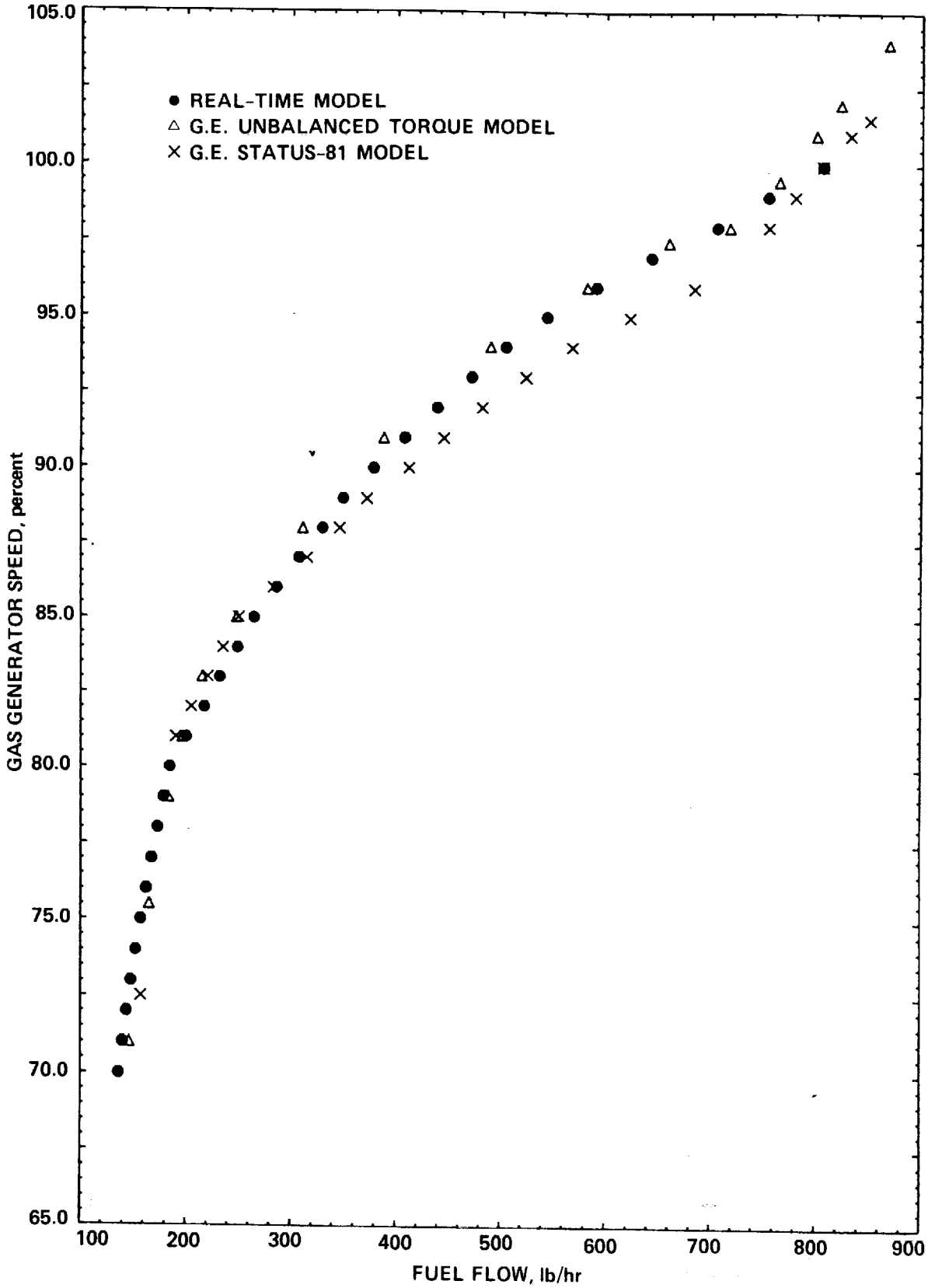

Figure 6: T700 gas generator speed vs. fuel flow for three simulation models at sea-level standard atmosphere conditions.

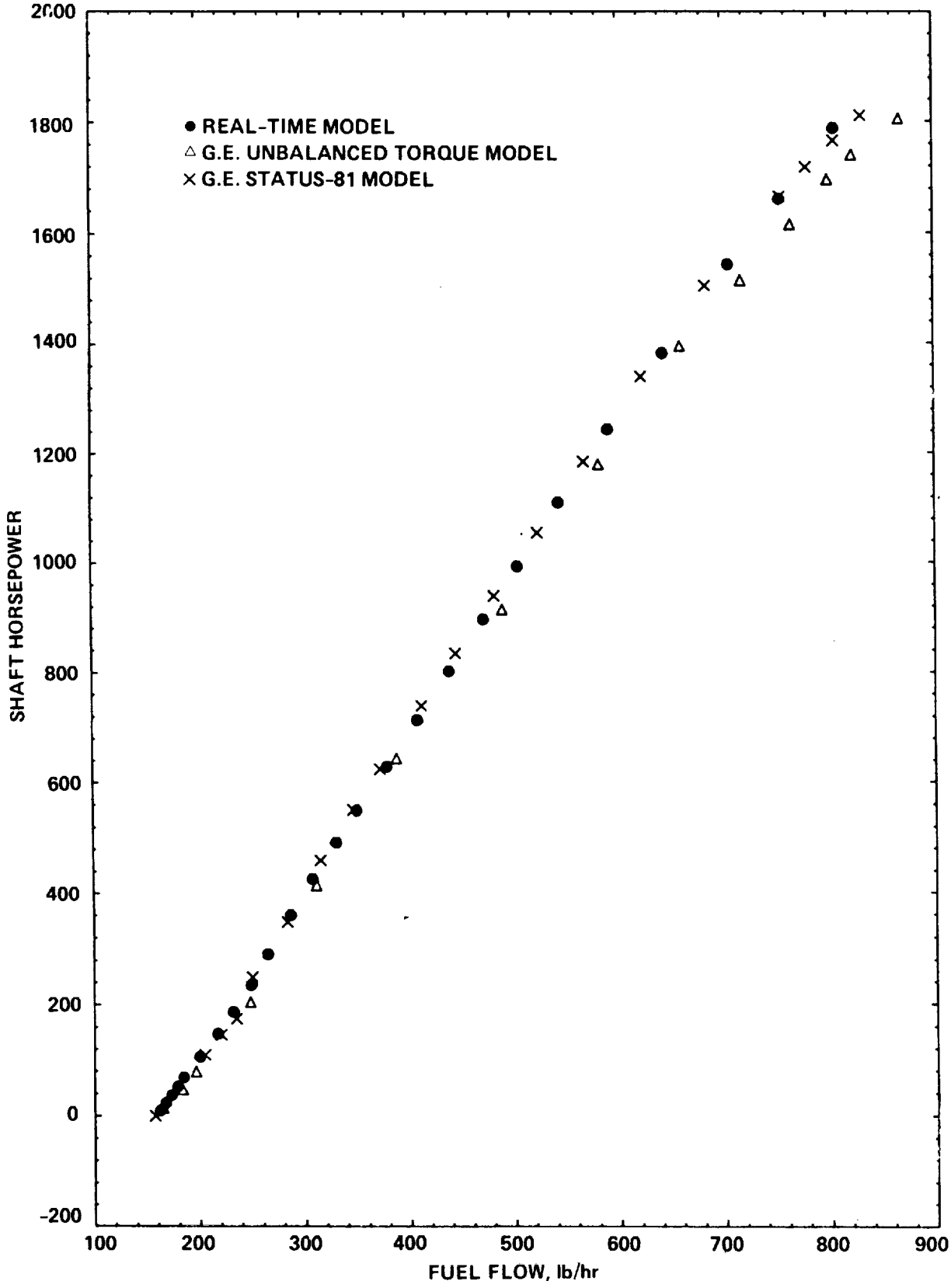

Figure 7: T700 horsepower vs. fuel flow for three simulation models at sea-level standard atmosphere conditions.

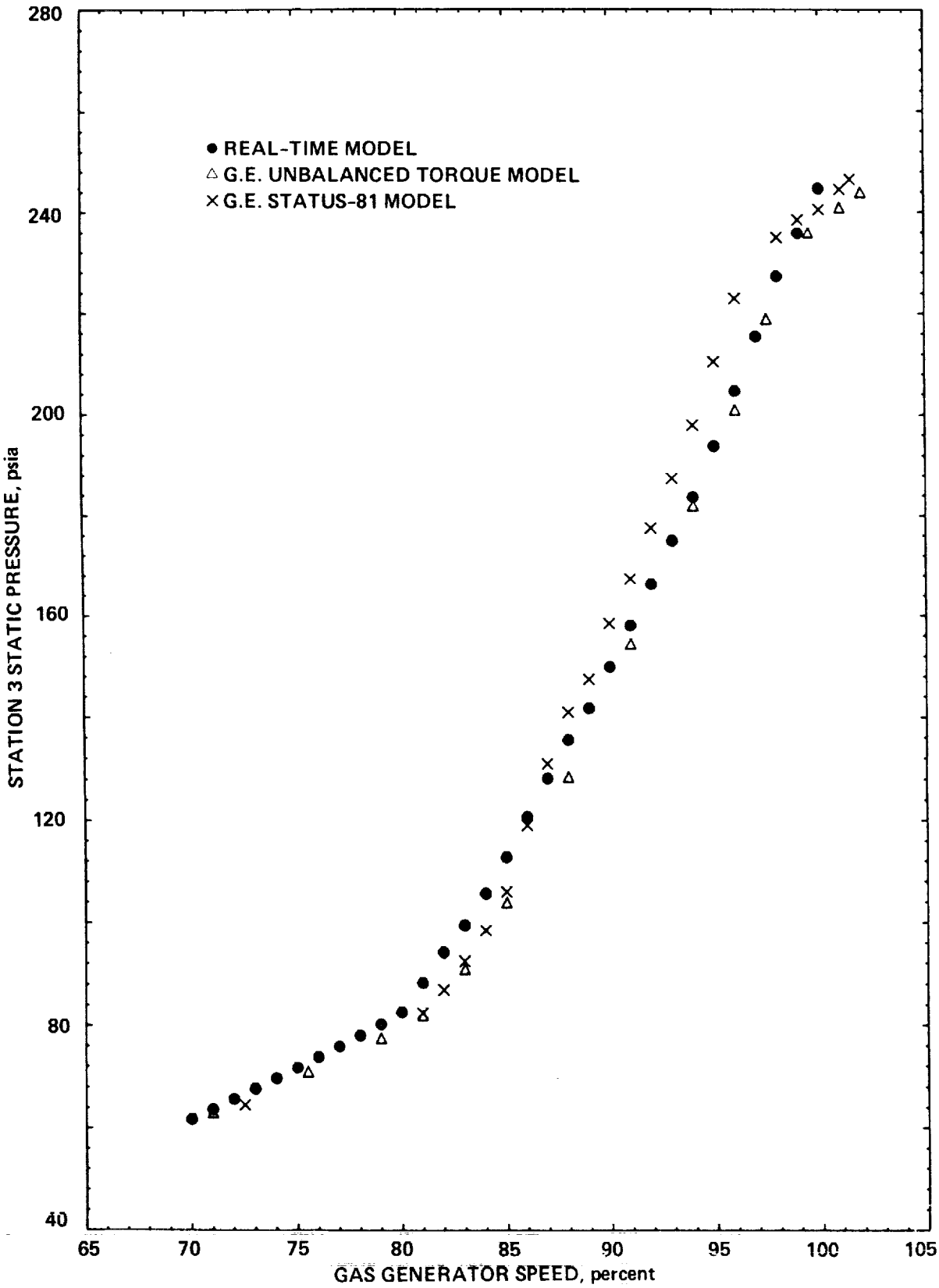

Figure 8: T700 station 3 static-pressure vs. gas-generator speed for three simulation models at sea-level standard atmosphere conditions.

Test Case	W_f lb_m/hr	$P2$ $PSIA$	$T2$ $°R$	$P49$ $PSIA$	Load Torque $ft - lb_f$
1	140.1	14.37	516.7	14.37	30.1
2	297.2	14.17	515.6	14.43	90.1
3	372.0	14.16	508.3	14.46	148.3
4	458.4	14.09	508.0	14.60	206.5
5	560.6	14.02	507.2	14.63	274.3
6	694.4	13.92	507.2	14.72	360.8

Table 2: Test conditions for NASA-Lewis experimental test engine.

Test Case	Data Type	NG %	NP %	$WA2$ lb_m/sec	$P3$ $PSIA$	$T3$ $°R$	$T45$ $°R$
1	Experimental engine	65.9	52.6	3.20	58.0	832.0	1413.
	Real-time model	70.0	83.8	3.59	63.4	855.9	1372.
2	Experimental engine	84.7	95.7	5.16	113.1	1026.	1577.
	Real-time model	86.4	100.6	5.52	119.0	1043.	1555.
3	Experimental engine	87.7	95.7	6.16	139.0	1081.	1626.
	Real-time model	88.1	97.8	6.27	141.7	1084.	1629.
4	Experimental engine	90.4	95.7	6.92	161.1	1127.	1731.
	Real-time model	90.7	97.3	7.00	163.3	1130.	1734.
5	Experimental engine	92.6	95.7	7.66	184.8	1173.	1838.
	Real-time model	92.8	98.2	7.73	186.4	1178.	1855.
6	Experimental engine	95.9	95.7	8.50	211.9	1228.	1974.
	Real-time model	96.1	99.4	8.53	213.8	1233.	2009.

Table 3: Comparison of real-time model steady-state operation with NASA-Lewis test article. This does not represent specification T700 performance.

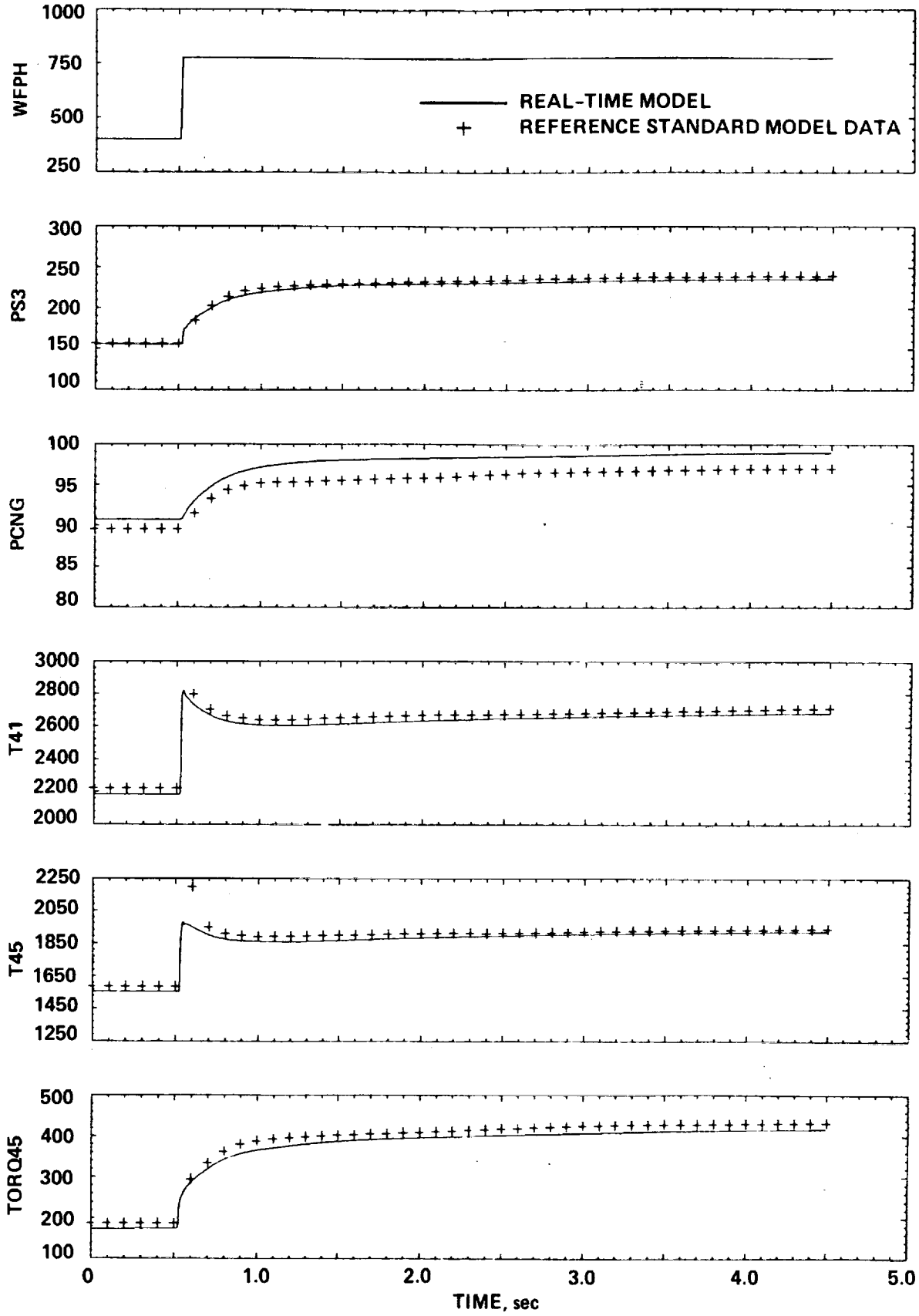

Figure 9: Response to a step increase in fuel flow from 400 to 775 lb_m per hour.

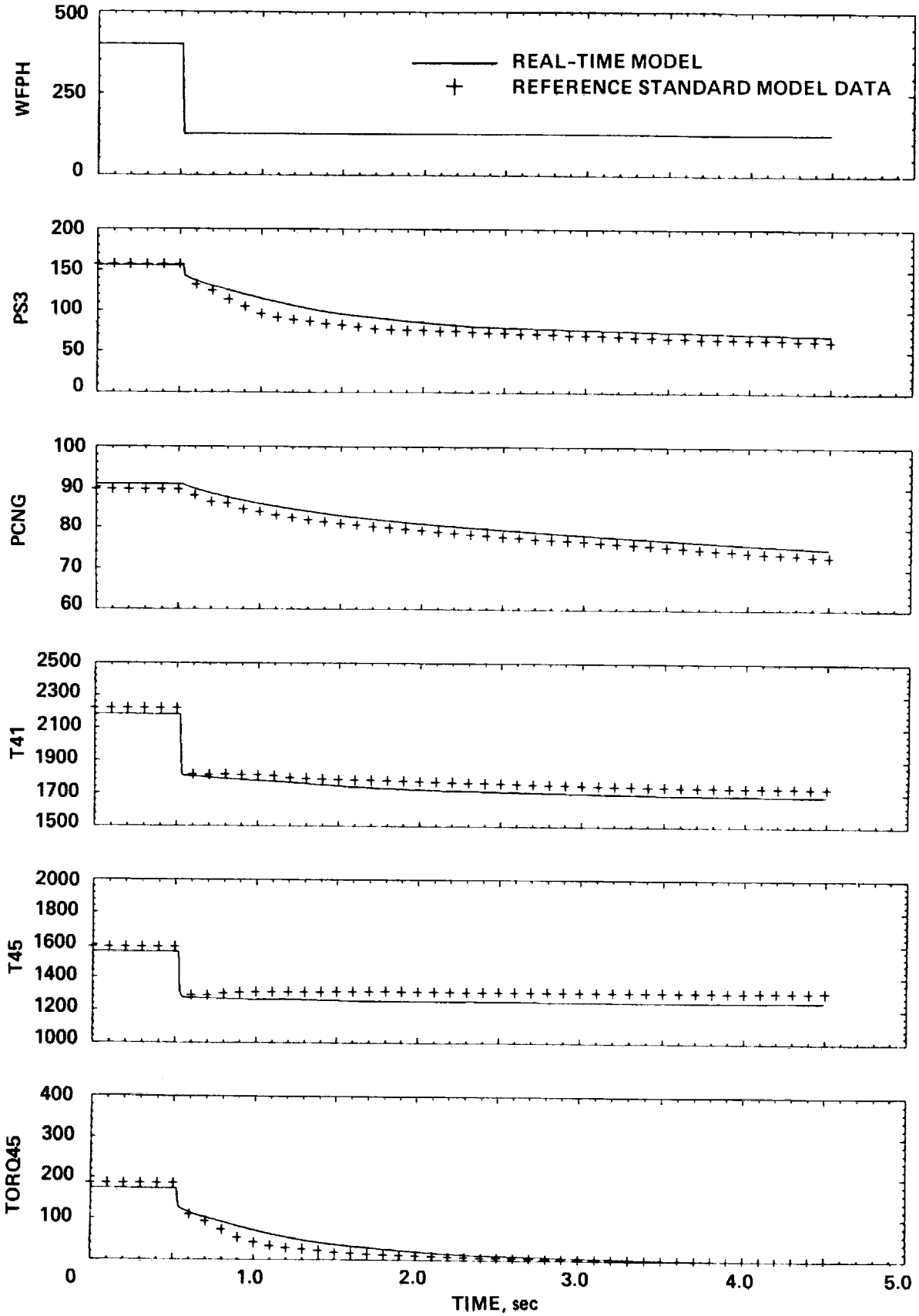

Figure 10: Response to a step decrease in fuel flow from 400 to 125 lb_m per hour.

temperature are slightly underestimated by the real-time program; this is a characteristic of the real-time model which was found for all validation cases. Output torque, station 3 static pressure, and temperature responses are in good agreement.

Low power engine performance is shown in figure 10, which represents a decrease in fuel flow to below-idle power. Gas generator dynamics are accurately represented. Other real-time model outputs display a slightly different dynamic characteristic, although zero torque is reached for both simulations at approximately the same time. The real-time model is initially less responsive. Under a simplifying assumption, the real-time heat-sink model constants were made independent of the direction of power change. Additional sophistication of the heat-sink representation may be warranted.

Closed-loop propulsion system response was validated by incorporating the engine and fuel control system into the real-time Gen Hel UH-60A helicopter simulation. The NASA-Ames version of this simulation is detailed in reference 13. This simulation contains a real-time blade-element main rotor system, a Bailey-type tail rotor model, and a rigid-shaft drive train model with simplified representations of accessory power requirements. A time step of 14 msec was used; this is a typical value for real-time execution of the blade-element rotor. In order to meet the cycling requirements of the iteration model, the T700 program was updated twice for each rotor routine cycle, or once every 7 msec. The power-turbine-speed degree of freedom corresponds to that of the drive train and rotor hub, and was therefore updated every 14 msec. Flight test data obtained from reference 14 was used for correlation. This data consists of single-axis control inputs to a vehicle with all stability augmentation disabled. The amplitudes of the inputs are small, typically not more than 15 percent of the control travel.

The correlation of secondary effects such as propulsion system response depends on adequate correlation of the vehicle and rotor system responses with the test data. Although the blade-element helicopter simulation is considered to be a high-fidelity model, differences do exist which are reflected in the engine and fuel-control-system responses. For all comparisons, the model configuration and test conditions were set up to match those of the flight tests. Time histories of the test-aircraft control inputs were used as direct inputs to the simulation. Constant biases were added to the control inputs to correct for small discrepancies between the test aircraft and the simulation trim positions. Therefore the simulation begins each transient response in trim and the incremental change in a control input is identical to that of the flight test. Details of the simulation comparison with the flight tests are given in reference 13.

An example of a single-axis collective input at high forward speed is shown in figure 11. The aircraft at a light gross weight was trimmed at an equivalent airspeed of 90 kts. Collective trim is in good agreement with that of the flight test. Power required by the aircraft is therefore correctly represented by the vehicle simulation. The output torque of both engines is shown by the second plot in the figure; this is in good agreement with test data for the initial trim. The trends displayed by the rotor speed time histories are correct. The data suggest that the test aircraft contains greater load demand compensation than the simulation, however, resulting in less rotor speed droop after the initial input. Gas generator speed and output torque time histories are also more responsive to the initial input. After the input, the test vehicle and simulation time histories diverged in pitch, with the vehicle reaching a 6-degree nose-up attitude at 6 seconds, while the simulation achieved a 2-degree nose-up attitude. The result of this is a rapidly-changing main rotor required-torque which prevents the test vehicle from regaining the trim rotor speed.

Figure 12 shows system response to a lateral cyclic control input at an airspeed of 55 knots. The lateral cyclic trim position is in good agreement with the test, while the collective trim position is slightly higher in the simulation. The engine torque is therefore higher. Again, a divergence in pitch attitude between the simulation and test data prevents a direct comparison at the end of the run. More rotor-speed droop is seen in the test data in response to the initial left cyclic input. The torque, gas generator turbine

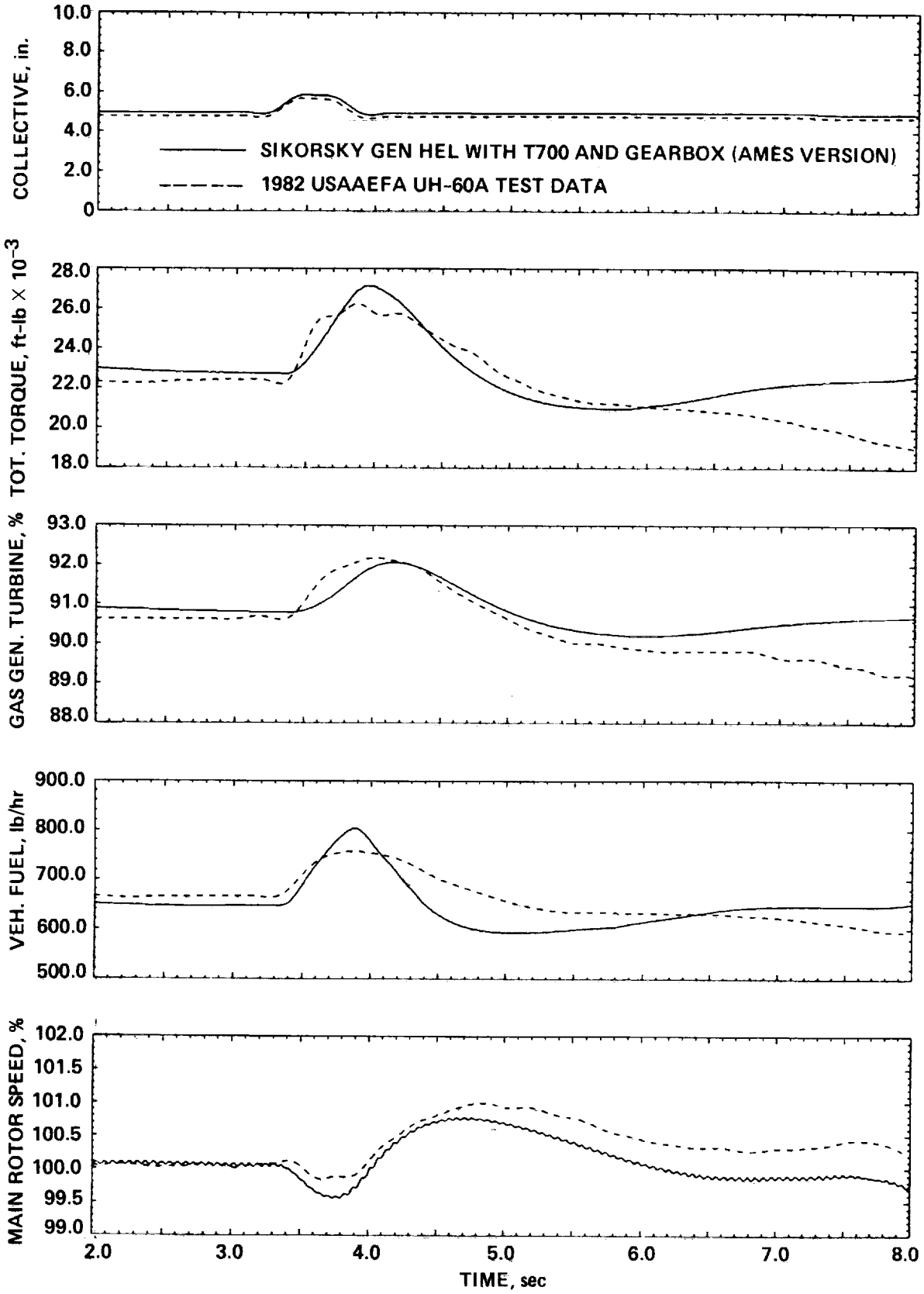

Figure 11: Closed-loop response of engine, fuel control system, and blade-element helicopter simulation to a collective input at high forward speed.

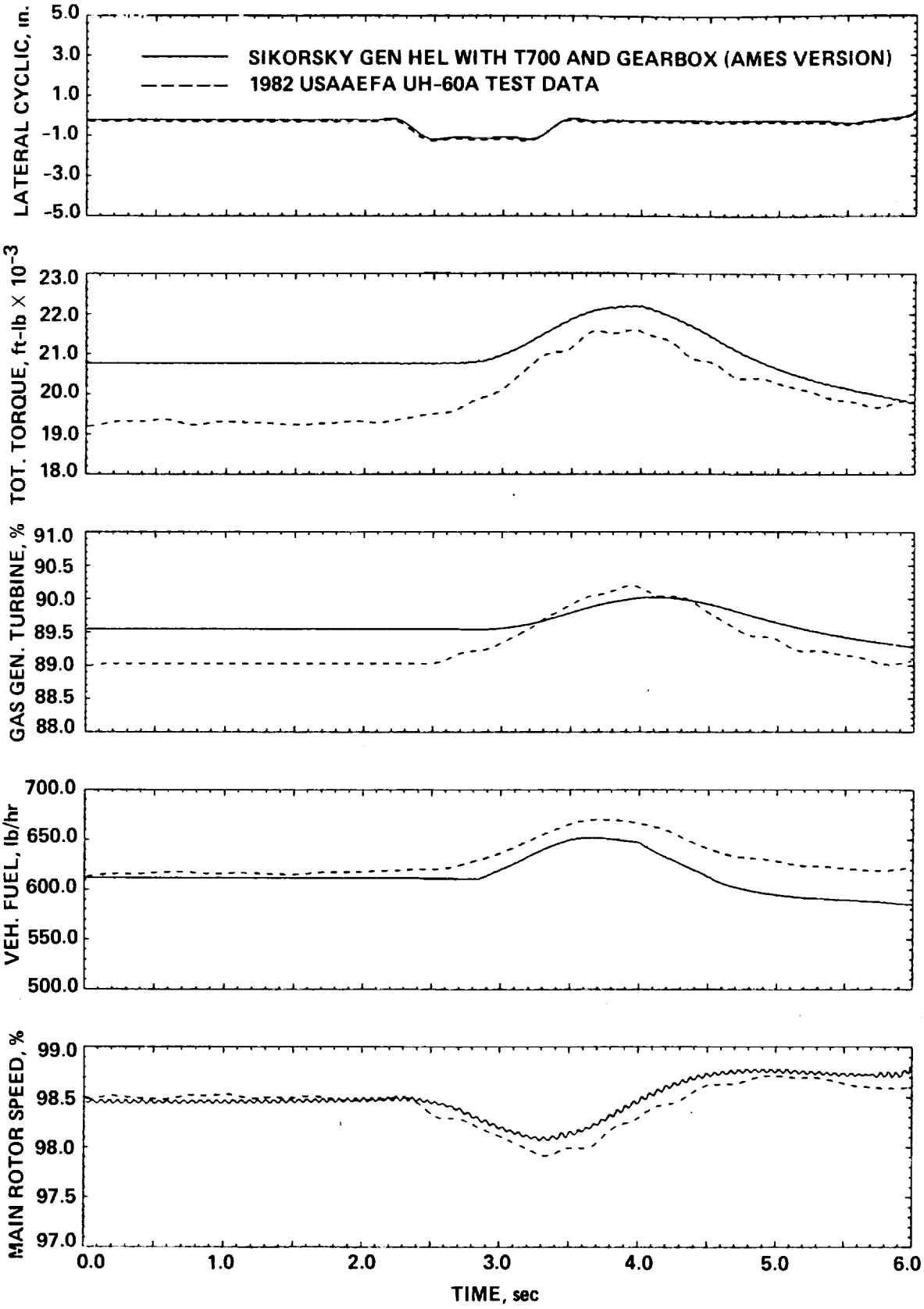

Figure 12: Closed-loop response of engine, fuel control system, and blade-element helicopter simulation to a lateral cyclic input at high forward speed.

speed, and fuel flow time histories suggest that the input causes an increase in torque required by the main rotor in test which is absent in the vehicle simulation. Rotor speed is shown to agree to within 0.2 percent over the duration of the run.

An example of high-power operation can be seen in figure 13, which is a 1-inch-down collective input at hover. In this case, the collective trims do not match well, a result of the simplified vehicle simulation of rotor downwash impingement on the fuselage and stabilator when in hover (ref. 13). Because the simulation requires less power, its torque, fuel flow, and gas generator trim values are lower than their test data counterparts. Trends in the data are reproduced well, however. As in all cases, the simulation fuel flow appears to be more oscillatory than the test data. This is attributed to the location of the sensor used in the test vehicle; it was mounted upstream of both engines and therefore did not correctly represent the fuel flow transients. As in figure 11, there is evidence of greater load demand compensation in the test, as shown by a slight droop in rotor speed during the input and also in a more-quickly-responding gas generator speed.

Another high power case is shown without the influences of the load demand compensation in figure 14, which illustrates the propulsion system response to a pedal input. As in all hover cases, the engine operates at a slightly lower power output because of the incorrect collective-trim position. As shown by the figure, the pedal trim is correct. Rotor speed changes in the test data appear to be be greater, despite greater gas-generator speed changes. Changes in power required by the aircraft are therefore probably greater. After 7.5 seconds, the test vehicle and the simulation had diverged in pitch, resulting in a poor rotor speed match after this point.

An example of response to a large transient input is shown in figure 15. The test data for this case were generated by Sikorsky. Control inputs were significant on all four axes, although the primary input was a lowering of collective from the trim position at 87 knots to the full-down position in one second. This results in nearly zero-G flight immediately after the input. Because the vehicle stabilator was in an off-nominal position, large rotor-hub moments cause large-amplitude first-harmonic oscillations in required torque. The frequency shown by the simulation time history is correct; it is equal to the number of blades times the rotor rotational frequency. The frequency shown by the test data is not correct. It is an aliased frequency caused by a large test-data time step. Rotor speed trends are shown to be in good agreement. The evidence of increased load-demand compensation in the test is again shown by a lack of initial rotor overspeed in the test data.

Dynamic response of the propulsion system is at a level of fidelity comparable to that of the blade-element helicopter simulation. Propulsion system damping is slightly greater than that indicated by the test data, and the load demand compensation is greater in the test data. For cases which are not influenced by the load demand compensation, rotor speed variations appear to be slightly larger in the test data, although there is evidence in some instances that changes in torque required by the vehicle are greater than those required by the vehicle simulation. All mechanical actuator and sensor nonlinearities were modeled with lags, transport delays, and hysteresis loops as provided by GE. Better correlation may possibly be attained by modification of these simple models. Greater model sophistication may also be necessary. Additions may include an explicit variable-geometry guide vane model with dynamics and heat-sink model constants which are a function of increasing and decreasing power. A small effective lag may be added with the inclusion of a $T45$ heat-sink model.

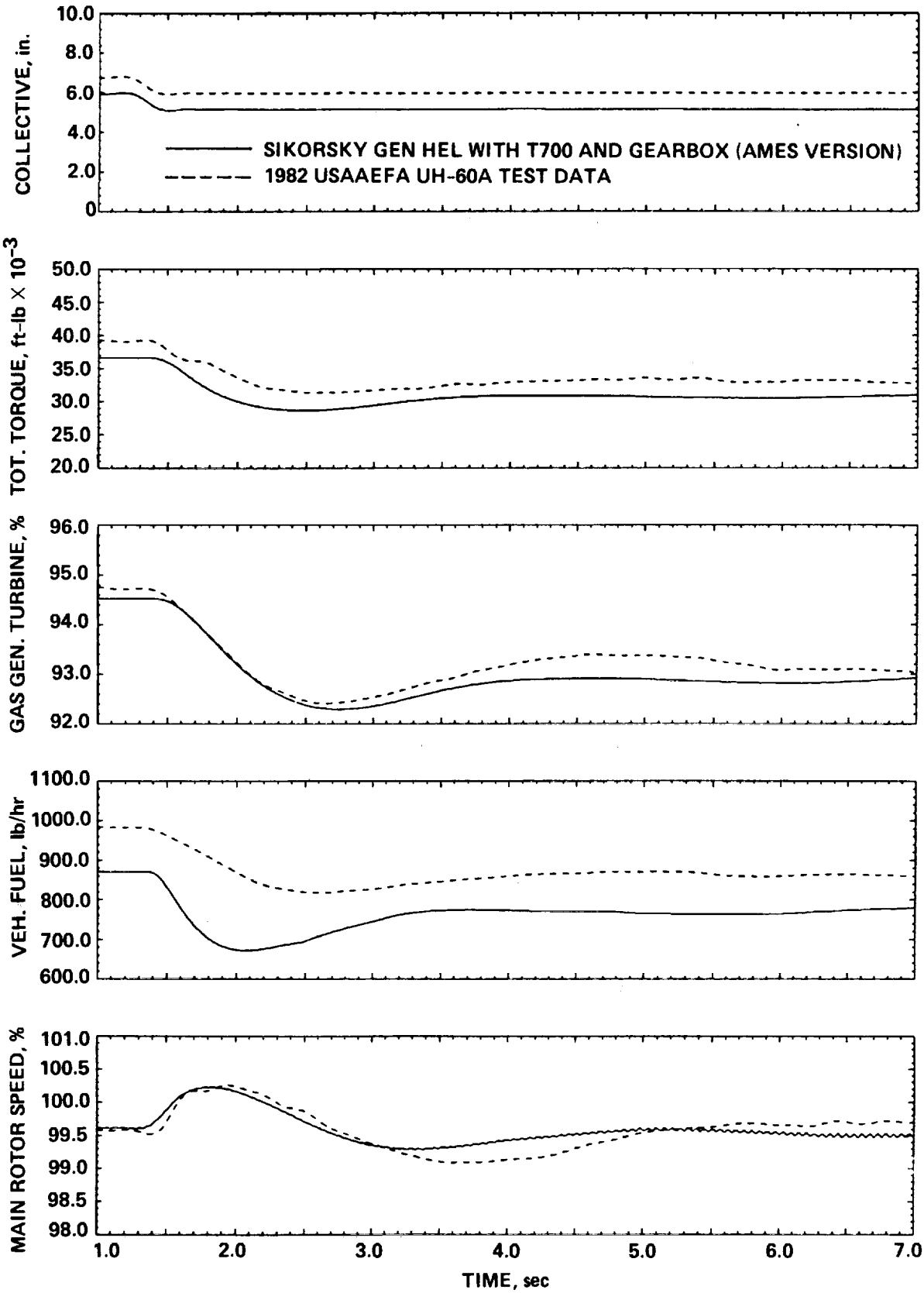

Figure 13: Closed-loop response of engine, fuel control system, and blade-element helicopter simulation to a collective input at hover.

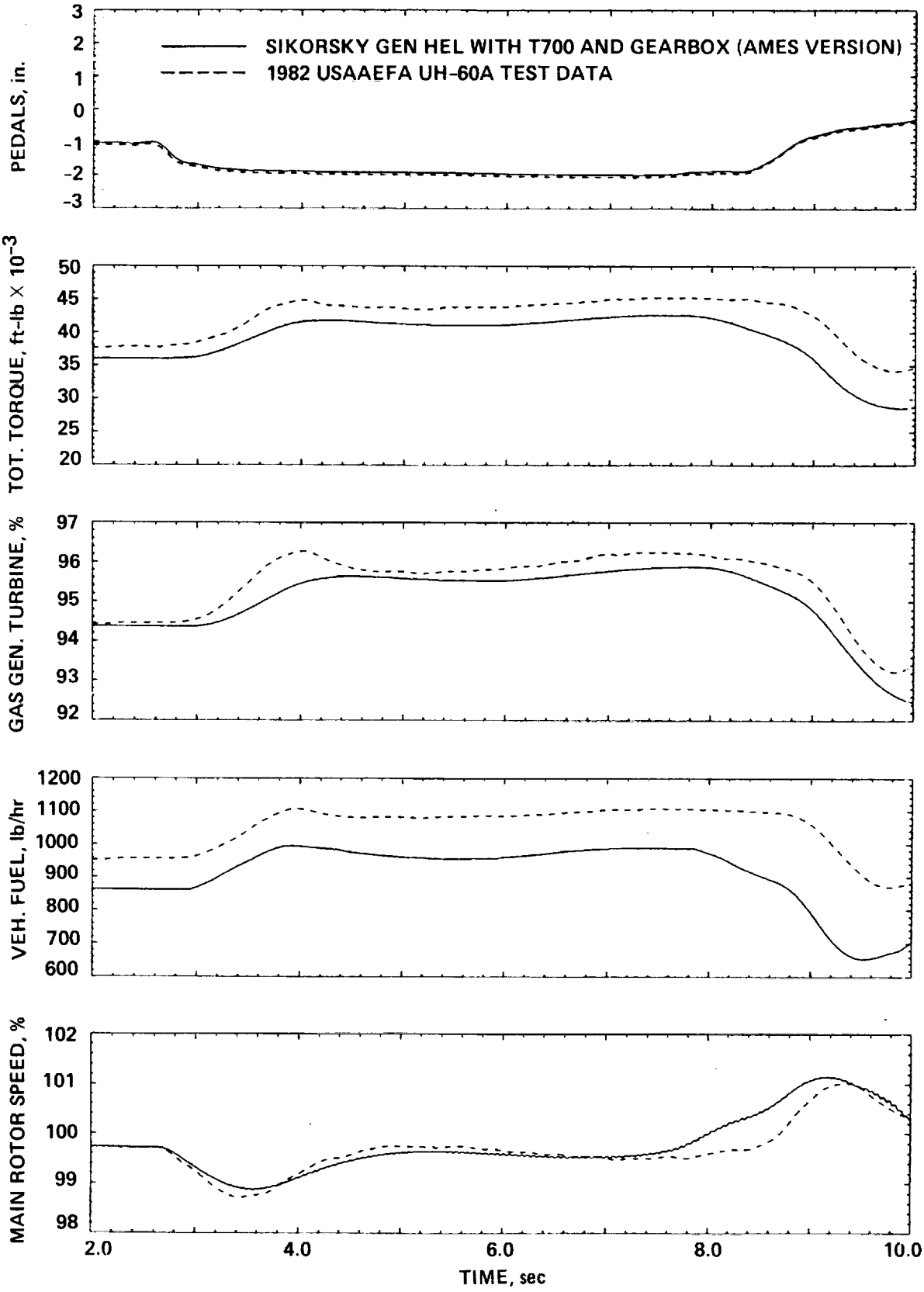

Figure 14: Closed-loop response of engine, fuel control system, and blade-element helicopter simulation to a pedal input at hover.

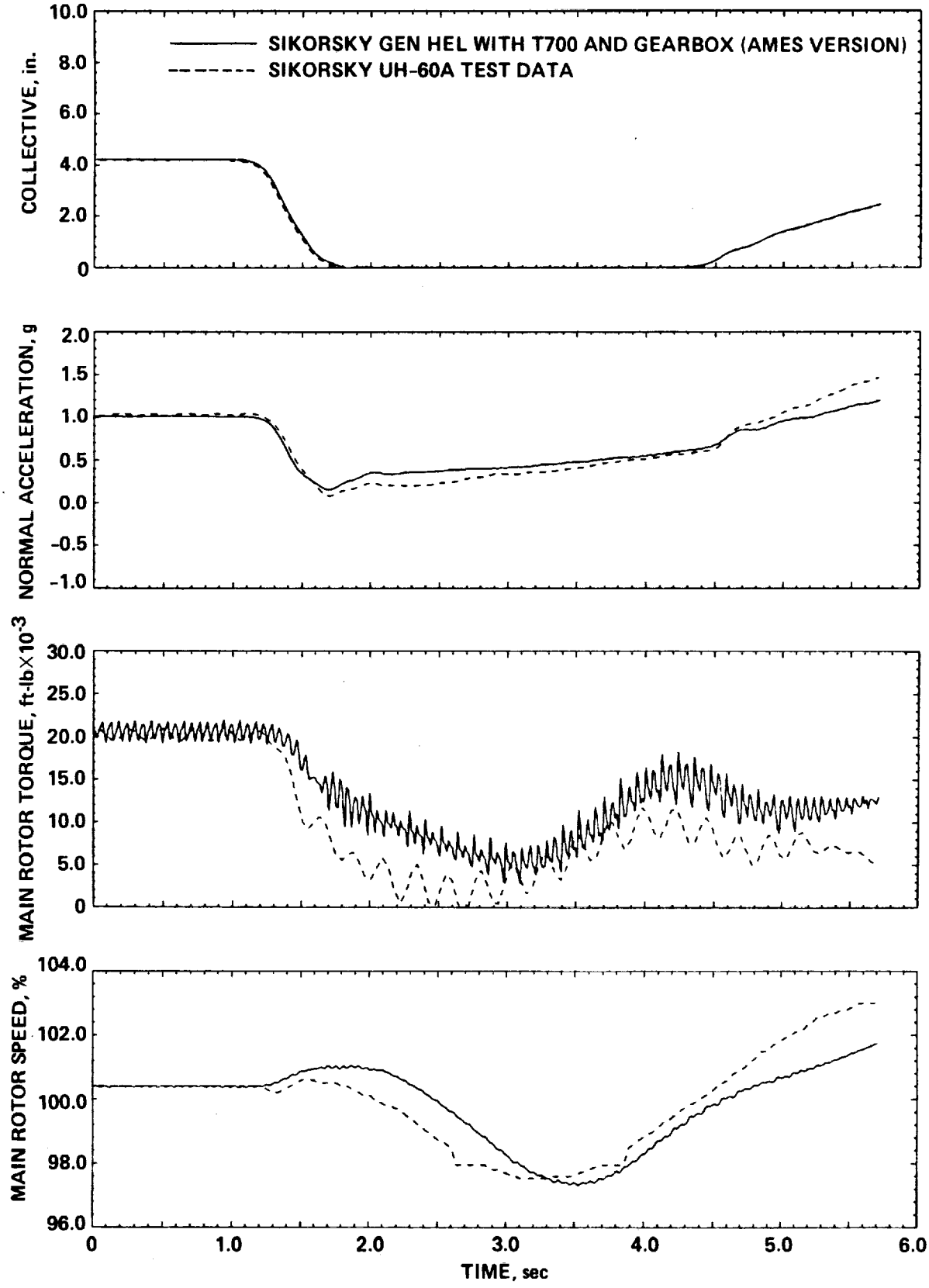

Figure 15: Closed-loop response of engine, fuel control system, and blade-element helicopter simulation to a large collective input.

CONCLUSIONS

As the maneuvering envelope of helicopters is widened for increasingly demanding mission tasks, the associated large-amplitude transients in aircraft power require high-fidelity modeling of the propulsion system. The real-time digital simulation of a small turboshaft engine fills this need in pilot-in-the-loop handling qualities investigations involving such power transients. Applications include real-time studies of the effect of rotor speed variation on handling qualities, investigations of new fuel control and flight control methodologies, and simulations of rotorcraft engine degradation and failure. The model adequately reproduces trim performance over the complete flight-power operating range as well as dynamics associated with changing load conditions. Engine degradation is easily modeled by modifying compressor or turbine flow and energy functions. The digital fuel control system model is separate and may be modified or replaced depending on user requirements.

Validation results suggest that the static and dynamic fidelity of the model is within the limits of the fidelity of current rotorcraft simulations. The modeling of high-speed dynamics which represent changes of mass flow between the internal control volumes was found to be unnecessary. Several refinements were found to be necessary to obtain correct propulsion system response, however. These include estimates of heat transfer to the engine components downstream of the combustor, estimates of losses between the power turbine outlet and the engine exhaust, power-turbine-speed damping, and sensor and actuator dynamics and nonlinearities.

APPENDIX A
T700 ENGINE MODEL CONSTANTS AND FUNCTION TABLES

Model constants and functional relationships specific to the T700-GE-700 engine are given below.

Table A.1

T700 Engine Constants

Constant	Value	Units
HVF	18300.0	Btu/lb_m
J_{GT}	0.0445	$ft \cdot lb_f \cdot sec^2$
J_{PT}	0.062	$ft \cdot lb_f \cdot sec^2$
K_{bl}	0.7826	nondimensional
K_{b3}	0.0025	nondimensional
K_{damp}	0.06854	$ft \cdot lb_f \cdot sec/rad$
K_{dpb}	0.03045	$lb_f^2 \cdot sec^2/lb_m^2 \cdot in^4 \cdot deg\ R$
K_{H2}	0.239	$Btu/lb_m \cdot deg\ R$
K_{H3_1}	0.2496	$Btu/lb_m \cdot deg\ R$
K_{H3_2}	-8.4	Btu/lb_m
K_{H41_1}	0.3010	$Btu/lb_m \cdot deg\ R$
K_{H41_2}	-86.905	Btu/lb_m
K_{H45}	0.9623	nondimensional
K_{Ps3}	0.956	nondimensional
K_{QC_1}	0.71	nondimensional
K_{QC_2}	0.29	nondimensional
K_{T41_1}	3.322	$lb_m \cdot deg\ R/Btu$
K_{T41_2}	288.7	$deg\ R$
K_{T45_1}	3.519	$lb_m \cdot deg\ R/Btu$
K_{T45_2}	179.1	$deg\ R$
K_{T49_1}	3.516	$lb_m \cdot deg\ R/Btu$
K_{T49_2}	172.3	$deg\ R$
K_{TH41_1}	0.0018326	$1/deg\ R$
K_{TH41_2}	0.0856	nondimensional
K_{TH45_1}	0.0018326	$1/deg\ R$
K_{TH45_2}	0.0856	nondimensional
K_{V3}	0.97	$lb_f/in^2 \cdot lb_m \cdot deg\ R$
K_{V41}	6.17	$lb_f/in^2 \cdot lb_m \cdot deg\ R$
K_{V45}	13.63	$lb_f/in^2 \cdot lb_m \cdot deg\ R$
K_{WGT}	0.0876	$lb_m \cdot in^2/lb_f \cdot sec$
NG_{des}	44700.0	rpm
NP_{des}	20900.0	rpm
TC_{T41}	0.29	$lb_m^{\frac{4}{5}} \cdot sec^{\frac{9}{5}}/deg\ R^{\frac{1}{2}}$

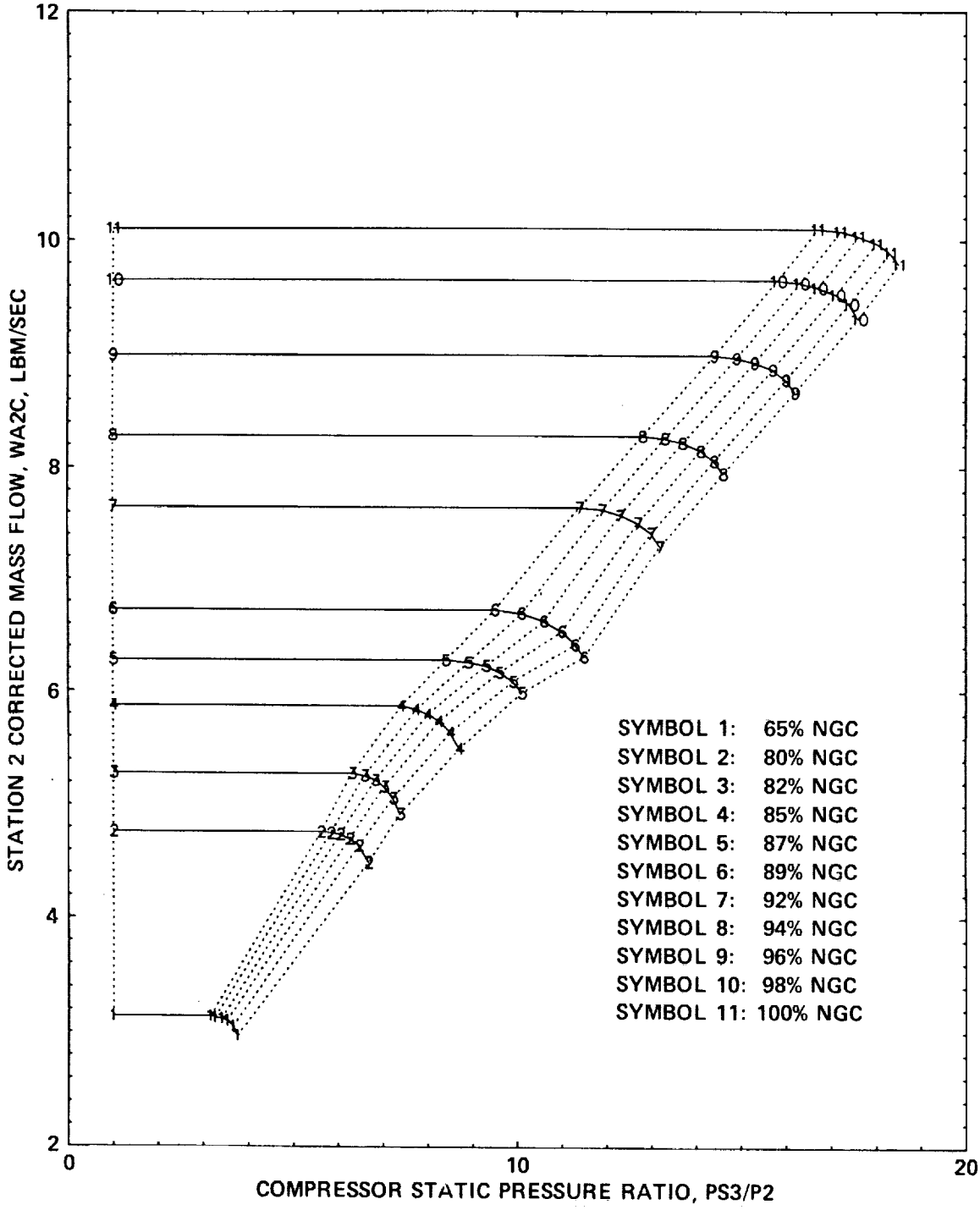

Figure A1.- T700 real-time model function f_1—compressor mass flow.

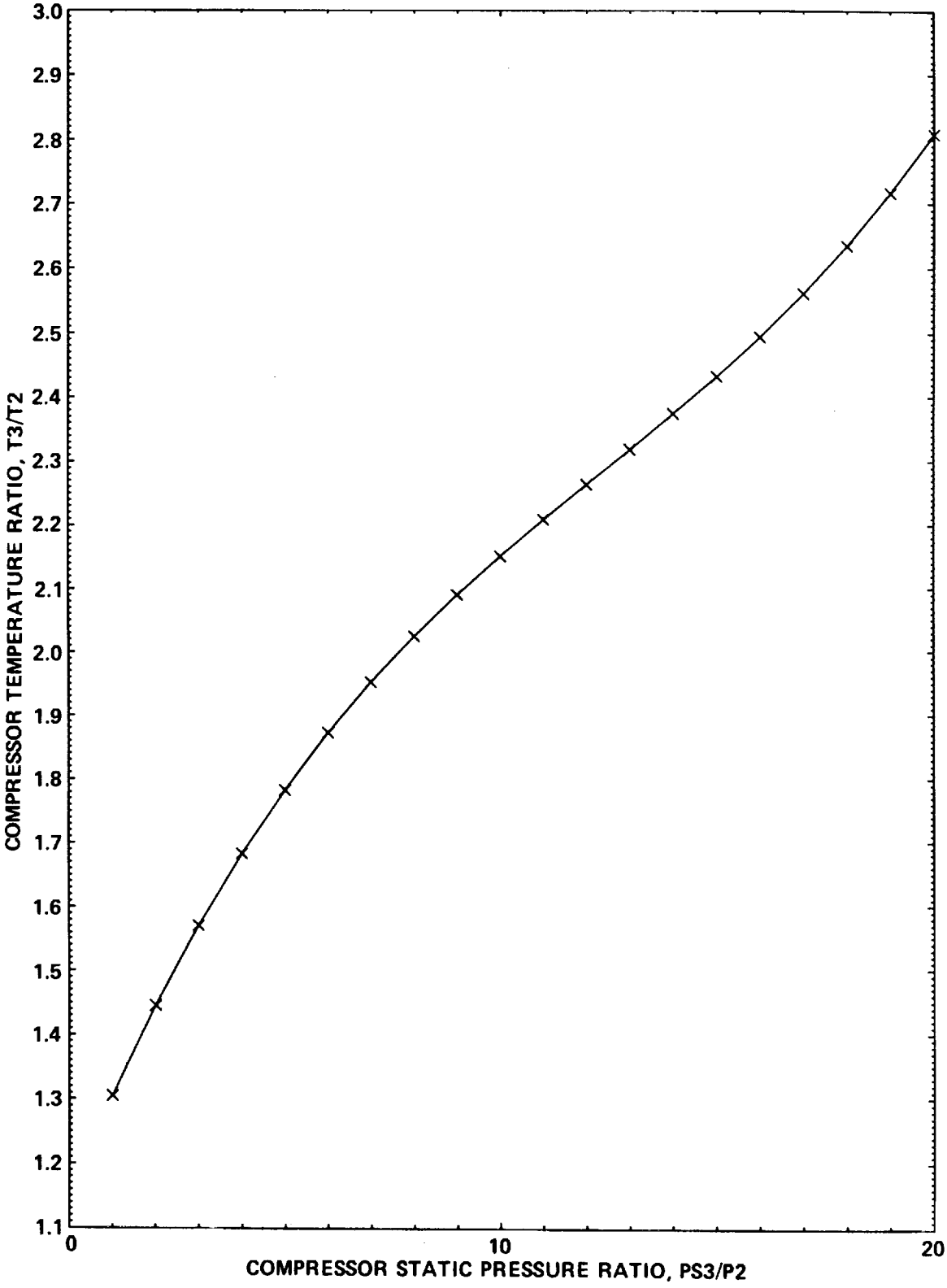

Figure A2.- T700 real-time model function f_2—compressor temperature.

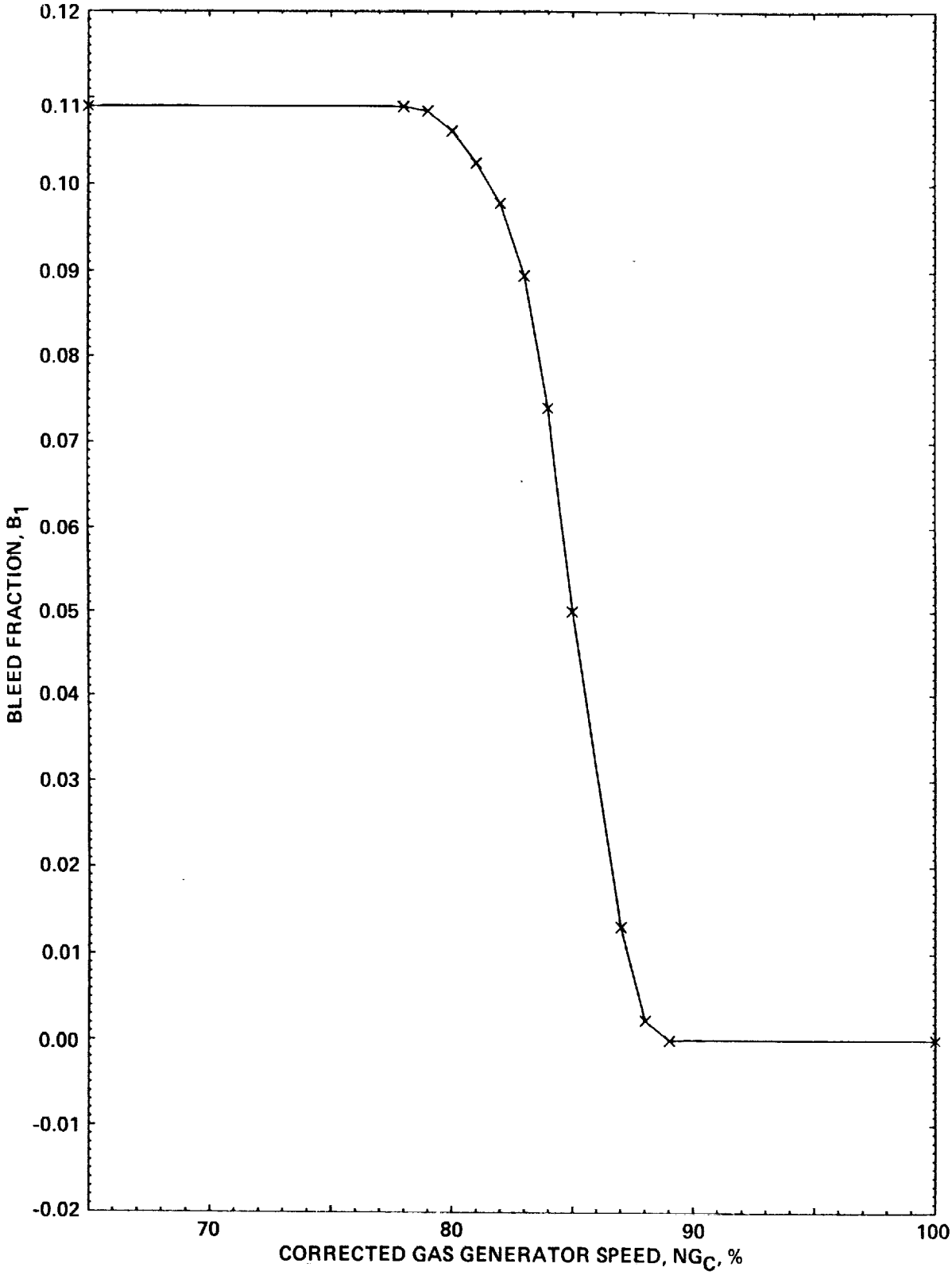

Figure A3.- T700 real-time model function f_3—seal-pressurization bleed fraction.

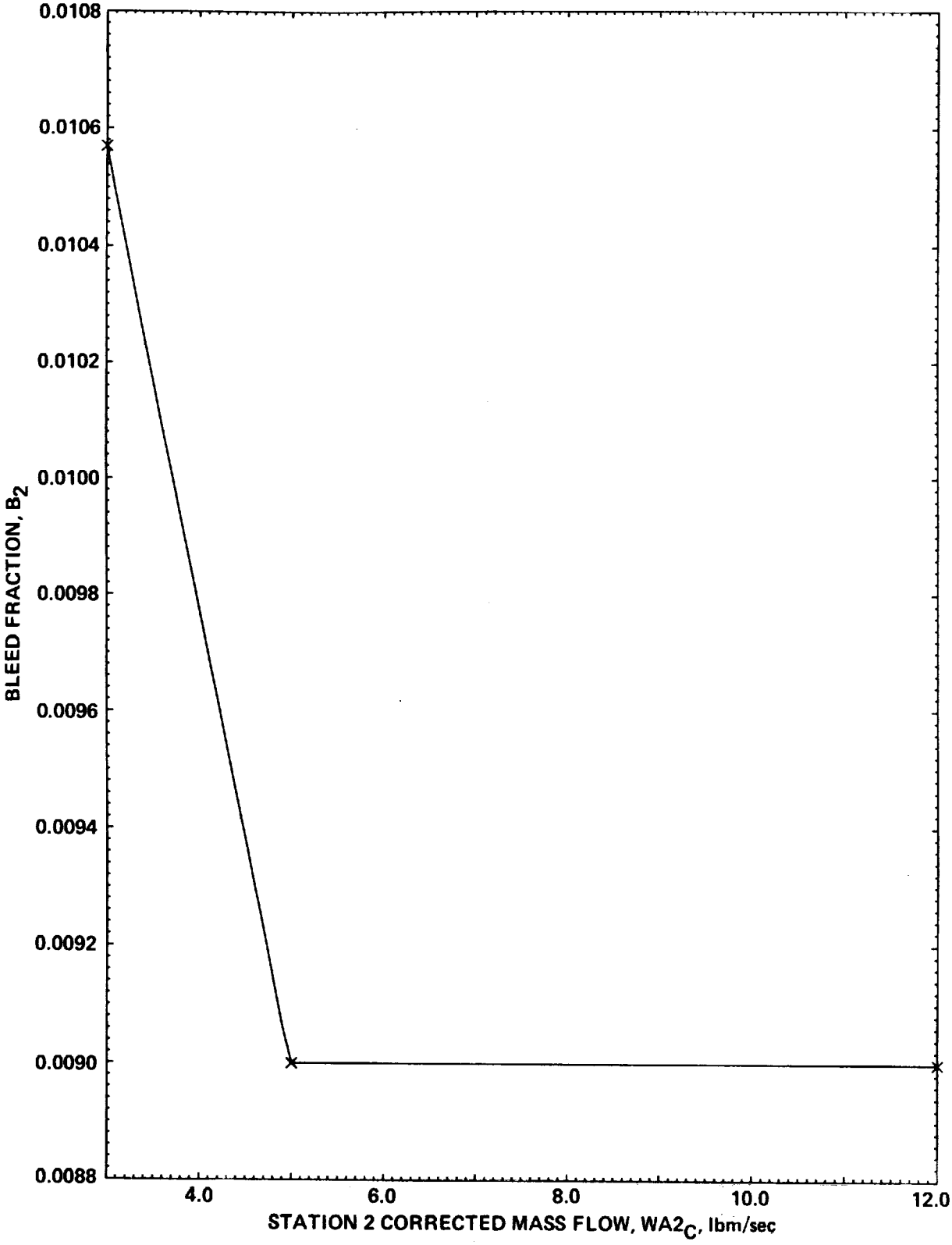

Figure A4.- T700 real-time model function f_4—power-turbine-balance bleed fraction.

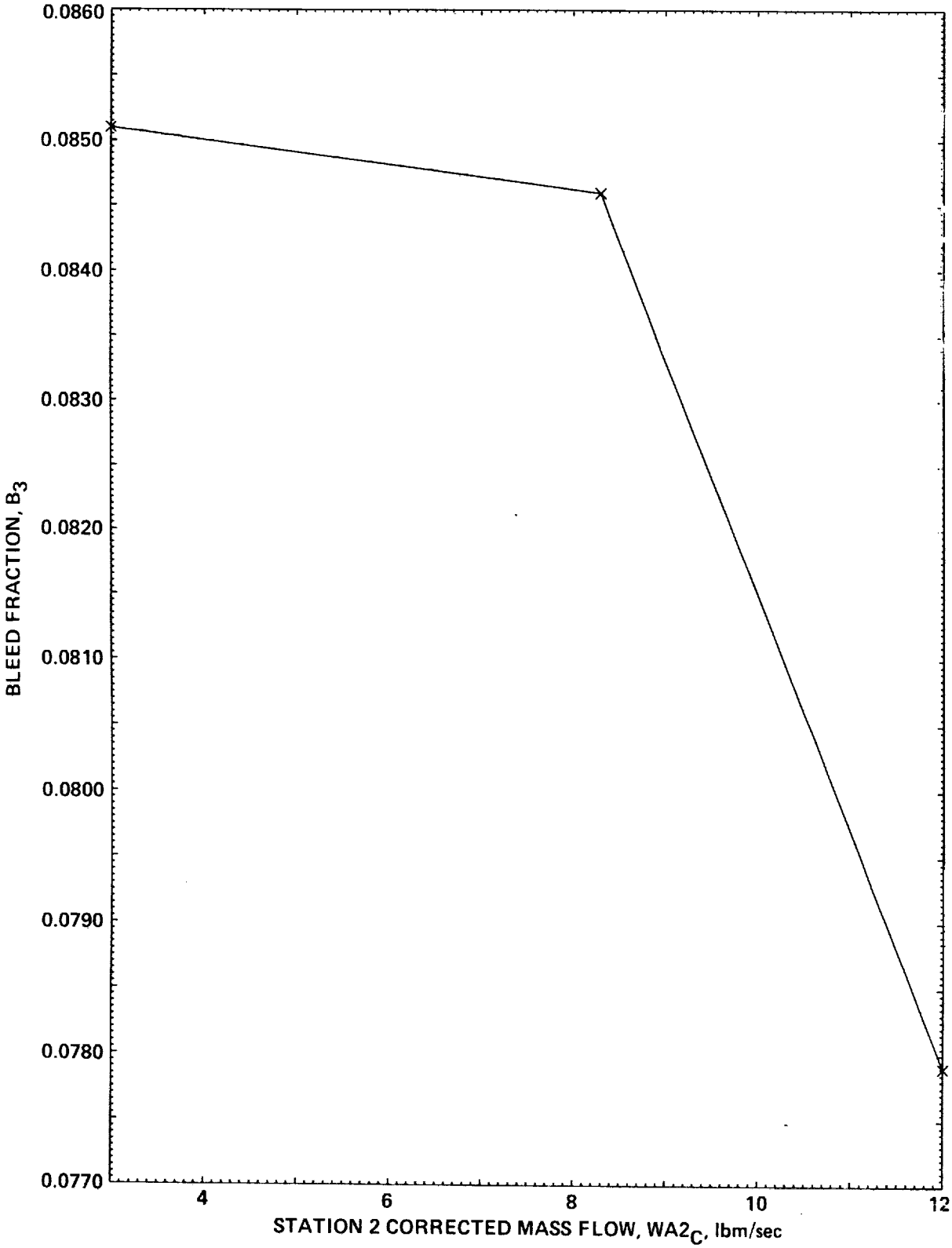

Figure A5.- T700 real-time model function f_5—impeller tip leakage and turbine cooling-bleed fraction.

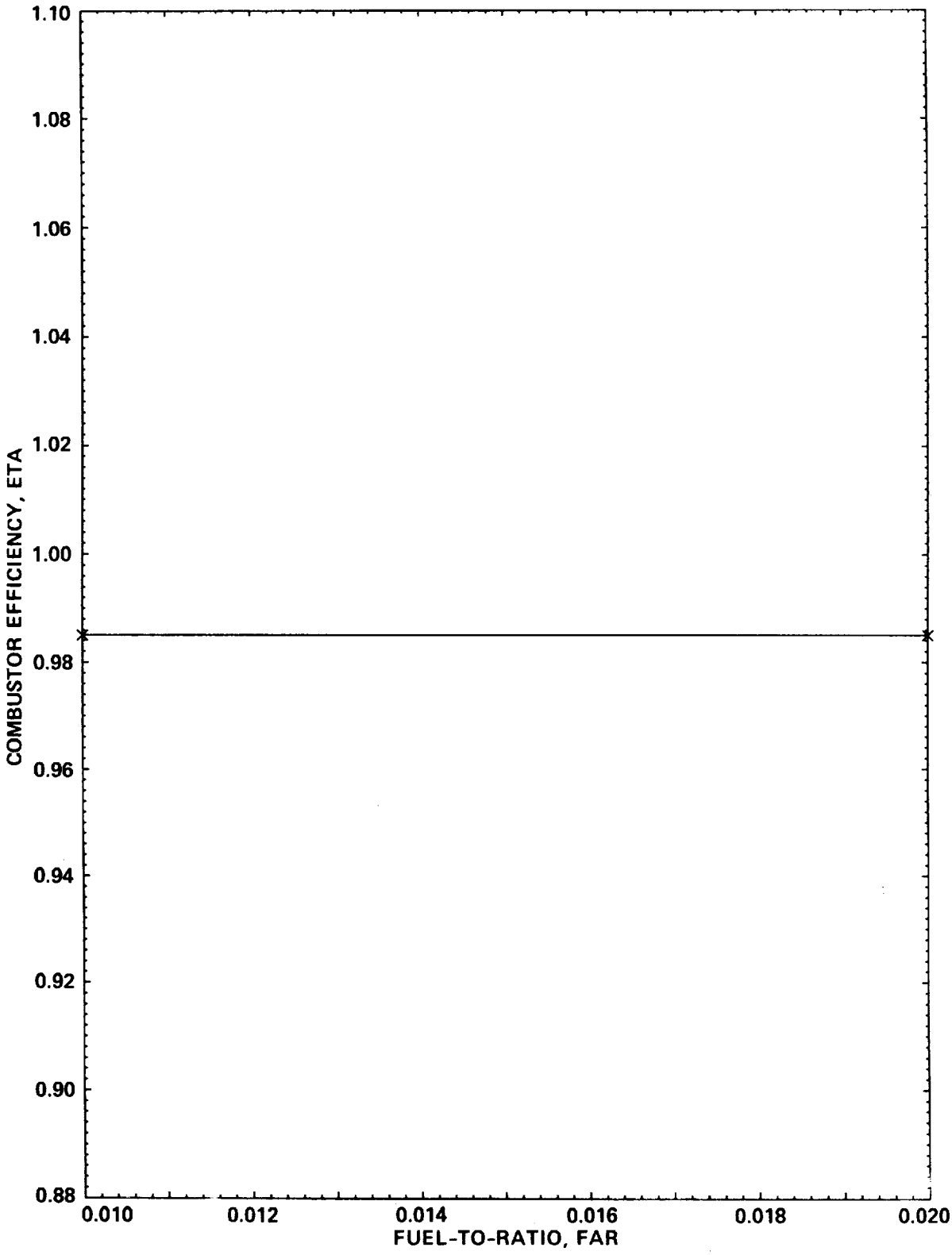

Figure A6.- T700 real-time model function f_6—combustor efficiency.

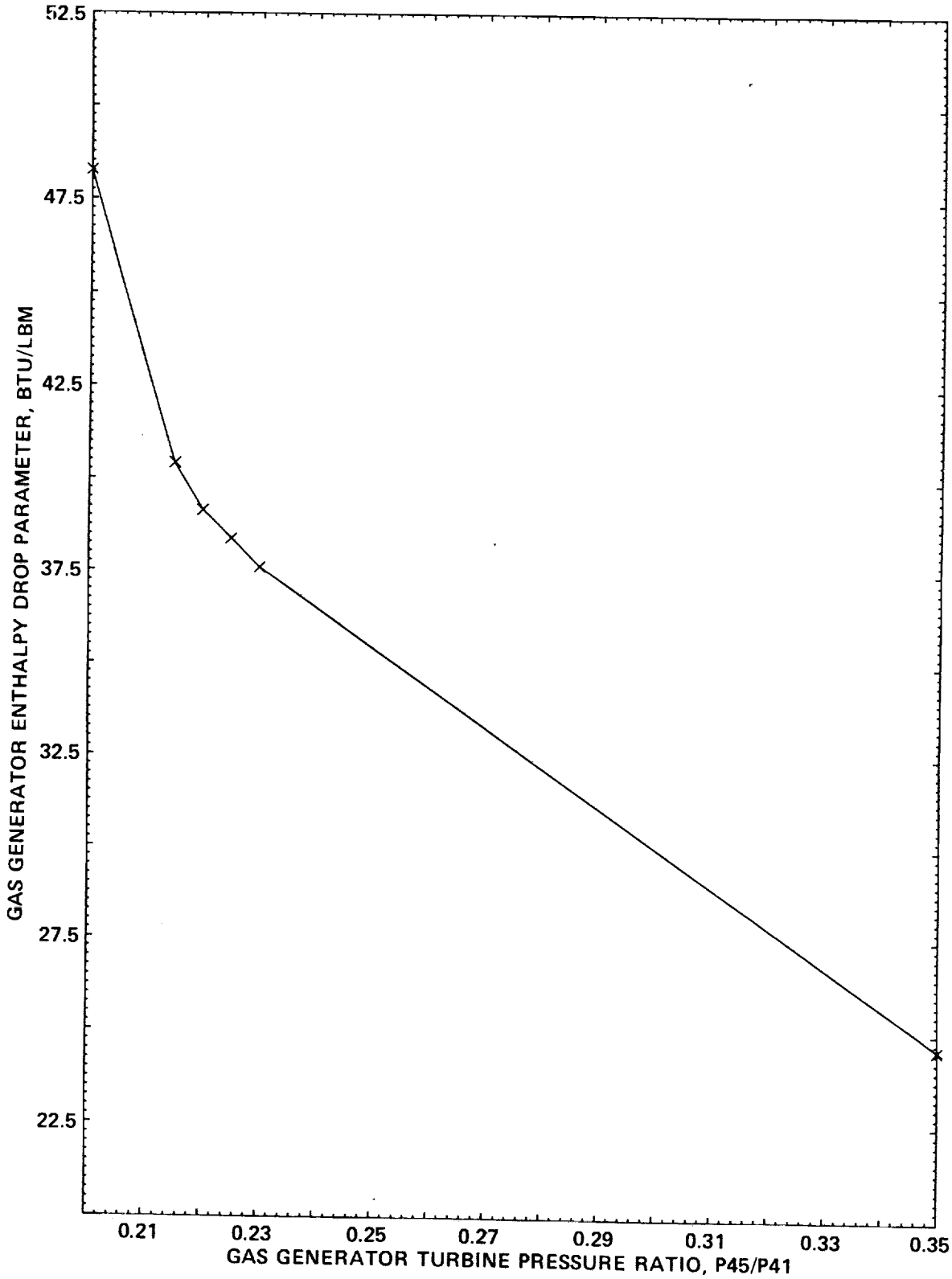

Figure A7.- T700 real-time model function f_7—gas-generator turbine energy.

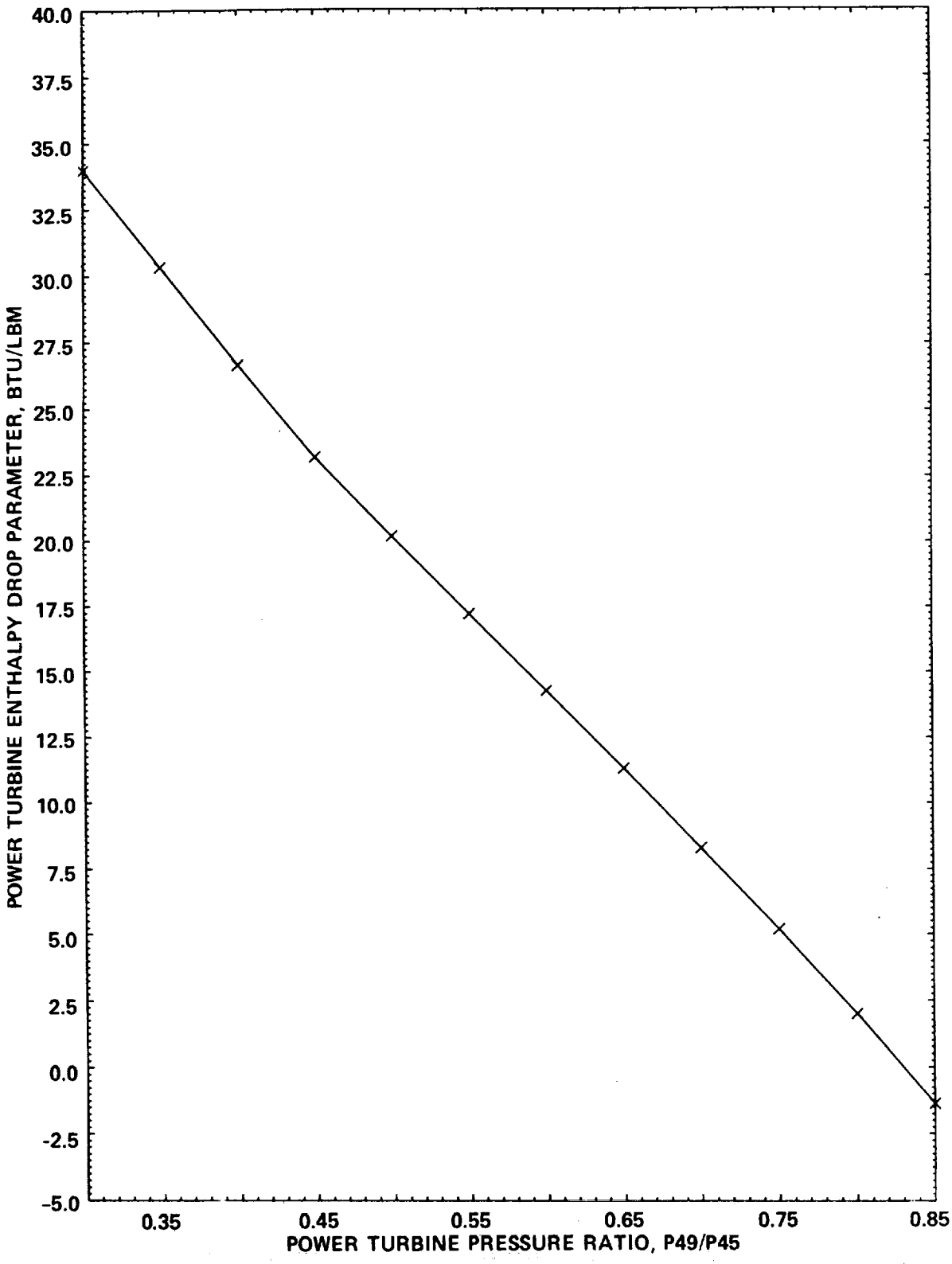

Figure A8.- T700 real-time model function f_8—power turbine energy.

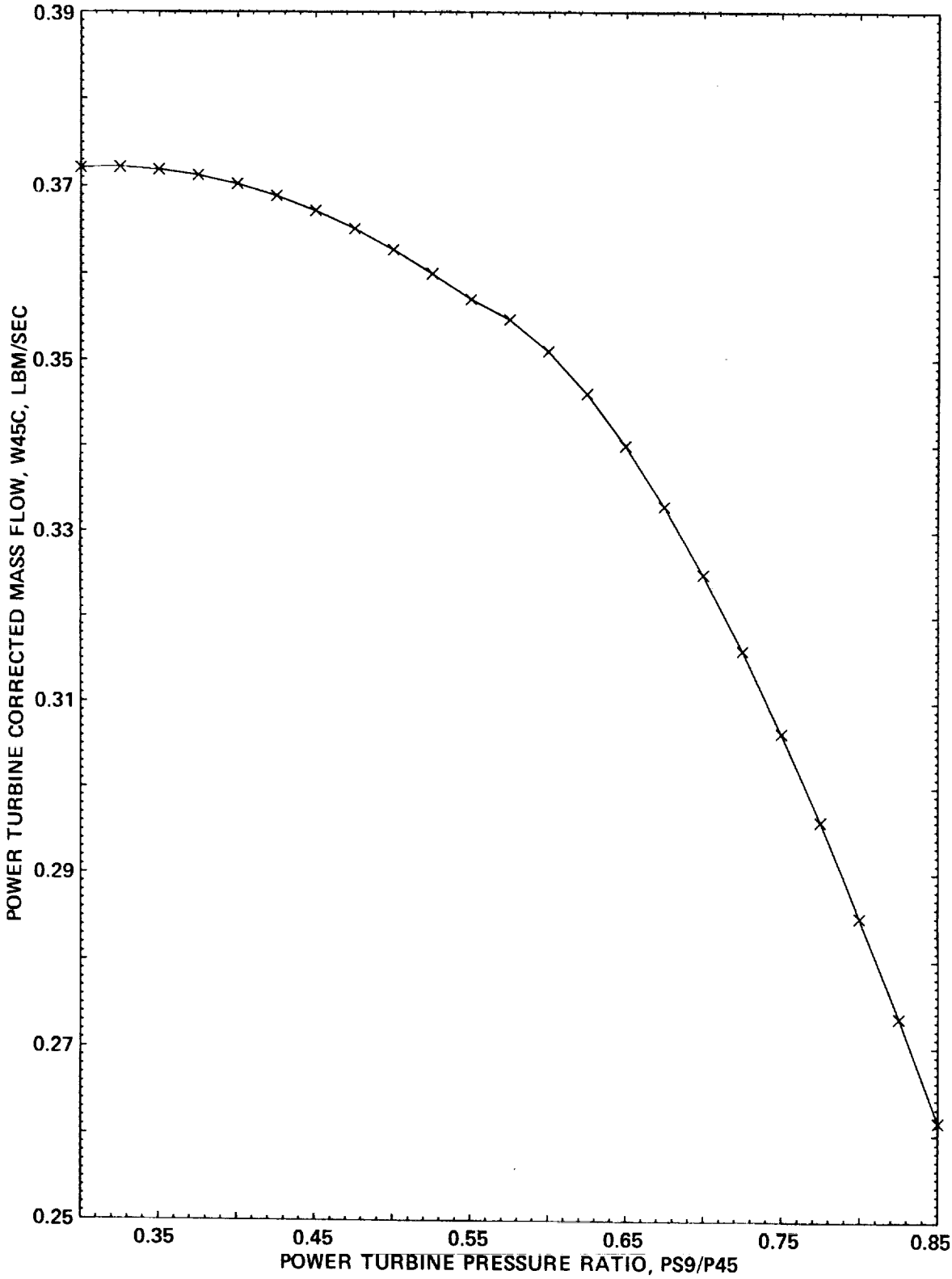

Figure A9.- T700 real-time model function f_9—power turbine mass flow.

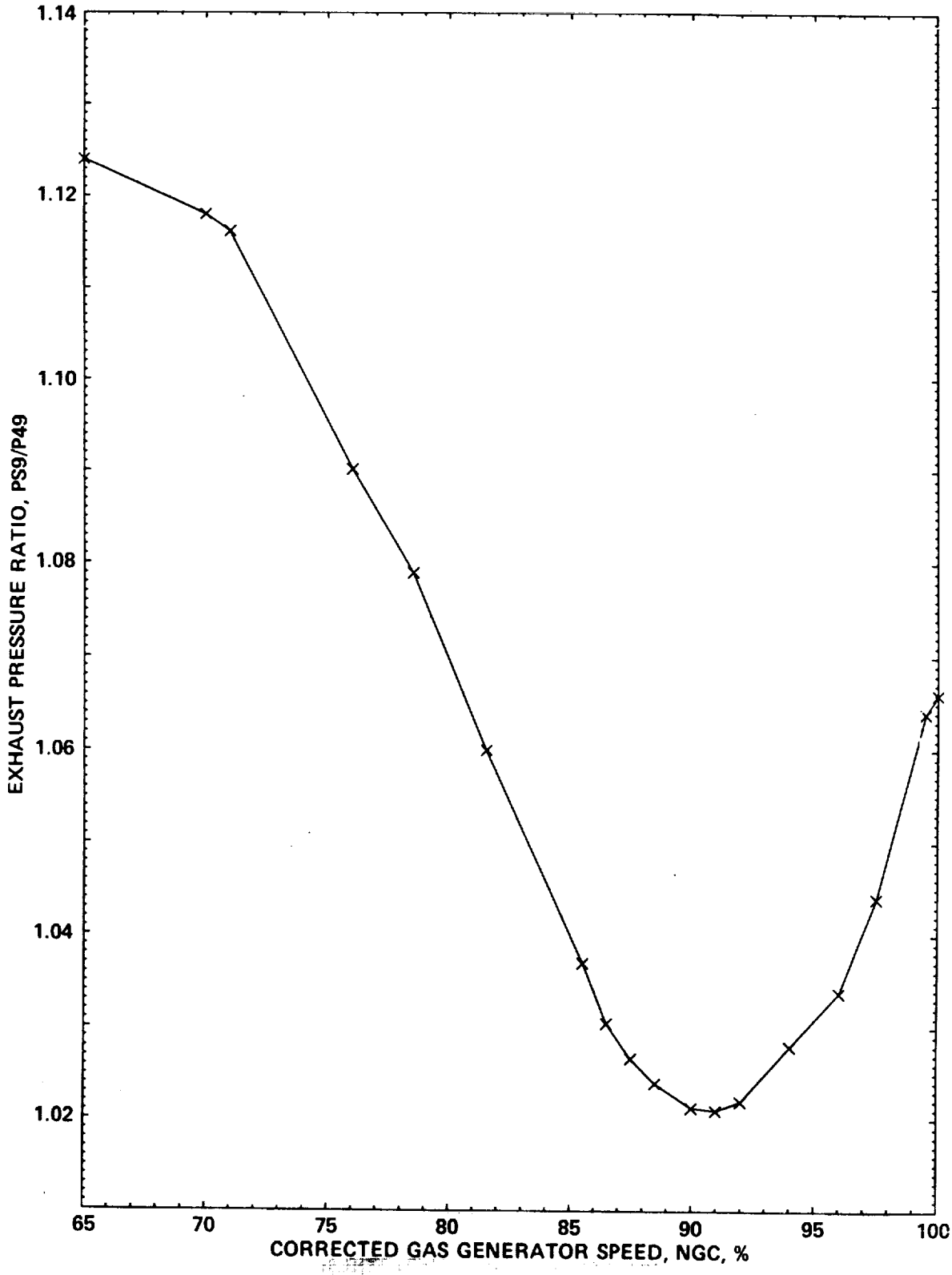

Figure A10.- T700 real-time model function f_{10}—exhaust pressure loss.

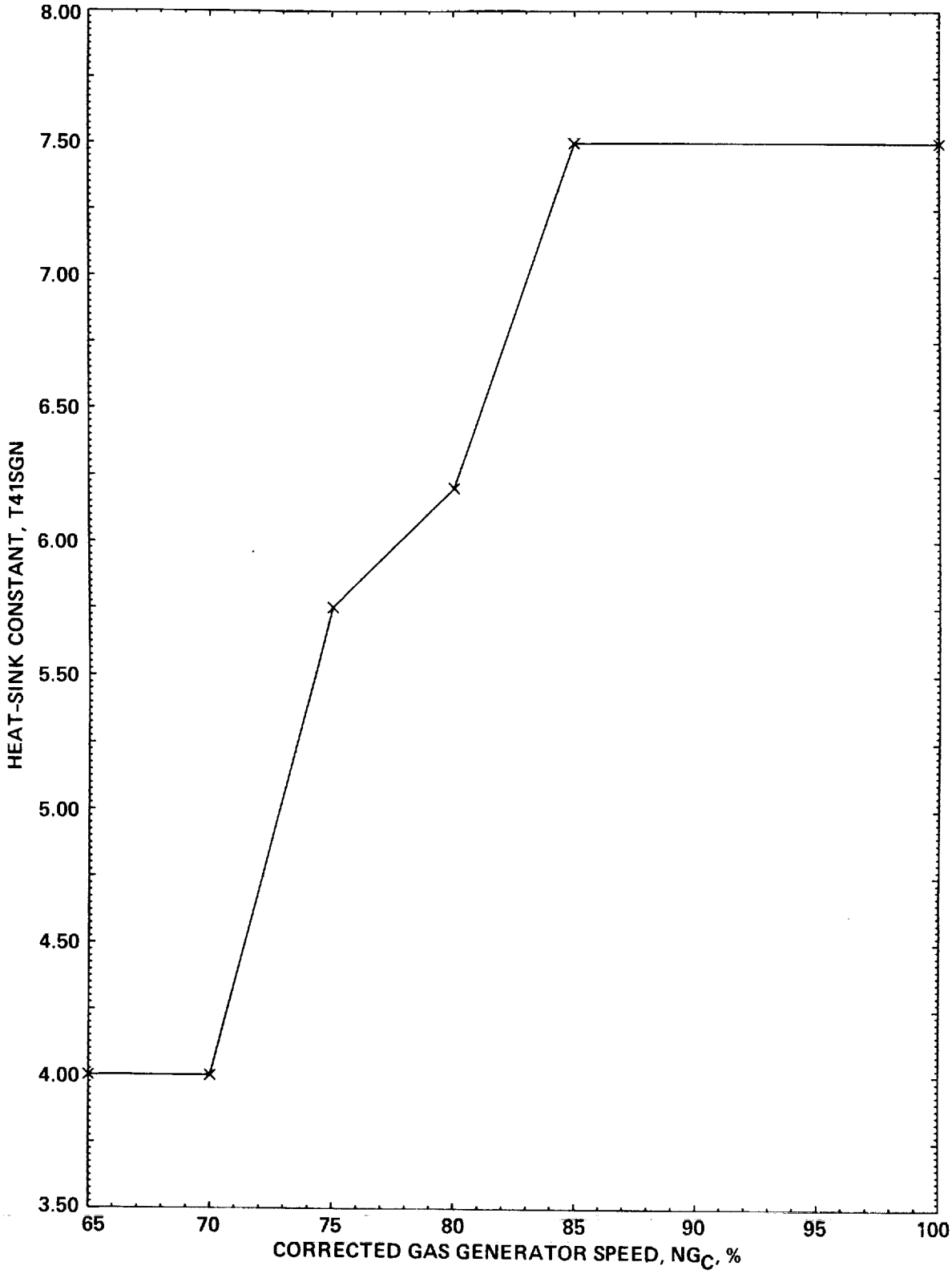

Figure A11.- T700 real-time model function f_{hs}—station 4.1 heat-sink constant.

APPENDIX B
LINEAR MODELS

Small-perturbation linear models for three trim conditions are given below. The two- and three-degree-of-freedom models approximate the dynamics between the control volumes to be instantaneous; the five- and six-degree-of-freedom models contain complete dynamics. The heat-sink model is contained in the three- and six-degree-of-freedom models.

TABLE B.1

SMALL-PERTURBATION MODEL TRIM CONDITIONS

Trim Condition	1[a]	2[b]	3[c]
Aircraft weight, lb_m	16825.	16825.	16825.
CG station, in	355.0	355.0	355.0
CG waterline, in	248.2	248.2	248.2
CG buttline, in	0.0	0.0	0.0
Equivalent airspeed, kts	0.0	80.0	80.0
Flightpath angle, deg	0.0	0.0	-7.08
Altitude, ft	0.0	0.0	0.0
Required torque (ref. hub), $ft \cdot lb_f$	32865.	20747.	10792.
Engine torque (ref. shaft), $ft \cdot lb_f$	229.0	138.9	76.06
Horsepower per engine	911.1	552.6	302.6
Power turbine speed, rpm	20895.	20895.	20895.
Gas Generator Speed, $rpmM$	41638.	39768.	38072.
Fuel flow per engine, lb_m/hr	476.3	349.3	267.7
P2, $PSIA$	14.696	14.696	14.696
T2, $deg\ R$	518.67	518.67	518.67
P_s3, $PSIA$	176.34	142.13	114.27
P41, $PSIA$	174.28	140.26	112.77
T41, $deg\ R$	2292.	2102.	1982.
P45, $PSIA$	37.42	30.66	25.54
T45, $deg\ R$	1632.	1501.	1424.

[a]Trim condition 1: hover
[b]Trim condition 2: level flight at 80 knots
[c]Trim condition 3: 1000 ft/min descending flight at 80 knots

$$A = \begin{bmatrix} -0.2693E+1 & 0.0000E+0 \\ 0.3865E+0 & -0.5650E+0 \end{bmatrix}$$

$$\bar{b} = \begin{bmatrix} 0.1296E+6 \\ 0.2105E+5 \end{bmatrix}$$

Figure B1. - 2 degree-of-freedom model for trim condition 1.

$$A = \begin{bmatrix} -0.4474E+1 & 0.0000E+0 & -0.6928E+3 & 0.1462E+4 & -0.2942E+4 \\ -0.2444E-1 & -0.5650E+0 & -0.4128E+2 & 0.3302E+2 & 0.2321E+3 \\ 0.7524E+0 & 0.0000E+0 & -0.4230E+3 & 0.4071E+3 & 0.0000E+0 \\ 0.0000E+0 & 0.0000E+0 & 0.4115E+4 & -0.4526E+4 & 0.0000E+0 \\ 0.1063E+1 & 0.0000E+0 & -0.2695E+3 & 0.8101E+3 & -0.3063E+4 \end{bmatrix}$$

$$\bar{b} = \begin{bmatrix} 0.8238E+5 \\ 0.6174E+4 \\ 0.0000E+0 \\ 0.1891E+6 \\ 0.4021E+5 \end{bmatrix}$$

Figure B2. - 5 degree-of-freedom model for trim condition 1.

$$A = \begin{bmatrix} -0.2233E+1 & 0.0000E+0 \\ 0.3128E+0 & -0.4461E+0 \end{bmatrix}$$

$$\overline{b} = \begin{bmatrix} 0.1494E+6 \\ 0.1663E+5 \end{bmatrix}$$

Figure B3. - 2 degree-of-freedom model for trim condition 2.

$$A = \begin{bmatrix} -0.3659E+1 & 0.0000E+0 & -0.6173E+3 & 0.1107E+4 & -0.1548E+4 \\ 0.1283E-1 & -0.4461E+0 & -0.2898E+2 & 0.2551E+2 & 0.1825E+3 \\ 0.6340E+0 & 0.0000E+0 & -0.4090E+3 & 0.3899E+3 & 0.0000E+0 \\ 0.0000E+0 & 0.0000E+0 & 0.3898E+4 & -0.4287E+4 & 0.0000E+0 \\ 0.8461E+0 & 0.0000E+0 & -0.2551E+3 & 0.9497E+3 & -0.4038E+4 \end{bmatrix}$$

$$\overline{b} = \begin{bmatrix} 0.8411E+5 \\ 0.4888E+4 \\ 0.0000E+0 \\ 0.1882E+6 \\ 0.4221E+5 \end{bmatrix}$$

Figure B4. - 5 degree-of-freedom model for trim condition 2.

$$A = \begin{bmatrix} -0.1816E+1 & 0.0000E+0 \\ 0.3615E+0 & -0.3567E+0 \end{bmatrix}$$

$$\bar{b} = \begin{bmatrix} 0.1531E+6 \\ 0.1435E+5 \end{bmatrix}$$

Figure B5. - 2 degree-of-freedom model for trim condition 3.

$$A = \begin{bmatrix} -0.3696E+1 & 0.0000E+0 & -0.5959E+3 & 0.9809E+3 & -0.1034E+4 \\ 0.3555E-1 & -0.3567E+0 & -0.1940E+2 & 0.1774E+2 & 0.1690E+3 \\ 0.7624E+0 & 0.0000E+0 & -0.3989E+3 & 0.3783E+3 & 0.0000E+0 \\ 0.0000E+0 & 0.0000E+0 & 0.3803E+4 & -0.4179E+4 & 0.0000E+0 \\ 0.6997E+0 & 0.0000E+0 & -0.2619E+3 & 0.1000E+4 & -0.4431E+4 \end{bmatrix}$$

$$\bar{b} = \begin{bmatrix} 0.8525E+5 \\ 0.3436E+4 \\ 0.0000E+0 \\ 0.1876E+6 \\ 0.4496E+5 \end{bmatrix}$$

Figure B6. - 5 degree-of-freedom model for trim condition 3.

$$A = \begin{bmatrix} -0.1618E+1 & 0.0000E+0 & 0.1472E+2 \\ 0.5569E+0 & -0.5650E+0 & 0.2432E+1 \\ 0.5148E-1 & 0.0000E+0 & -0.9891E+0 \end{bmatrix}$$

$$\overline{b} = \begin{bmatrix} 0.8500E+5 \\ 0.1362E+5 \\ -0.3011E+4 \end{bmatrix}$$

$$C = \begin{bmatrix} \mathbf{I} \end{bmatrix}$$

$$\overline{d} = \begin{bmatrix} 0.0000E+0 \\ 0.0000E+0 \\ 0.5294E+4 \end{bmatrix}$$

Figure B7. - 3 degree-of-freedom model for trim condition 1.

$A =$

$$\begin{bmatrix} -0.4474E+1 & 0.0000E+0 & -0.1419E+3 & 0.9129E+3 & -0.2942E+4 & 0.1049E+2 \\ -0.2444E-1 & -0.5650E+0 & 0.0000E+0 & -0.7748E+1 & 0.2321E+3 & 0.7867E+0 \\ 0.7524E+0 & 0.0000E+0 & -0.4230E+3 & 0.4071E+3 & 0.0000E+0 & 0.0000E+0 \\ 0.0000E+0 & 0.0000E+0 & 0.5252E+4 & -0.5653E+4 & 0.0000E+0 & 0.2229E+2 \\ 0.1063E+1 & 0.0000E+0 & 0.0000E+0 & 0.5445E+3 & -0.3063E+4 & 0.5123E+1 \\ -0.2659E+2 & 0.0000E+0 & 0.1984E+6 & -0.2118E+6 & 0.0000E+0 & 0.7785E+3 \end{bmatrix}$$

$$\bar{b} = \begin{bmatrix} 0.5533E+5 \\ 0.4147E+4 \\ 0.0000E+0 \\ 0.1316E+6 \\ 0.2701E+5 \\ 0.4600E+7 \end{bmatrix}$$

$$C = \begin{bmatrix} \mathbf{I} \end{bmatrix}$$

$$\bar{d} = \begin{bmatrix} 0.0000E+0 \\ 0.0000E+0 \\ 0.0000E+0 \\ 0.0000E+0 \\ 0.0000E+0 \\ 0.5271E+4 \end{bmatrix}$$

Figure B8. - 6 degree-of-freedom model for trim condition 1.

$$A = \begin{bmatrix} -0.1305E+1 & 0.0000E+0 & 0.1439E+2 \\ 0.4215E+0 & -0.4461E+0 & 0.1596E+1 \\ 0.3364E-1 & 0.0000E+0 & -0.8622E+0 \end{bmatrix}$$

$$\overline{b} = \begin{bmatrix} 0.9239E+5 \\ 0.1030E+5 \\ -0.2673E+4 \end{bmatrix}$$

$$C = \begin{bmatrix} \mathbf{I} \end{bmatrix}$$

$$\overline{d} = \begin{bmatrix} 0.0000E+0 \\ 0.0000E+0 \\ 0.6076E+4 \end{bmatrix}$$

Figure B9. - 3 degree-of-freedom model for trim condition 2.

$A =$

$$\begin{bmatrix} -0.3659E+1 & 0.0000E+0 & -0.1185E+3 & 0.6127E+3 & -0.1548E+4 & 0.8968E+1 \\ 0.1283E-1 & -0.4461E+0 & 0.0000E+0 & -0.3099E+1 & 0.1825E+3 & 0.5212E+0 \\ 0.6340E+0 & 0.0000E+0 & -0.4090E+3 & 0.3899E+3 & 0.0000E+0 & 0.0000E+0 \\ 0.0000E+0 & 0.0000E+0 & 0.4909E+4 & -0.5287E+4 & 0.0000E+0 & 0.1868E+2 \\ 0.8461E+0 & 0.0000E+0 & -0.4315E+1 & 0.7010E+3 & -0.4038E+4 & 0.4501E+1 \\ -0.2279E+2 & 0.0000E+0 & 0.1889E+6 & -0.2017E+6 & 0.0000E+0 & 0.6630E+3 \end{bmatrix}$$

$$\bar{b} = \begin{bmatrix} 0.5425E+5 \\ 0.3153E+4 \\ 0.0000E+0 \\ 0.1260E+6 \\ 0.2722E+5 \\ 0.4473E+7 \end{bmatrix}$$

$$C = \begin{bmatrix} \mathrm{I} \end{bmatrix}$$

$$\bar{d} = \begin{bmatrix} 0.0000E+0 \\ 0.0000E+0 \\ 0.0000E+0 \\ 0.0000E+0 \\ 0.0000E+0 \\ 0.6048E+4 \end{bmatrix}$$

Figure B10. - 6 degree-of-freedom model for trim condition 2.

$$A = \begin{bmatrix} -0.7428E+0 & 0.0000E+0 & 0.1217E+2 \\ 0.4617E+0 & -0.3567E+0 & 0.1130E+1 \\ 0.1659E-1 & 0.0000E+0 & -0.8819E+0 \end{bmatrix}$$

$$\overline{b} = \begin{bmatrix} 0.9056E+5 \\ 0.8540E+4 \\ -0.3507E+4 \end{bmatrix}$$

$$C = \begin{bmatrix} \mathbf{I} \end{bmatrix}$$

$$\overline{d} = \begin{bmatrix} 0.0000E+0 \\ 0.0000E+0 \\ 0.7076E+4 \end{bmatrix}$$

Figure B11. - 3 degree-of-freedom model for trim condition 3.

$A =$

$$\begin{bmatrix} -0.3696E+1 & 0.0000E+0 & -0.1143E+3 & 0.5044E+3 & -0.1034E+4 & 0.7507E+1 \\ 0.3555E-1 & -0.3567E+0 & 0.0000E+0 & -0.1431E+1 & 0.1690E+3 & 0.3025E+0 \\ 0.7624E+0 & 0.0000E+0 & -0.3989E+3 & 0.3783E+3 & 0.0000E+0 & 0.0000E+0 \\ 0.0000E+0 & 0.0000E+0 & 0.4767E+4 & -0.5133E+4 & 0.0000E+0 & 0.1544E+2 \\ 0.6997E+0 & 0.0000E+0 & -0.7397E+1 & 0.7474E+3 & -0.4431E+4 & 0.3959E+1 \\ -0.3040E+2 & 0.0000E+0 & 0.2036E+6 & -0.2172E+6 & 0.0000E+0 & 0.6080E+3 \end{bmatrix}$$

$$\bar{b} = \begin{bmatrix} 0.5287E+5 \\ 0.2131E+4 \\ 0.0000E+0 \\ 0.1210E+6 \\ 0.2789E+5 \\ 0.4767E+7 \end{bmatrix}$$

$$C = \begin{bmatrix} \mathbf{I} \end{bmatrix}$$

$$\bar{d} = \begin{bmatrix} 0.0000E+0 \\ 0.0000E+0 \\ 0.0000E+0 \\ 0.0000E+0 \\ 0.0000E+0 \\ 0.7044E+4 \end{bmatrix}$$

Figure B12. - 6 degree-of-freedom model for trim condition 3.

APPENDIX C
T700 FUEL CONTROL SYSTEM MODEL

The real-time model of the T700-GE-700 fuel control system is given below.

T700 Fuel Control System Variables and Constants

$AWFP$	HMU deceleration schedule gain, $lb_m \cdot in^2/lb_f \cdot hr \cdot \%$
$B4$	ECU nonlinear NP-loop-gain circuit (discrete switch)
$B6$	ECU speed error gain
$BWFP$	HMU deceleration schedule bias, $lb_m \cdot in^2/lb_f \cdot hr$
CB	ECU error threshold for additional NP governing gain, *percent* NP
CE	ECU load-share-authority upper limit, *percent* NP
CH	hysteresis of gas-generator speed sensor, *percent* NG
$CLMV$	metering-valve lag time constant, *sec*
$CLLDS$	load-demand-spindle lag time constant, *sec*
$CNTL$	lag time constant for gas-generator-speed sensor, *sec*
$CORR$	threshold for nonlinear NP-loop-gain circuit
CR	engine torque-level threshold for nonlinear NP loop gain circuit
$CT2$	lag time constant for ECU governor, *sec*
$CT7$	lag time constant for ECU load-share circuit, *sec*
$CT9$	ECU T4.5-compensation lag time constant, *sec*
$CT12$	lag time constant for ECU governor, *sec*
$CT13$	lag time constant for ECU governor-rate compensation, *sec*
$CT14$	lag time constant for ECU governor-rate compensation, *sec*
$CT16$	lag time constant for ECU proportional-plus-integral compensation, *sec*

$CTPL$ lag time constant for power turbine speed sensor, sec

$CTPS3$ lag time constant for compressor static-discharge pressure sensor, sec

$DBIAS$ lower limit and bias for ECU load share authority, $percent\ NP$

$DWFP$ fuel flow command for HMU load-demand spindle, $lb_m \cdot in^2 / lb_f \cdot hr$

$DWFPL$ fuel flow command for HMU load-demand spindle including dynamics, $lb_m \cdot in^2 / lb_f \cdot hr$

$ET45$ T4.5 error signal, $deg\ R$

$HMUSEL$ W_f/P_s3 demand after limiting by idle, acceleration, and deceleration cams, $lb_m \cdot in^2 / lb_f \cdot hr$

$KNDRP$ droop line slope, $\Delta(W_f/P_s3)/\Delta PCNG$, $lb_m \cdot in^2 / lb_f \cdot hr \cdot percent$

NG rotational speed of compressor and gas generator, rpm

$NGREF$ NG reference speed in percent of design speed, $percent\ NG$

$P45$ total pressure at power turbine inlet, lb_f/in^2

PAS angle of power available spindle, deg

$PCNG$ rotational speed of compressor and gas generator in percent of design speed, $percent\ NG$

$PCNGI$ set point value of gas generator speed determined by idle schedule, $percent\ NG$

$PCNGHL$ gas generator speed including sensor dynamics and hysteresis, $percent\ NG$

$PCNP$ rotational speed of power turbine in percent of design speed, $percent\ NP$

$PCPRF$ reference rotational speed of pc ver turbine as set by cockpit control, $percent\ NP$

PNG set point value of gas generator speed determined by load demand-compensation circuit, $percent\ NG$

$PS3$ compressor static discharge pressure, lb_f/in^2

$PS3HYS$ compressor discharge-pressure-sensor hysteresis, lb_f/in^2

$PS3L$	compressor discharge pressure including sensor dynamics and hysteresis, lb_f/in^2
$SPDER$	ECU speed error signal, *percent NP*
$SPDG$	ECU trim-demand signal, *volts*
$SPDS1$	ECU compensated speed error signal, *volts*
$SPDSF$	ECU speed error signal with governor dynamics; input to ECU error selector logic, *volts*
$SPDSP$	ECU compensated trim-demand signal, *volts*
$SPDSS$	ECU trim-demand signal before compensation, *volts*
$T2$	inlet temperature, *deg R*
$T8$	lead-time constant for ECU T4.5 limiter compensation, *sec*
$T10$	lag-time constant for ECU T4.5 limiter compensation, *sec*
$T11$	lead-time constant for ECU governor, *sec*
$T17$	lag-time constant for ECU load share, *sec*
$T45$	power turbine inlet temperature, T4.5, *deg R*
$T45COR$	ECU T4.5 thermocouple harness correlation bias, *deg R*
$T45E$	measured T4.5, *deg R*
$T45EL$	T4.5 sensed by ECU thermocouple harness, *deg R*
$T45L$	measured T4.5 with harness dynamics, *deg R*
$T45REF$	reference constant used as maximum T4.5 limit, *deg R*
$TAU45$	T4.5 harness time-constant which varies based on station 4.5 flow parameter and T4.5, *sec*
$TL1$	lag-time constant 1 for ECU load-share torque sensor, *sec*
$TL2$	lag-time constant 2 for ECU load share torque sensor, *sec*

$TLGE$ T4.5-harness time constant, sec

$TMDB$ HMU torque motor deadband, ma

$TMGN$ HMU torque motor sensitivity, $in/ma \cdot sec$

$TMLG$ HMU torque motor linkage gain, $lb_m \cdot in^2/lb_f \cdot hr \cdot in$

$TMLVG$ HMU torque motor LVDT feedback gain, $volts/in$

$TMRU$ W_f/P_s3 trim signal from torque motor based on ECU trim signal, $lb_m \cdot in^2/lb_f \cdot hr$

$TORQ45$ power turbine torque (identical to Q_{PT}), $ft \cdot lb_f$

$TRQER$ sensed torque error between two engines operating in parallel, $ft \cdot lb_f$

$TRQL$ sensed power-turbine output torque, $ft - lb_f$

$TSIG$ compensated T4.5 error signal; input to ECU error selector logic, $volts$

$W45$ power-turbine-inlet mass flow rate, lb_m/hr

$W45R$ power turbine flow parameter

WF fuel flow, lb_m/sec

$WFIDM$ minimum value of W_f/P_s3 demand regardless of all other commands, $lb_m \cdot in^2/lb_f \cdot hr$

$WFIRF$ set point value of W_f/P_s3 determined by idle schedule, $lb_m \cdot in^2/lb_f \cdot hr$

$WFMAX$ maximum available fuel flow; represents maximum aperture in metering valve, lb_m/hr

$WFMIN$ minimum available fuel flow; represents minimum flow stop in metering valve, lb_m/hr

$WFMV$ fuel flow required by HMU; results from multiplication of W_f/P_s3 and P_s3 via mechanical linkage, lb_m/hr

$WFPAC$ maximum value of W_f/P_s3 demand during acceleration transients; prevents compressor stall, $lb_m \cdot in^2/lb_f \cdot hr$

$WFPDC$ minimum value of W_f/P_s3 demand during deceleration transients; prevents engine flameout, $lb_m \cdot in^2/lb_f \cdot hr$

$WFPDCH$ maximum limit on W_f/P_s3 demand during deceleration, $lb_m \cdot in^2/lb_f \cdot hr$

$WFPDCL$ minimum limit on W_f/P_s3 demand during deceleration, $lb_m \cdot in^2/lb_f \cdot hr$

$WFPDM$ commanded W_f/P_s3 signal before limiting selector logic, $lb_m \cdot in^2/lb_f \cdot hr$

$WFPRF$ maximum available W_f/P_s3 signal; set by power available spindle, $lb_m \cdot in^2/lb_f \cdot hr$

$WFPTP$ W_f/P_s3 topping signal, $lb_m \cdot in^2/lb_f \cdot hr$

$WFQPS3$ set point value of W_f/P_s3 determined by load demand compensation circuit, $lb_m \cdot in^2/lb_f \cdot hr$

$XCPC$ helicopter collective pitch position in percent of maximum, *percent*

$XHILIM$ torque motor maximum limit, in/sec

$XKINTG$ ECU proportional-plus-integral compensation integral-path gain

$XKPROP$ ECU proportional-plus-integral compensation proportional-path gain

$XLDHYS$ load demand spindle hysteresis, deg

$XLDSA$ load demand spindle angle, deg

$XLDSH$ load demand spindle angle with hysteresis, deg

$XLOLIM$ torque motor minimum limit, in/sec

$XQLO$ load share error input, *percent* NP

$YHILIM$ engine torque-integrator maximum limit for nonlinear NP loop gain circuit

$YLOLIM$ engine torque-integrator minimum limit for nonlinear NP loop gain circuit

$ZHILIM$ ECU proportional-plus-integral compensation integrator maximum limit

$ZK1$ NP loop additional proportional gain for ECU governor rate compensation used during high power operation

$ZK3$ ECU T4.5 compensation-circuit gain

$ZK5$ ECU governor-rate-compensation loop gain

$ZK7$ NP loop proportional gain for ECU governor rate compensation

$ZK8$ ECU load-share-path gain

$ZK9$ speed error trim gain for ECU governor rate compensation

$ZK10$ additional gain loop for ECU governor rate compensation for errors greater than the absolute value of CB

$ZLOLIM$ ECU proportional-plus-integral compensation integrator minimum limit

Table C.1

T700 Fuel Control System Constants

Constant	Value	Units
$AWFP$	0.05909	$lb_m \cdot in^2/lb_f \cdot hr \cdot \%$
$B6$	1.0	nondimensional
$BWFP$	-3.927	$lb_m \cdot in^2/lb_f \cdot hr$
CB	0.75	$\%NP$
CE	13.21	$\%NP$
CH	0.05	$\%NG$
$CLMV$	0.03	sec
$CLLDS$	0.2	sec
$CNTL$	0.025	sec
$CORR$	20.0	nondimensional
CR	20.0	nondimensional
$CT2$	0.088	sec
$CT7$	1.0	sec
$CT9$	0.010	sec
$CT12$	0.088	sec
$CT13$	1.0	sec
$CT14$	0.10	sec
$CT16$	1.0	sec
$CTPL$	0.010	sec
$CTPS3$	0.010	sec
$DBIAS$	3.25	$\%NP$
$KNDRP$	0.25	$lb_m \cdot in^2/lb_f \cdot hr \cdot \%$
$NGREF$	101.0	$\%NG$
$PS3HYS$	0.375	lb_f/in^2
$T8$	0.40	sec
$T10$	0.060	sec
$T11$	0.87	sec
$T17$	0.010	sec

Table C.1 Concluded
T700 Fuel Control System Constants

Constant	Value	Units
$T45COR$	11.0	$°R$
$T45REF$	2004.0	$°R$
$TL1$	0.010	sec
$TL2$	0.010	sec
$TLGE$	0.077	sec
$TMDB$	2.0	ma
$TMGN$	0.0159	$in/ma \cdot sec$
$TMLG$	84.0	$lb_m \cdot in^2/lb_f \cdot hr \cdot in$
$TMLVG$	55.0	$volts/in$
$WFMAX$	785.0	lb_m/hr
$WFMIN$	65.0	lb_m/hr
$WFPDCH$	2.10	$lb_m \cdot in^2/lb_f \cdot hr$
$WFPDCL$	1.45	$lb_m \cdot in^2/lb_f \cdot hr$
$XHILIM$	0.0787	in/sec
$XKINTG$	0.18	nondimensional
$XKPROP$	0.20	nondimensional
$XLDHYS$	2.5	deg
$XLOLIM$	-0.0427	in/sec
$YHILIM$	40.0	nondimensional
$YLOLIM$	0.0	nondimensional
$ZHILIM$	3.5	nondimensional
$ZK1$	1.7	nondimensional
$ZK3$	0.045	nondimensional
$ZK5$	0.40	nondimensional
$ZK7$	0.30	nondimensional
$ZK8$	0.231	nondimensional
$ZK9$	0.625	nondimensional
$ZK10$	0.375	nondimensional
$ZLOLIM$	-1.0	nondimensional

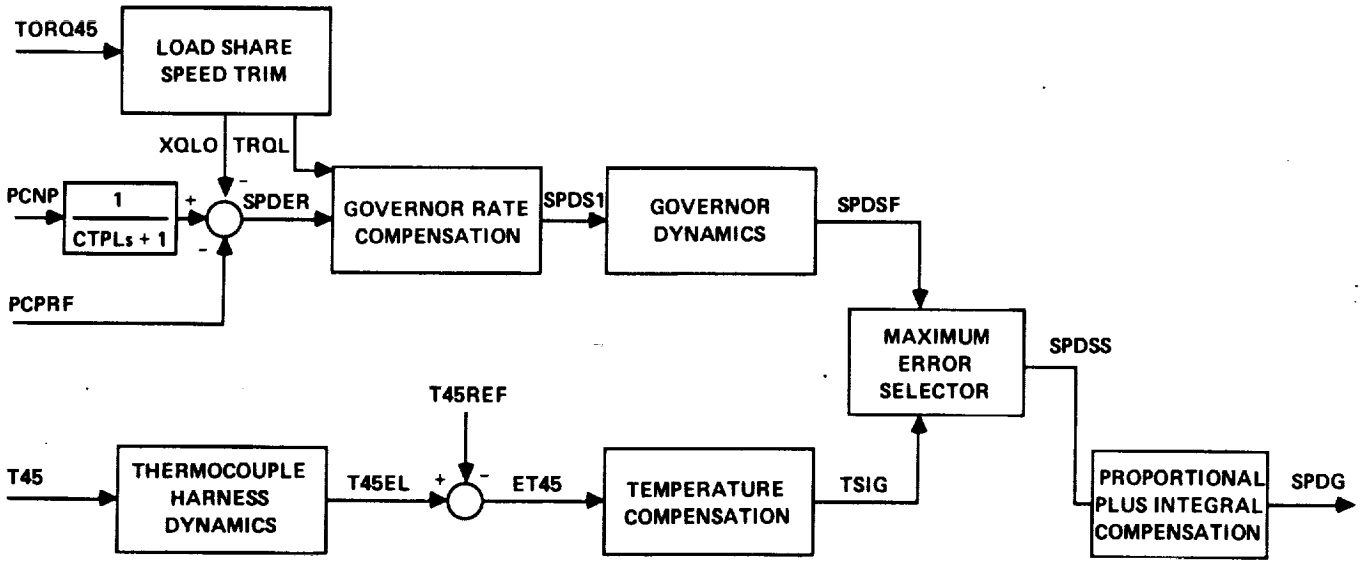

Figure C1.- T700 electrical control unit (ECU).

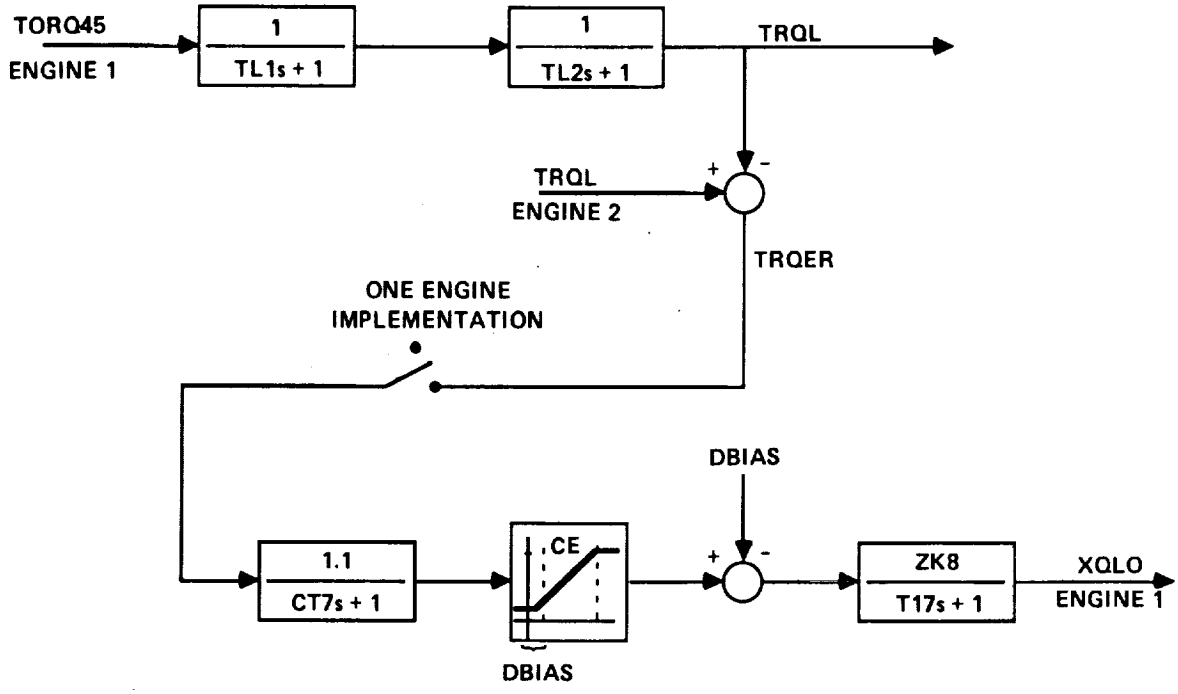

Figure C2.- T700 ECU load-share speed trim.

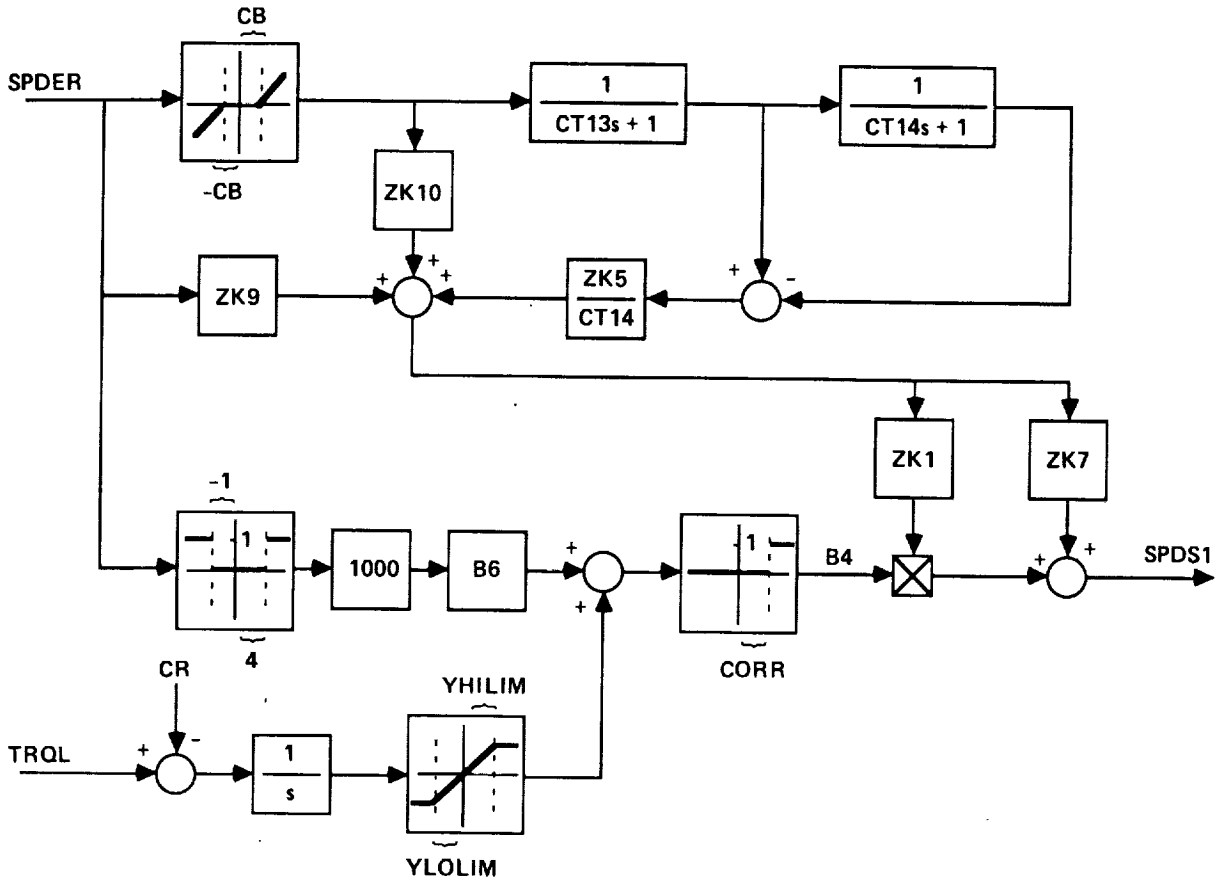

Figure C3.- T700 ECU governor rate compensation.

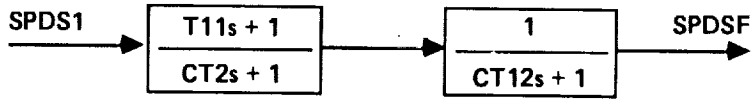

Figure C4.- T700 ECU governor dynamics.

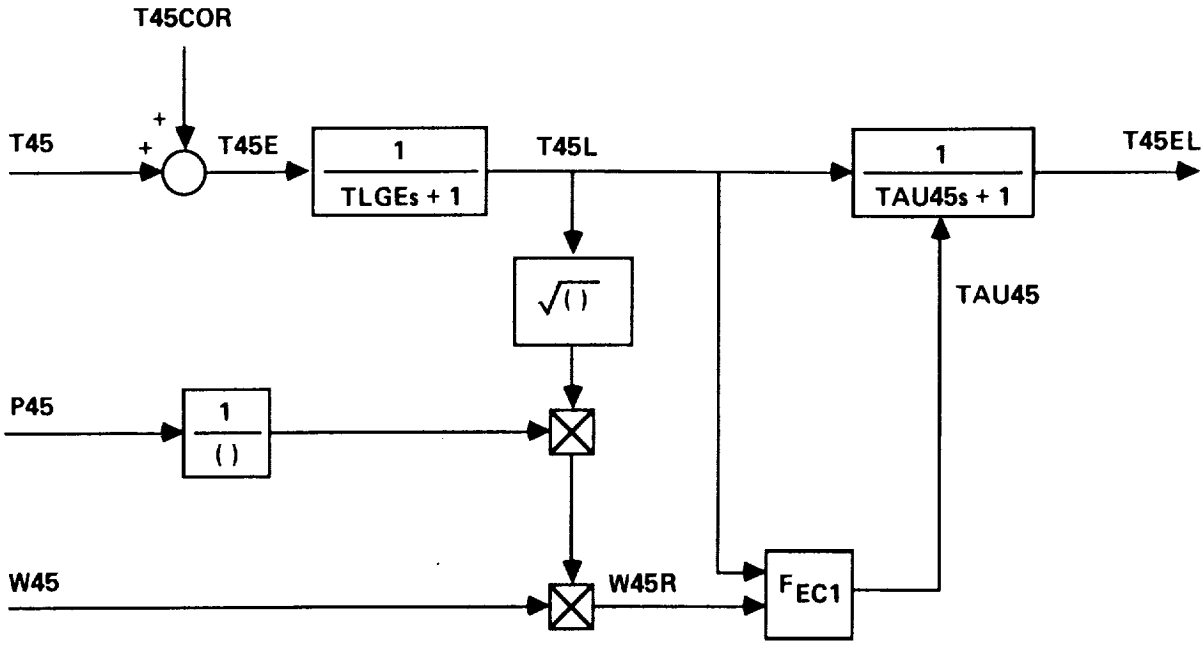

Figure C5.- T700 ECU thermocouple harness.

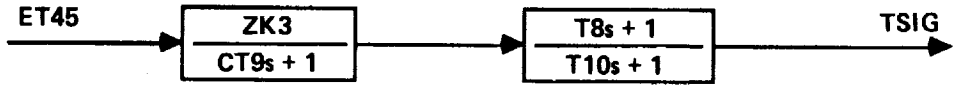

Figure C6.- T45 compensation.

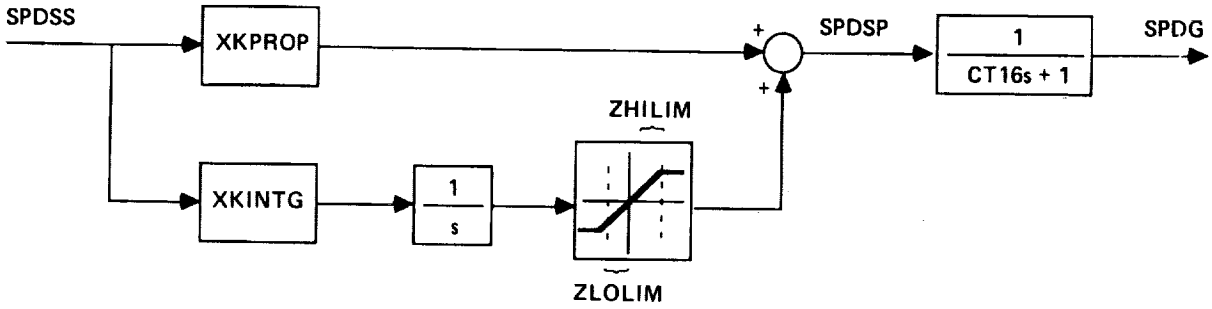

Figure C7.- T700 ECU proportional plus integral (P+I) compensation.

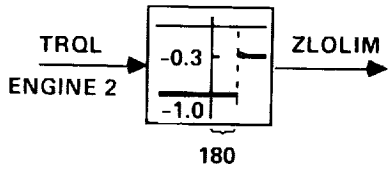

Figure C8.- P+I integrator limit logic.

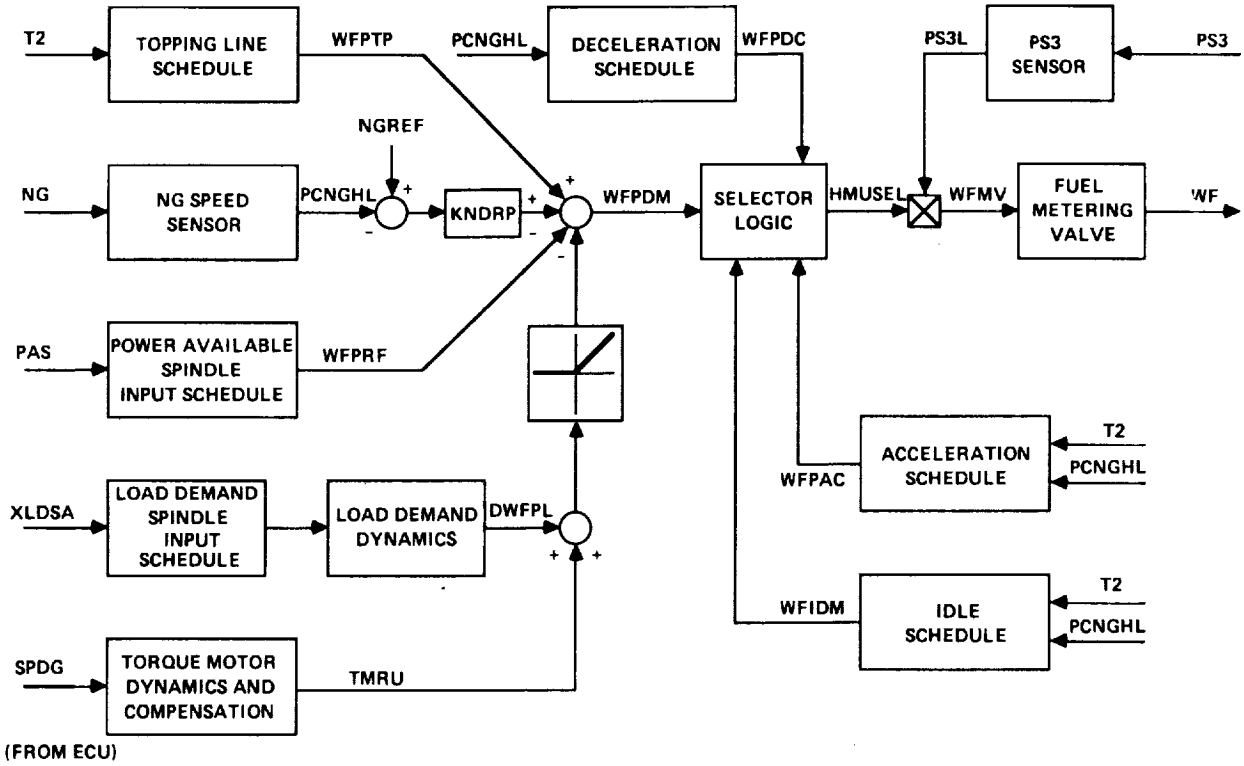

Figure C9.- T700 hydromechanical control unit (HMU).

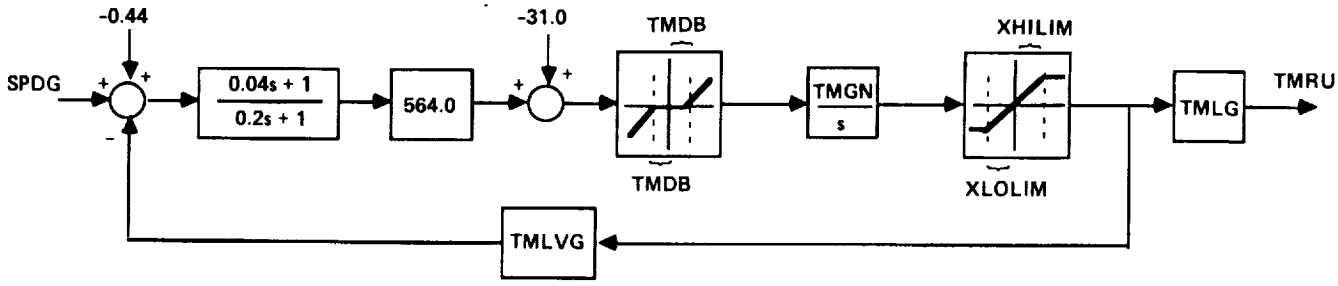

Figure C10.- T700 torque motor dynamics and compensation.

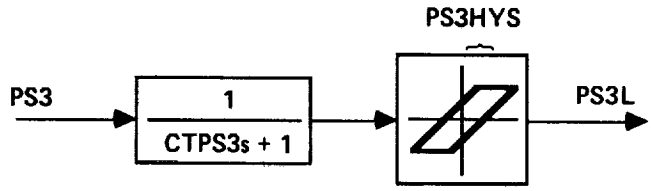

Figure C11.- Compressor static discharge pressure sensor.

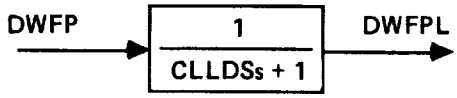

Figure C12.- Load demand (fuel flow command) dynamics.

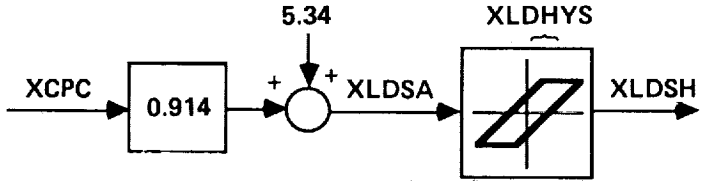

Figure C13.- Collective pitch to load demand spindle rigging (UH-60A Black Hawk implementation).

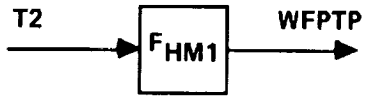

Figure C14.- Topping line schedule.

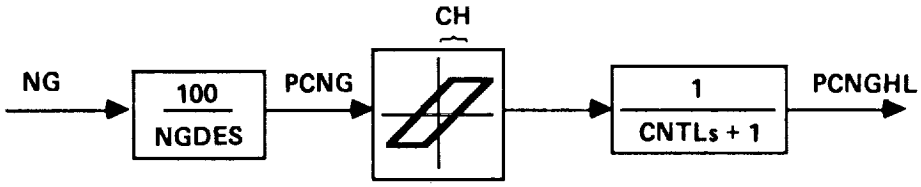

Figure C15.- NG spool sensor dynamics.

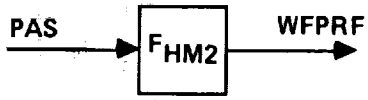

Figure C16.- Power available spindle input schedule.

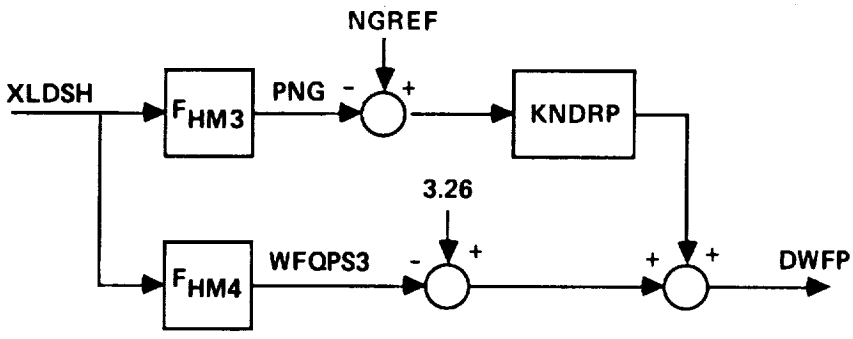

Figure C17.- Load demand spindle input schedule.

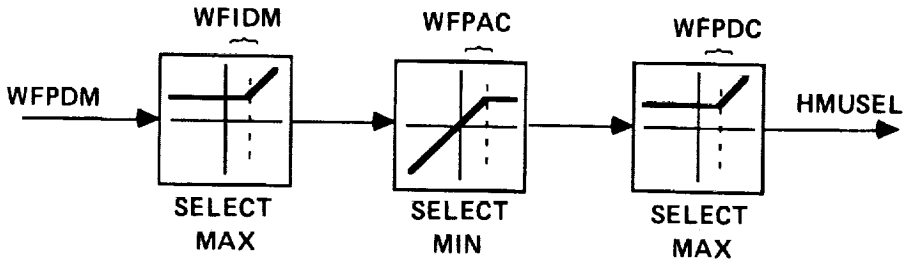

Figure C18.- Limit selector logic.

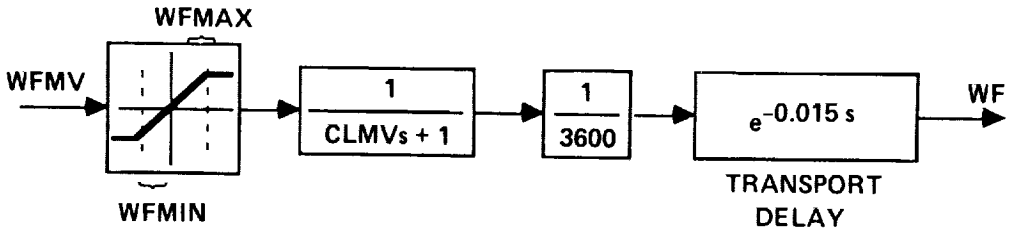

Figure C19.- Fuel flow metering valve.

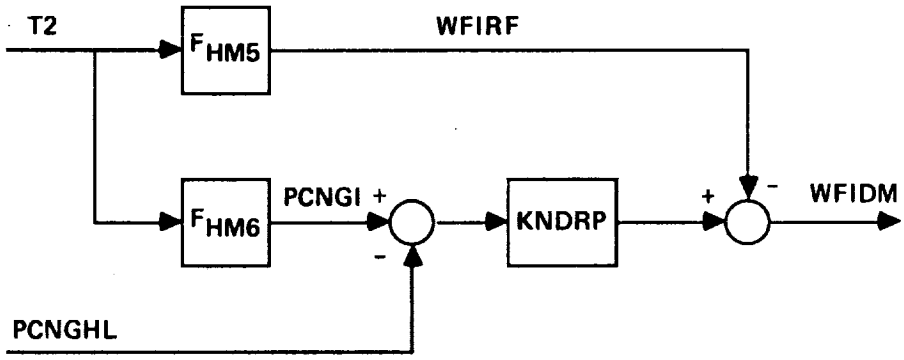

Figure C20.- Idle schedule.

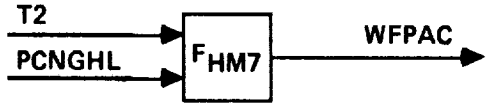

Figure C21.- Acceleration schedule.

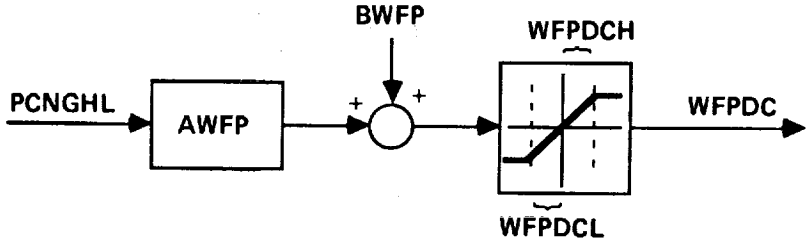

Figure C22.- Deceleration schedule.

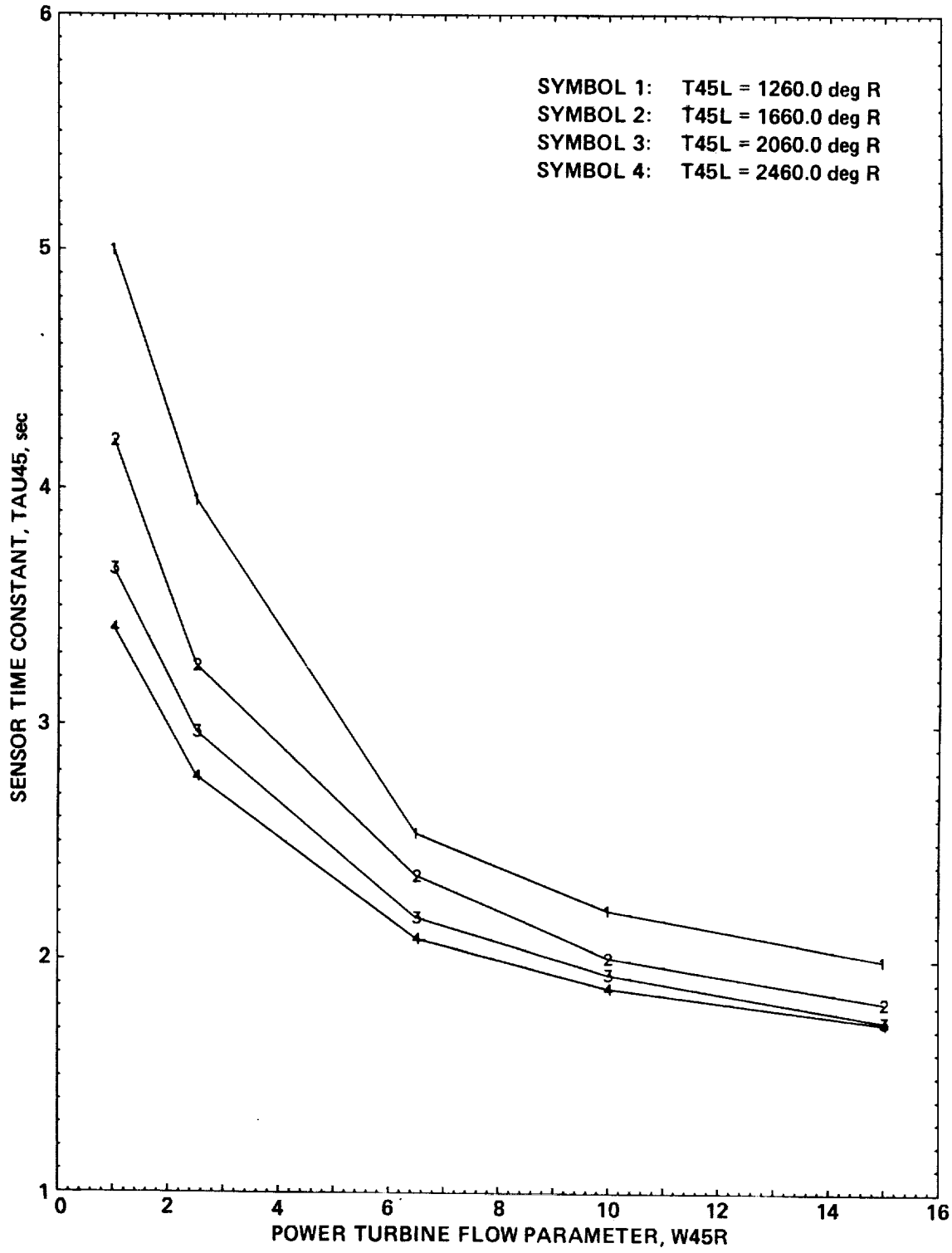

Figure C23.- T700 real-time model function F_{EC1}—ECU thermocouple sensor time constant.

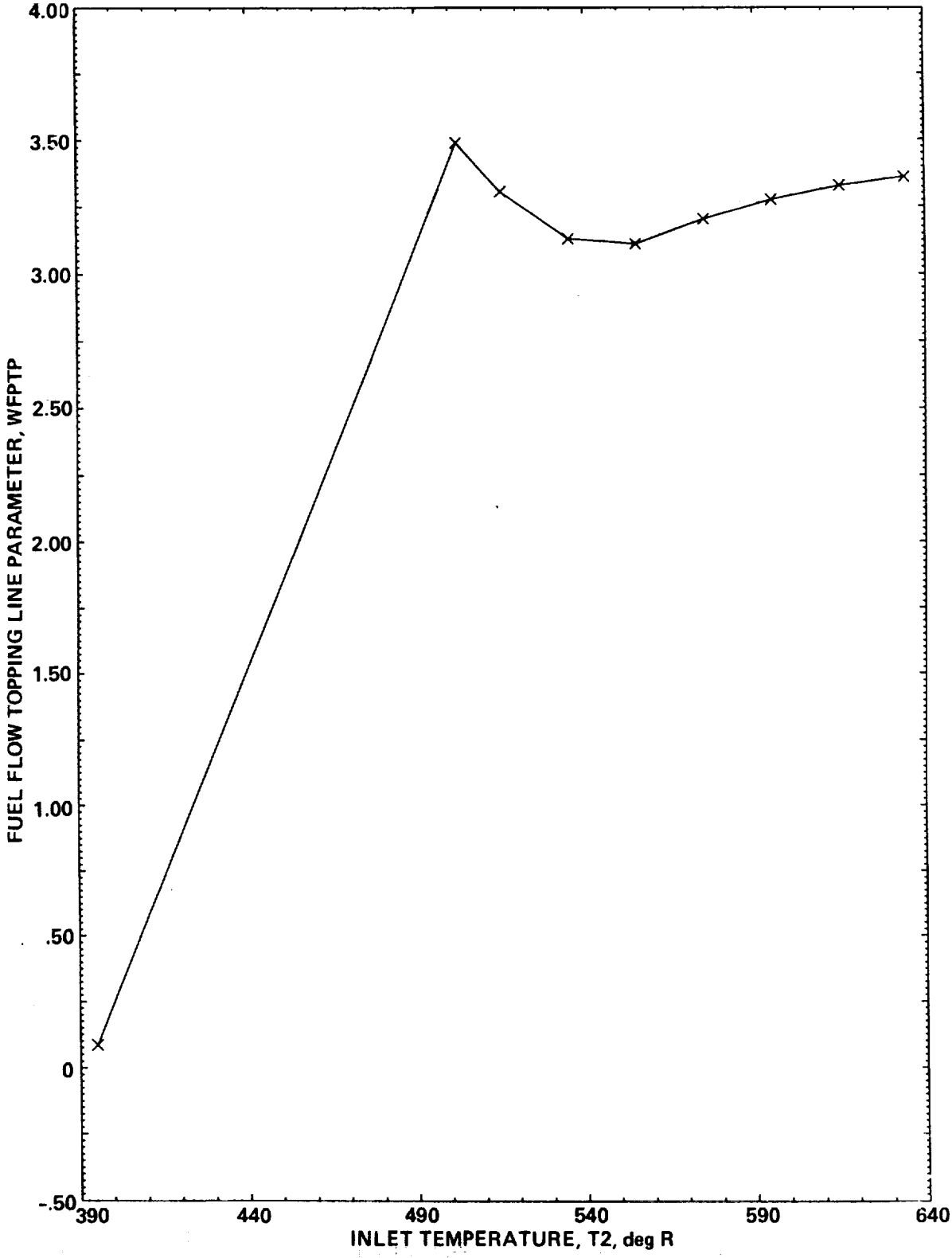

Figure C24.- T700 real-time model function F_{HM1}—HMU topping line schedule.

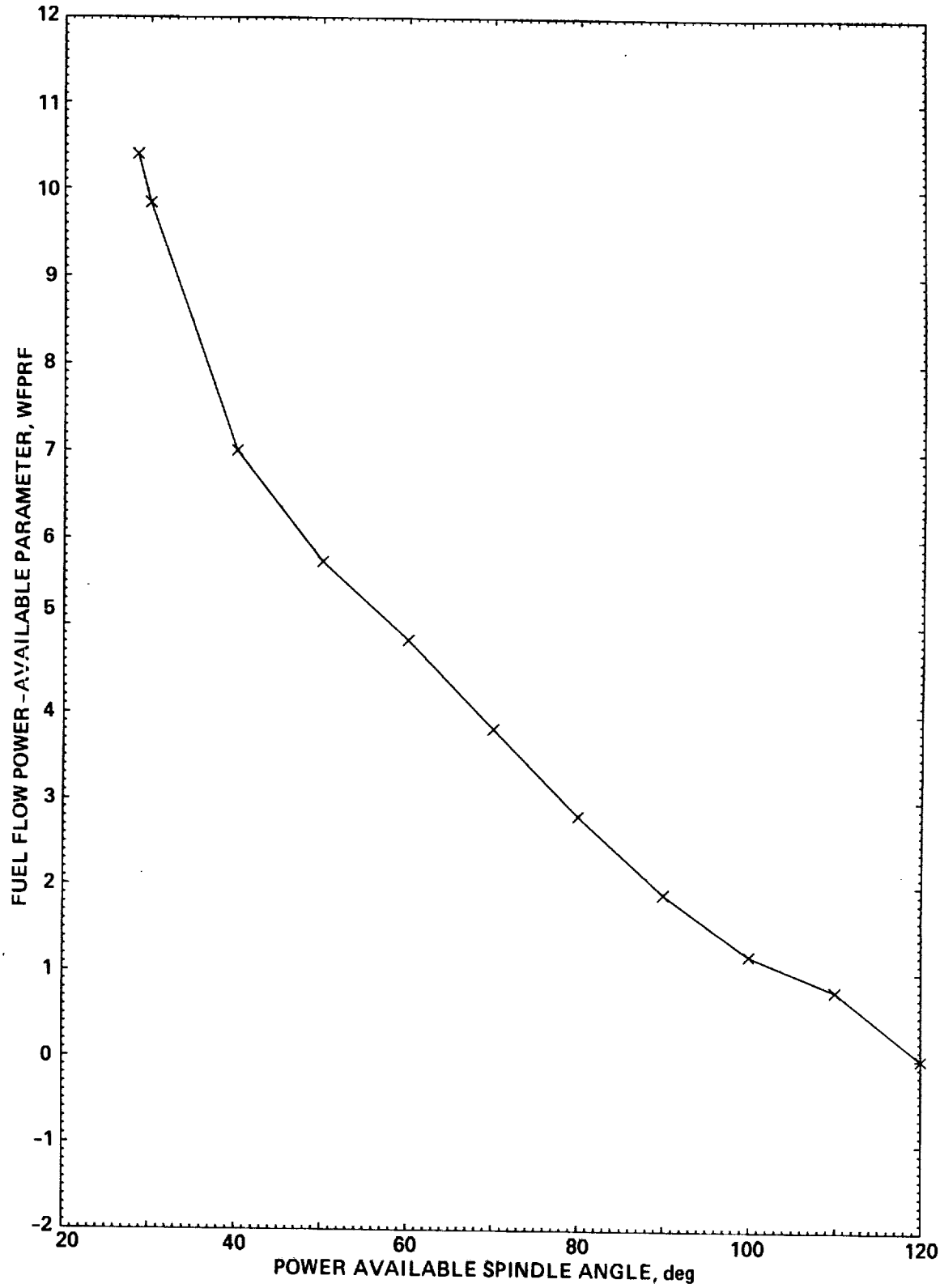

Figure C25.- T700 real-time model function F_{HM2}—HMU power-available input schedule.

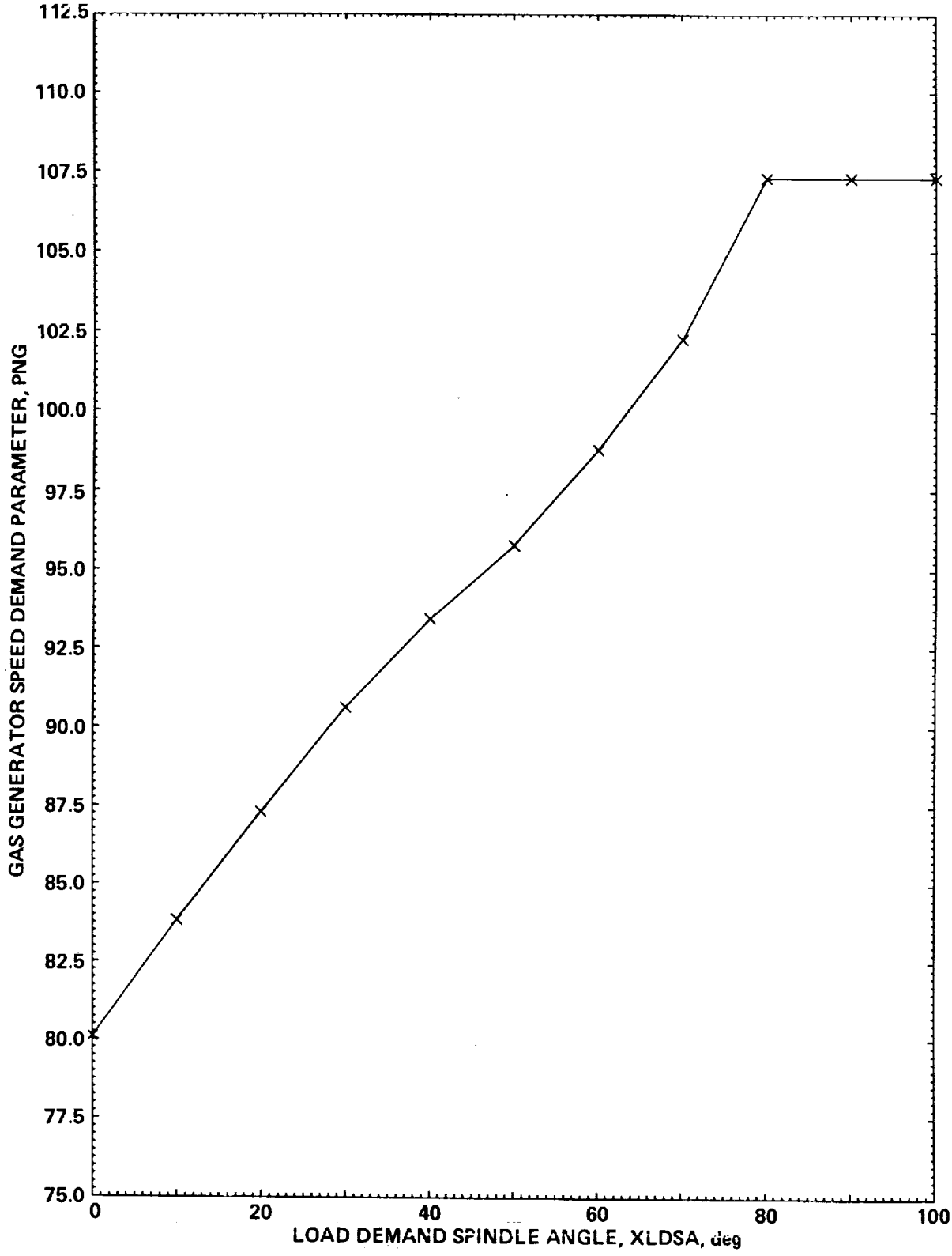

Figure C26.- T700 real-time model function F_{HM3}—HMU load-demand-compensation schedule function 1.

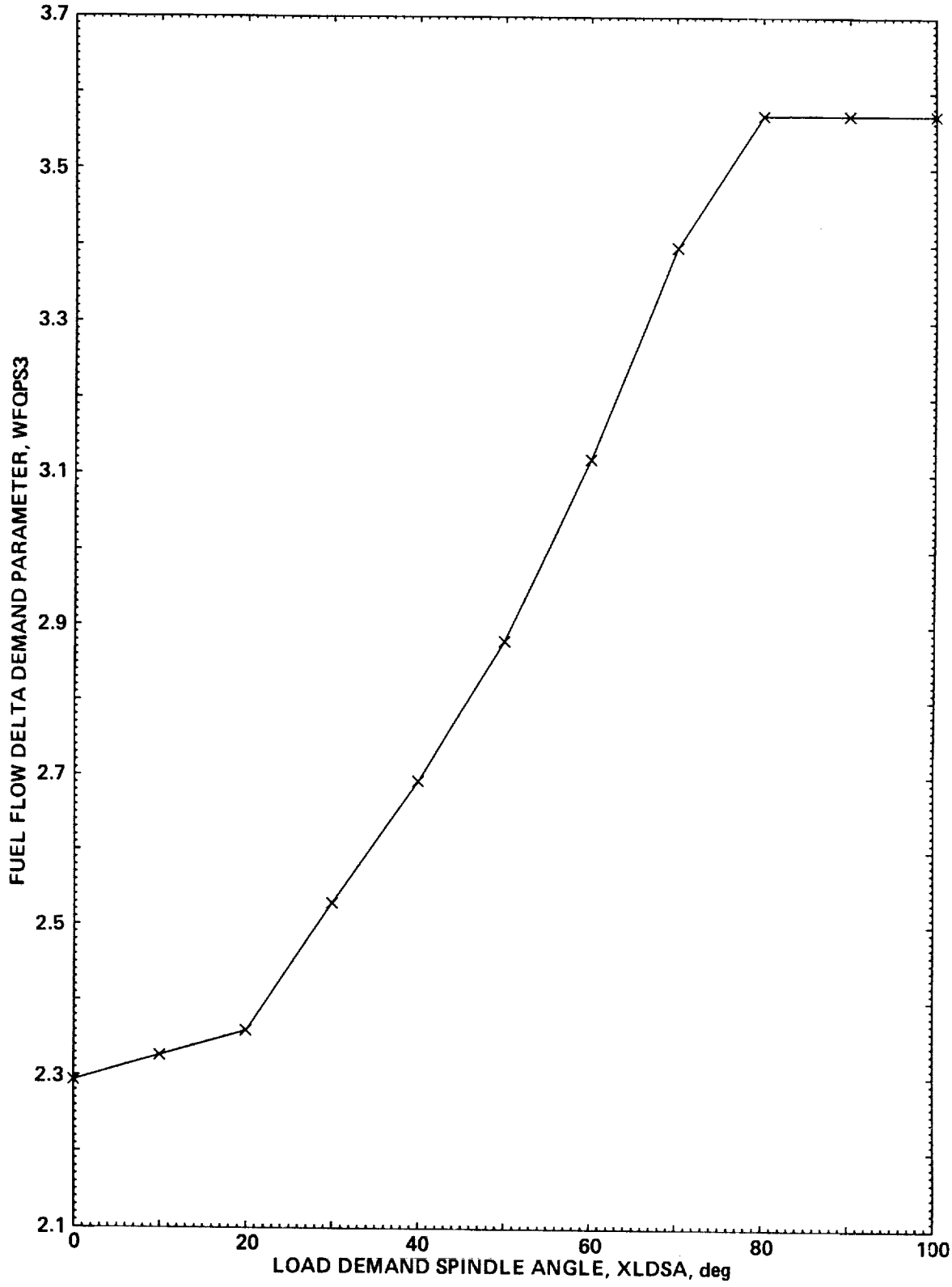

Figure C27.- T700 real-time model function F_{HM4}—HMU load-demand-compensation schedule function 2.

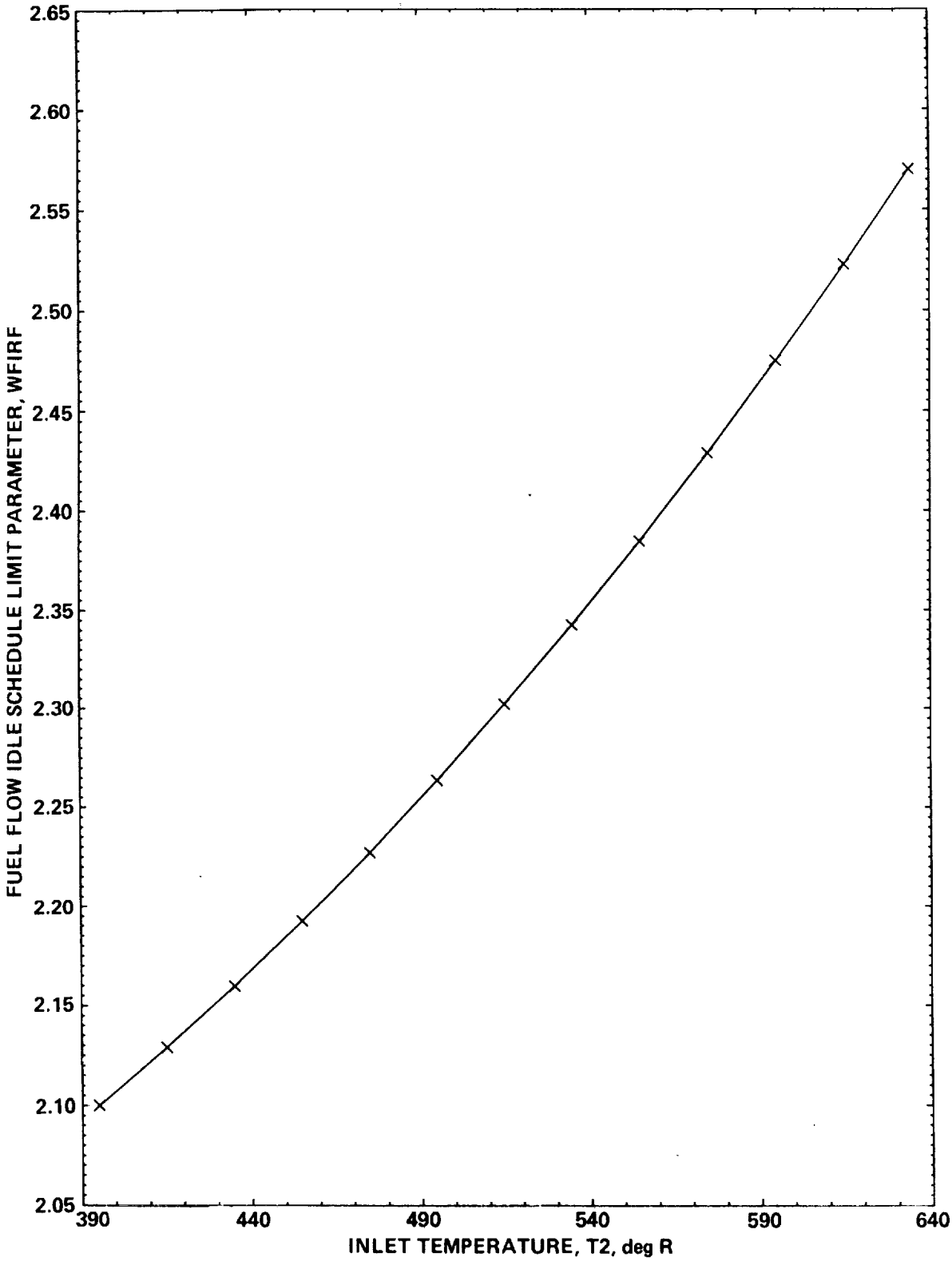

Figure C28.- T700 real-time model function F_{HM5}—HMU idle-schedule function 1.

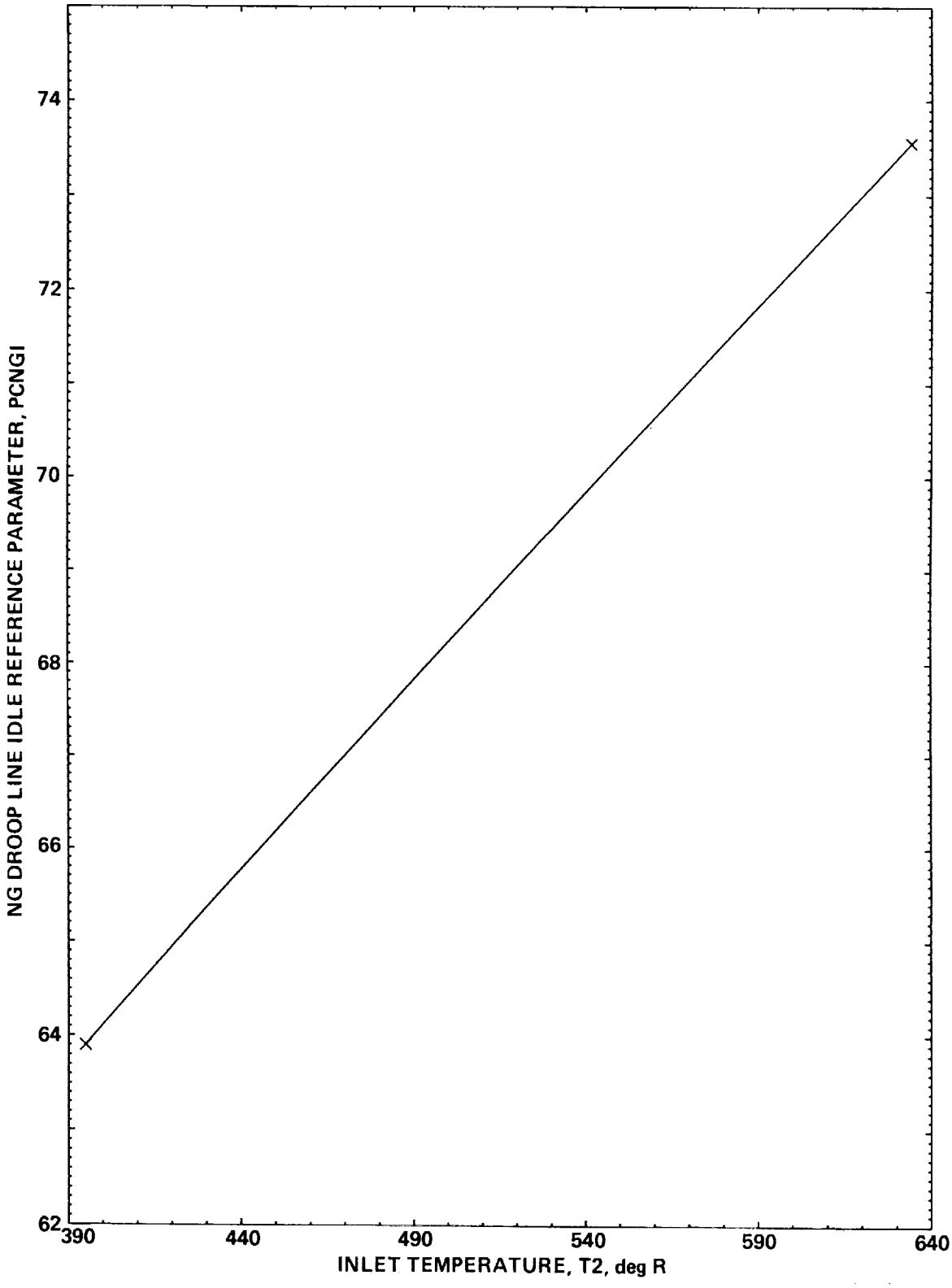

Figure C29.- T700 real-time model function F_{HM6}—HMU idle-schedule function 2.

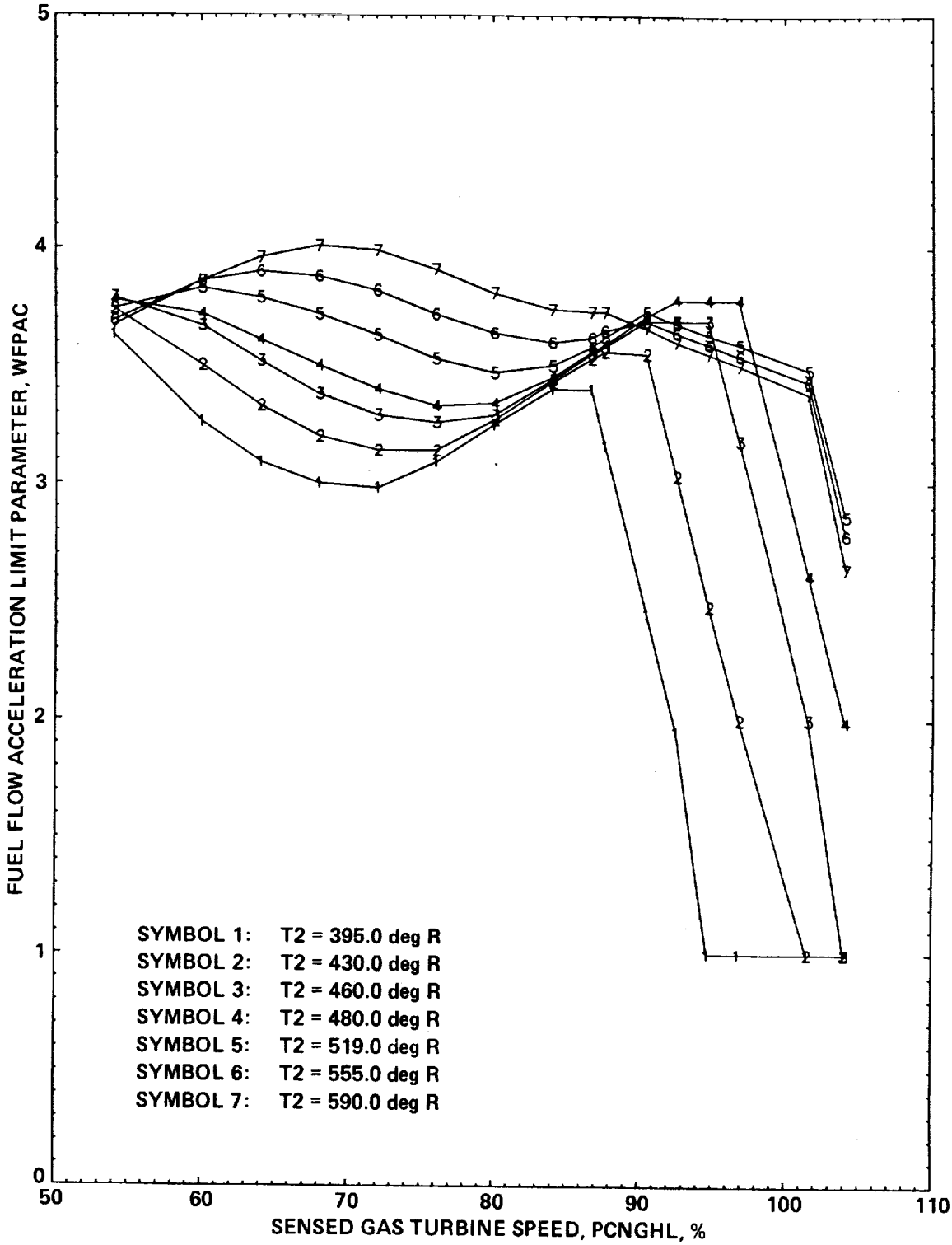

Figure C30.- T700 real-time model function F_{HM7}—HMU maximum fuel-parameter limit during acceleration.

REFERENCES

1. Hull, R.: Development of a Rotorcraft/Propulsion Dynamics Interface Analysis: Volume I. NASA CR-166380, 1982.

2. Howlett, J. J.: UH-60A Black Hawk Engineering Simulation Program: Volume I – Mathematical Model. NASA CR-166309, 1981.

3. Mihaloew, J. R.; Ballin, M. G.; and Ruttledge, D. G. C.: Rotorcraft Flight-Propulsion Control Integration. NASA-Army Rotorcraft Technology Conference paper, 1987.

4. Kaplita, T. T.: UH-60A Black Hawk Engineering Simulation Model Validation and Proposed Modifications. Tech. Rep. SER-70982, United Technologies Sikorsky Aircraft, 1984.

5. General Electric Aircraft Engine Business Group: Model Specification for T700-GE-701 Turboshaft Engine, Part I. DARCOM CP-2222-02701, 1983.

6. Prescott, W. E.; and Mabee, R. L.: T700-GE-700 Training Guide. General Electric Aircraft Engine Business Group; Technical Training Operation, 1984.

7. Hart, C. E.; and Wensel, L. M.: Real-Time Hybrid Computer Simulation of a Small Turboshaft Engine and Control System. NASA TM-83579, 1984.

8. Seldner, K.; Mihaloew, J. R.; and Blaha, R. J.: Generalized Simulation Technique for Turbojet Engine System Analysis. NASA TN D-6610, 1972.

9. Mihaloew, J. R.; and Hart, C. E.: Real Time Digital Propulsion System Simulation for Manned Flight Simulators. NASA TM-78958, 1978.

10. Mihaloew, J. R.: A Nonlinear Propulsion System Simulation Technique for Piloted Simulators. NASA TM-82600, 1981.

11. French, M. W.: Development of a Compact Real-Time Turbofan Engine Dynamic Simulation. SAE Rep. 821401, Society of Automotive Engineers, 1982.

12. Pineo, F. J.: Adaptive Update Method for Embedded Real-Time Jet Engine Models. M.S. thesis, Massachusetts Institute of Technology, 1985.

13. Ballin, M. G.: Validation of a Real-Time Engineering Simulation of the UH-60A Helicopter. NASA TM-88360, 1987.

14. Abbott, W. Y.; Benson, J. O.; Oliver, R. C.; and Williams, R. A.: Validation Flight Test of UH-60A for Rotorcraft Systems Integration Simulator (RSIS). USAAEFA Project 79-24, United States Army Aviation Engineering Flight Activity, 1982.

NASA
National Aeronautics and Space Administration

Report Documentation Page

1. Report No.	2. Government Accession No.	3. Recipient's Catalog No.
NASA TM-100991		

4. Title and Subtitle

A High Fidelity Real-Time Simulation of a Small Turboshaft Engine

5. Report Date

July 1988

6. Performing Organization Code

7. Author(s)

Mark G. Ballin

8. Performing Organization Report No.

A-88151

10. Work Unit No.

505-61-51

9. Performing Organization Name and Address

Ames Research Center
Moffett Field, California 94035

11. Contract or Grant No.

13. Type of Report and Period Covered

Technical Memorandum

12. Sponsoring Agency Name and Address

National Aeronautics and Space Administration
Washington, D.C. 20546-0001

14. Sponsoring Agency Code

15. Supplementary Notes

Point of contact: Mark G. Ballin, Ames Research Center, MS 211-2, Moffett Field, California 94035
(415) 694-6115 or FTS 464-6115

16. Abstract

A high-fidelity component-type model and real-time digital simulation of the General Electric T700-GE-700 turboshaft engine were developed for use with current generation real-time blade-element rotor helicopter simulations. A control system model based on the specification fuel control system used in the UH-60A Black Hawk helicopter is also presented. The modeling assumptions and real-time digital implementation methods particular to the simulation of small turboshaft engines are described. The validity of the simulation is demonstrated by comparison with analysis-oriented simulations developed by the manufacturer, available test data, and flight-test time histories.

C-2

17. Key Words (Suggested by Author(s))	18. Distribution Statement
Helicopter Flight simulation Turboshaft engine Controls	Unclassified - Unlimited Subject Category - 08

19. Security Classif. (of this report)	20. Security Classif. (of this page)	21. No. of pages	22. Price
Unclassified	Unclassified	89	A05